Investigating the Immune Cell Response to Albumin-Derived Perfluorocarbon-Based Artificial Oxygen Carriers (A−AOCs)

Dissertation

presented by
Linda Marciale Tchuendem
Born in Baham

in partial fulfilment of the requirements
for the Degree of
Dr. rer. nat.

Faculty of Chemistry
Universität Duisburg-Essen

2023

The current study was conducted within the research team led by Prof. Dr. Katja Ferenz at the Institute of Physiological Chemistry, University of Duisburg-Essen.

Supervisor: **Prof. Dr. Katja Ferenz**

1. Examiner: **Prof. Dr. Katja Ferenz**

2. Examiner: **Prof. Dr. Stefanie Flohé**

Chairman: **Prof. Dr. Eckart Hasselbrink**

Date of the disputation: **19 June 2024**

Dedication

To my children,

As you journey along your own paths in life, remember that my love and encouragement are always with you. May you find inspiration in these pages to overcome challenges and achieve your dreams.

DOI: 10.17185/duepublico/82251
URN: urn:nbn:de:hbz:465-20240807-071155-1

Table of Contents

1. Abstract

Albumin-derived perfluorocarbon-based artificial oxygen carriers (A−AOCs) exhibit promising potential as substitutes for red blood cells in critical medical scenarios, such as emergencies, trauma, and major surgeries, where rapid and efficient oxygen delivery is vital. Despite their potential advantages, their clinical implementation has been hindered by limited understanding of their interactions with immune cells. In this study, we evaluated the effects of A−AOCs on immune responses using three macrophage models: Primary human macrophages-like cells (PHM), murine macrophages (cell line J774), and murine bone marrow-derived macrophages (BMDM). Our findings indicate that 10 ng/ml phorbol 12-myristate 13-acetate (PMA) ensured stable differentiation of THP-1 cells into PHM. A−AOCs exhibited a potential to mitigate cell extravasation and migration in PHM. Moreover, A−AOCs up to 4 % concentration displayed good tolerance without inducing significant cytotoxicity in all three macrophage models. Protein and gene expression analysis revealed that A−AOCs up to 10 % concentration did not activate these macrophages. Overall, our results demonstrated that macrophages indeed internalized A−AOCs, as confirmed by transmission electron microscopy (TEM), confocal laser scanning microscopy (LSM), and correlative light and electron microscopy (CLEM) analyses. However, subsequent activation by A−AOCs post-internalization was not observed, as confirmed by our cytokine and mRNA measurements. Additionally, A−AOCs did not significantly affect oxygen consumption rate or induce oxidative stress in PHM. The present study provides insight into A−AOCs interactions with immune cells, supporting their safety for potential application as oxygen carriers in critical medical situations.

Keywords: albumin-derived perfluorocarbon-based artificial oxygen carriers, macrophages, immune response, cytotoxicity, cell differentiation, oxygen consumption, nanoparticle uptake, inflammation.

2. Zusammenfassung

Albuminumhüllte perfluorocarbonbasierte künstliche Sauerstoffträger (A−AOCs) zeigen vielversprechendes Potenzial als Ersatz für rote Blutkörperchen in kritischen medizinischen Szenarien wie Notfällen, Traumata und großen Operationen, bei denen eine schnelle und effiziente Sauerstoffzufuhr lebenswichtig ist. Trotz ihrer potenziellen Vorteile wurde ihre klinische Anwendung durch ein begrenztes Verständnis ihrer Wechselwirkungen mit Immunzellen behindert. In dieser Studie haben wir die Auswirkungen von A−AOCs auf Immunreaktionen unter Verwendung von drei Makrophagen-Modellen bewertet: primären humanen Makrophagen (PHM), murinen Makrophagen (Zellinie J774) und murinen Makrophagen differenziert aus Knochenmark (BMDM). Unsere Ergebnisse zeigen, dass 10 ng/ml Phorbol 12-Myristat 13-Acetat (PMA) eine stabile Differenzierung von THP-1-Zellen in PHM gewährleisteten. A−AOCs zeigten Potenzial zur Minderung von Zell-Extravasation und Migration in PHM und zeigten eine gute Verträglichkeit bis zu einer Konzentration von 4%, ohne in den drei Makrophagen-Modellen signifikante Zytotoxizität zu induzieren. Protein- und Genexpressionsanalysen zeigten, dass A−AOCs bis zu einer Konzentration von 10 % diese Makrophagen nicht aktivierten. Insgesamt zeigten unsere Ergebnisse, dass Makrophagen tatsächlich A−AOCs internalisierten, wie durch Transmissionselektronenmikroskopie (TEM), konfokale Laserscanning-Mikroskopie (LSM) und korrelative Licht- und Elektronenmikroskopie (CLEM) bestätigt wurde. Allerdings wurde nach der Internalisierung keine anschließende Aktivierung durch A−AOCs beobachtet, wie durch unsere Zytokin- und mRNA-Messungen bestätigt wurde. Darüber hinaus beeinflussten A−AOCs den Sauerstoffverbrauch nicht und induzierten keinen oxidativen Stress in PHM in signifikantem Maße. Die vorliegende Untersuchung liefert Einblicke in die Wechselwirkungen von A−AOCs mit Immunzellen und unterstützt ihre potenzielle Anwendung als Sauerstoffträger in kritischen medizinischen Situationen.

Schlüsselwörter: albuminumhüllte perfluorocarbonbasierte künstliche Sauerstoffträger, Makrophagen, Immunreaktion, Zytotoxizität, Zelldifferenzierung, Sauerstoffverbrauch, Aufnahme von Nanopartikeln, Entzündung.

3. Introduction

The development of artificial oxygen carriers (AOCs) has been a subject of considerable interest in the field of medicine, particularly in situations where traditional blood transfusion may not be feasible or ideal [1]. One promising class of AOCs is albumin-derived perfluorocarbon-based artificial oxygen carriers (A−AOCs), which have shown great potential in oxygen delivery [2–4]. However, the interaction between A−AOCs and the immune system is a critical aspect to consider in their successful clinical implementation. A−AOCs are designed to mimic the oxygen-carrying capacity of red blood cells while possessing unique properties. These AOCs consist of perfluorocarbon (PFC) nanoparticles encapsulated within albumin, a naturally occurring protein with excellent biocompatibility [5,6]. The PFC core provides a reservoir for oxygen storage and release, while the albumin shell aids in stabilization and circulation within the bloodstream. Due to their recognizable patterns by immune cells, foreign substances, including A−AOCs, can be perceived as foreign objects and processed by the innate immune system [7,8]. Within the immune system, macrophages play a critical role in recognizing and responding to such foreign substances [9]. To evaluate the biocompatibility and immune interactions of these innovative oxygen-carrying systems, it is essential to understand how macrophages specifically respond to A−AOCs. This recognition triggers a cascade of events involving phagocytosis, antigen presentation, and the release of pro-inflammatory cytokines [10,11]. To optimize the clinical use of AOCs, it is crucial to modulate the immune response. Strategies such as surface modifications, coating with biocompatible materials such as albumin can be employed to minimize adverse immune reactions [12,13]. These approaches aim to reduce the recognition and subsequent activation of immune cells, promote immune tolerance, and enhance the biocompatibility of AOCs.

Understanding the immune cell response to A−AOCs is essential for evaluating their immunomodulatory effects and potential clinical applications. In this study we conducted comparative studies using different macrophage sources for this purpose. These sources include the human monocytic leukaemia cell line (THP-1), which can be induced to differentiate into adherent macrophage-like cells using phorbol-12-myristate-13-acetate (PMA). The differentiated THP-1 cells have proven to be a suitable *in vitro* model for studying macrophage functions [8]. In addition to THP-1 cells, this study utilized the murine macrophage cell line (J774) and primary murine macrophages (bone marrow-derived macrophages: BMDM) as valuable sources. These cell lines were employed to gain further insights into the complex interactions between A−AOCs and the immune system [14,15].

4. Theoretical background

4.1. Artificial oxygen carriers as blood substitute

Allogenic red blood transfusion is a critical medical intervention used to save lives, with thousands of patients receiving red blood cell concentrates daily to address severe blood loss or anaemia [16]. This transfusion method allows organs to maintain normal functioning and ensures vital blood functions such as oxygen delivery [17]. However, allogeneic blood transfusions have significant limitations, including a shortage of donors, concerns about contamination, delayed wound healing after surgery, transfusion reactions, acute lung injury, and immunomodulation [18,17]. Furthermore, many adverse issues are associated with incorrect blood group matching in patients [18]. In Sub-Saharan African countries like Cameroon, blood transfusion faces two main challenges: a high demand for transfusions in sick children, primarily due to malaria-related anaemia, and in young women due to obstetric haemorrhages. Additionally, there is a shortage of blood donors due to the lack of acceptance of blood donation. Human immunodeficiency viruses (HIV) and other transfusion-transmitted infections also remain prevalent in these countries.

In European countries including Germany, blood transfusion also experiences a high demand but a slight decrease in blood donors. This trend is expected to continue, primarily due to population aging [19,1]. About 65 % of the German population falls within the age group of 15-65 years, which is the prime age range for blood donors [19,20]. However, the majority of blood recipients are individuals above the age of 65 who are less likely to be able to donate blood [19]. This creates a challenging situation where the demand for blood increases with age, while the potential pool of donors diminishes [20].

Given the limitations and challenges associated with relying solely on blood donations to meet the demand for blood transfusions, the development of an alternative solution is crucial. Presently, two distinct categories of AOCs exist, categorized by their oxygen transport mechanisms: hemoglobin-based artificial oxygen carriers (HbOCs), where oxygen forms a covalent bond with hemoglobin; and perfluorocarbon-based artificial oxygen carriers (PFCOCs), wherein oxygen is physically dissolved within perfluorocarbons [21,22]. Artificial oxygen carriers, such as PFCOCs or HbOCs offer several advantages [21,23]. AOCs can be synthetized in large quantities on demand, reducing the risk of disease transmission as they are highly purified [21,23]. They eliminate the need for ABO blood group matching since they are

non-antigenic, and they have convenient storage properties [23]. AOCs resemble natural hemoglobin in terms of oxygen and carbon dioxide transport and delivery and have a sufficient half-life in circulation. AOCs have shown potential in various clinical settings, including the treatment of decompression sickness, as targets for medicines, and as oxygen therapeutics [24]. They are not a complete substitute for blood since blood has additional functions like providing essential nutrients and immune protection. However, AOCs can effectively carry oxygen to tissues and remove carbon dioxide, making them a valuable tool when allogeneic red blood cells are not feasible due to medical or religious reasons, or in situations where targeted oxygen delivery is required [25,21,26].

While the development of AOCs has made progress, challenges remain. Inflammatory reactions, conservation methods, and oxygen affinity are among the major obstacles that need to be addressed to ensure the clinical viability of AOCs [27,1]. Both hemoglobin-based and perfluorocarbon-based oxygen carriers have undergone preclinical and clinical investigations; however, they have not yet obtained approval for human application in Western Europe or the USA [28,22]. Clinical trials and studies have been conducted on perfluorocarbon-based blood substitutes such as Fluosol-DA®, Perftoran®, Oxygent™ and Oxycyte®, but none of them is approved in Western Europe or the USA due to side effects that have occurred [29]. Moreover, a recent meta-analysis revealed increased mortality among patients treated with hemoglobin-based blood substitutes [18,17]. Therefore, further research is necessary to demonstrate the safety and efficacy of AOCs before they can be routinely used in clinical settings [30].

Despite the ongoing challenges, the search for blood substitutes remains a worthwhile endeavor, especially considering the urgent need for alternative solutions in areas with deficient medical care and transfusion services [21]. Moreover, AOCs have the potential to provide an additional tool for physicians when blood donors are scarce or when specific medical conditions require oxygen delivery [25,30]. Given our research focus on PFCOCs, it is essential to delve deeper into the specifics of these innovative substances. In the following paragraphs, we will explore the unique characteristics and potential applications of PFCOCs.

4.2. Perfluorocarbon-based artificial oxygen carriers (PFCOCs)

Perfluorocarbons (PFCs) are synthetic compounds that possess unique properties due to the replacement of hydrogen atoms with fluorine atoms in their hydrocarbon structure [31–33].

They exhibit excellent gas solubility and can dissolve substantial amounts of gases, including oxygen, carbon dioxide, and others [32,33]. PFCs are chemically and biologically unreactive and do not mix with water. Consequently, when used as blood substitutes, emulsifiers are necessary to facilitate their integration into the bloodstream [32]. The solubility coefficient of PFCs for oxygen surpasses that of oxygen dissolved in plasma [31,34] (see figure 1). This characteristic, coupled with their fluidity and low surface tension, makes pure PFCs well-suited for liquid ventilation, particularly in cases of acute respiratory distress syndrome, where they enhance oxygenation.

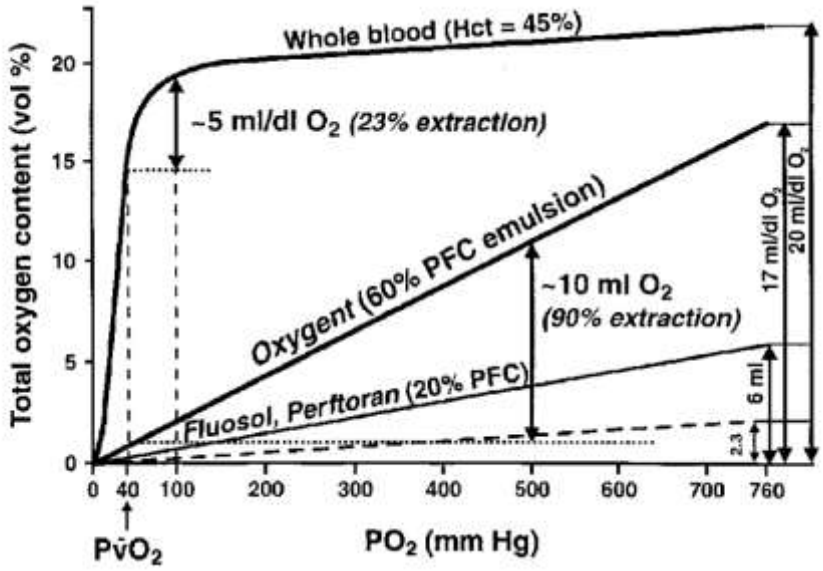

Figure 1: Solubility of oxygen

In fluorocarbons, the solubility of oxygen adheres to Henry's law, meaning it is directly proportional to the partial pressure of the gas. This behavior is anticipated because there is no chemical bonding involved. In contrast, hemoglobin forms a strong covalent (coordination) bond with oxygen at its iron atoms, leading to saturation at pO2 levels higher than those present in Earth's atmosphere. Oxygen extraction from a PFC emulsion has the potential to achieve a remarkable 90 % of oxygen content [32].

PFC emulsions have shown promising results as oxygen carriers, benefitting from the inert nature of PFCs and their high solubility for oxygen and carbon dioxide. Among the various PFCs, perfluorodecalin (PFD) and perfluorooctyl bromide (PFOB) are the most commonly used [31,35]. PFD is a synthetic fluorocarbon compound extensively studied for its ability to carry and deliver oxygen to cells in the body [35,31,36,37]. With its high oxygen solubility (dissolving 40 ml of oxygen per 100 ml of PFD at room temperature and pressure), PFD can efficiently dissolve a significant amount of oxygen and transport it [35]. Its unique physicochemical properties, such as low viscosity and high gas solubility, make it an ideal

candidate as an oxygen carrier. PFCOCs hold great promise as alternatives for oxygen delivery in various medical applications. They possess a high oxygen-carrying capacity and solubility due to the strong affinity of PFCs for oxygen. These carriers can be administered intravenously, facilitating efficient oxygen transport to tissues and cells [21]. By dissolving oxygen in their liquid phase, PFCOCs create an oxygen-rich dispersion that readily releases oxygen to oxygen-deprived tissues [26]. Moreover, PFCOCs as synthetic products, are compatible with different blood types, eliminating the need for blood typing and matching [23]. An important benefit of PFCOCs is their capability to improve tissue oxygenation in situations of hypoxia or insufficient oxygen availability [21,4]. By increasing the oxygen-carrying capacity of the blood, PFCOCs improve oxygen delivery to vital organs and tissues, thereby improving patient outcomes in critical situations. Additionally, PFCs exhibit low reactivity with biological molecules and have a long half-life in the bloodstream, providing extended oxygen-carrying capability. Despite their promising characteristics, no PFCOCs are currently approved for clinical use in western Europe or USA. Some PFCs, like Fluosol-DA®, faced challenges due to adverse effects of the surfactants used. Others, such as Oxypherol, had excessively long organ retention, rendering them unsuitable for human use [21]. However, certain PFCOCs, like Perftoran® and Oxygent™, have shown beneficial effects in preclinical and clinical studies. Perftoran® demonstrated efficacy in various medical conditions. It was approved for clinical use in Russia for temporary intravascular oxygen delivery in cases of hemorrhagic shock and perfusion of human organs. It has also been approved for medical use in other countries. Perftoran® faced criticism for its long organ half-life, low emulsion stability, and short shelf life without freezing [22]. Oxygent™ exhibited positive outcomes in tissue oxygenation and myocardial functional recovery. However, some signs of immunomodulation were observed in subjects experiencing febrile responses and a dose-dependent increase in minor flu-like symptoms 24 h after administration [38]. Although PFCOCs offer significant advantages as artificial oxygen carriers, further research is necessary to optimize their stability, biocompatibility, and elimination from the body. Considering these limitations, a novel oxygen carrier called albumin-derived perfluorocarbon-based artificial oxygen carriers (A−AOCs) has been developed. More detailed information about A−AOCs will be provided in the subsequent paragraph.

4.3. Albumin-derived perfluorocarbon-based artificial oxygen carriers

4.3.1. Albumin

Albumin is a crucial protein found in the blood plasma, constituting approximately 55-60 % of total plasma proteins in humans [5]. It plays a vital role in maintaining the body's overall homeostasis and performing various physiological functions [39]. One of its primary functions is to regulate osmotic pressure within blood vessels, preventing excessive fluid leakage into surrounding tissues [40]. This property ensures proper hydration, and it also helps prevent the development of edema. Albumin acts as a carrier protein, responsible for transporting a diverse range of substances throughout the body, including hormones, fatty acids, drugs, and bilirubin [41]. Additionally, it contributes to the regulation of blood pH by buffering acids and bases, thus maintaining the body's acid-base balance [42]. Albumin also plays a significant role in the immune response, acting as an antioxidant that scavenges free radicals and protects against oxidative stress [43]. Albumin derived from human plasma or recombinant technology, undergoes meticulous purification processes, and is subjected to stringent quality control measures to ensure its safety and efficacy [6]. The safety of albumin for clinical use is well-established. While hypersensitivity reactions or allergic responses may occur in rare instances, they are infrequent and manageable with appropriate precautions. The risk of viral transmission has been significantly reduced through rigorous donor screening, plasma testing, and advanced manufacturing techniques [6]. Moreover, albumin exhibits compatibility with a wide range of medications and therapies, making it a versatile and reliable option in clinical practice. Its extensive clinical use and well-established safety record reinforce its status as a trusted and essential component in patient care [41]. Beyond its clinical applications, albumin's unique properties have made it an ideal candidate for various biomedical purposes [41]. Its solubility, stability, and biocompatibility have led to its use as a drug carrier, diagnostic marker, and therapeutic agent [41]. With multiple binding sites and conformational flexibility, albumin can bind and transport diverse molecules efficiently. Its long circulation half-life and extravasation ability make it suitable for targeted drug delivery [41]. Notably, albumin has emerged as a promising shell material for artificial oxygen carriers. These carriers, based on albumin, offer advantages such as low immunogenicity, high biocompatibility, and tunable oxygen release kinetics [2,4,44]. By modifying albumin's structure or conjugating it with oxygen-carrying molecules, its oxygen-binding capacity can be enhanced [44]. The albumin shell protects the oxygen load, ensuring controlled and sustained oxygen delivery with minimized side effects.

Surface modifications can further improve stability, circulation time, and target-specific binding, enabling precise drug delivery to specific tissues or organs [12,45]. Thus, albumin's exceptional properties make it a versatile platform for various biomedical applications, including the design of artificial oxygen carriers [46]

4.3.2. Significance of Albumin-derived perfluorocarbon-based artificial oxygen carriers

A−AOCs were developed to address the limitation of the previous developments without the albumin shell, which were instable and had a short half-life [3]. The synthesis procedure involves utilizing albumin in conjunction with ultrasound or high pressure to create an amphiphilic albumin shell that encapsulates a core of perfluorodecalin (see figure 2). This innovative approach eliminates the need for additional emulsifiers when administering them intravenously [2,4]. *In vitro* tests have demonstrated the effective oxygen transport capacity of A−AOCs, supported by experiments in Langendorff-heart-model and in vivo rat studies on toxicity and pharmacokinetics [2,3]. Intravenous application of A−AOCs in rats showed good tolerance, stable vascular perfusion, and no significant deviations in systemic parameters or tissue injury. The half-life of A−AOCs was deemed sufficient, and a proof-of-concept study exhibited the survival of rats after replacing 95 % of their blood with A−AOCs. A−AOCs also exhibited a higher oxygen transport capacity than a competitor product, Perftoran® [2]. Another study demonstrated the preventive use of A−AOCs before air diving, resulting in higher survival rates, longer survival times, and reduced symptoms compared to a group that received serum albumin only [36]. These findings suggest the potential of albumin-derived perfluorocarbon-based artificial oxygen carriers as blood substitutes. As red blood cell substitute, A−AOCs are applied directly into the body through an intravenous injection. In the body, the first cells that are in contact with A−AOCs are endothelial cells and immune cells, among which macrophages are of major importance. Although A−AOCs are well established in our research group [2–4,47], interactions with immune cells have not been investigated so far.

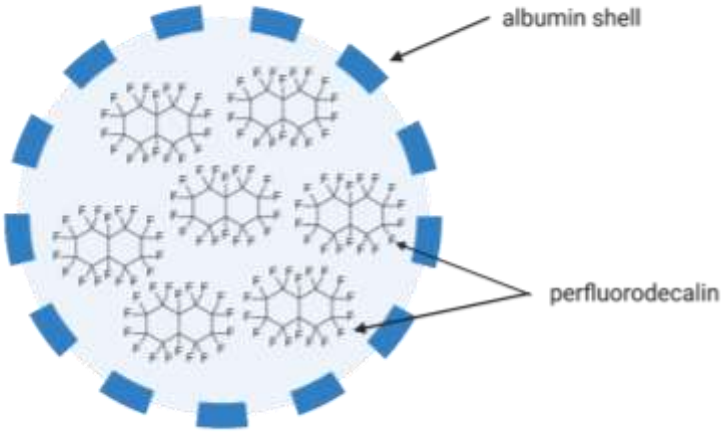

Figure 2: Albumin-derived perfluorocarbon-based artificial oxygen carrier

An Albumin-derived perfluorocarbon-based artificial oxygen carrier (A-AOC) consisting of a gas-permeable albumin shell that encloses a core made of perfluorodecalin (Created with BioRender.com).

4.4. Cellular uptake and clearance of artificial oxygen carriers

Artificial oxygen carriers are designed to deliver oxygen to tissues and organs when natural oxygen-carrying capacity is compromised [47]. The uptake of these carriers by cells involves intricate interactions influenced by several factors. The physicochemical properties of the artificial oxygen carriers, such as size, surface charge, and composition, play a critical role in determining their cellular uptake efficiency [31]. Additionally, the characteristics of the cells themselves, including their membrane properties and receptor expression, contribute to the uptake process. Various mechanisms, such as endocytosis, phagocytosis and pinocytosis, or direct penetration of the cell membrane, may be involved in the internalization of artificial oxygen carriers [48]. Different cell lines exhibit variations in their ability to take up artificial oxygen carriers. This variability can be attributed to variations in cell membrane composition, receptor expression, and cellular functions. For instance, phagocytic cells, such as macrophages, have a higher tendency to engulf larger artificial oxygen carriers through endocytosis [8]. Once internalized, artificial oxygen carriers can follow various intracellular trafficking pathways [49]. They may be directed to lysosomes for degradation, released into the cytoplasm, or transported to specific organelles. The clearance of artificial oxygen carriers from the body is a critical aspect to consider for their safe and effective use in biomedical applications [49]. Several clearance pathways are involved in the removal of these particles from the

systemic circulation. One of the primary clearance mechanisms is through the reticuloendothelial system, particularly the liver and spleen, which play a vital role in filtering and eliminating nanoparticles from the bloodstream [31]. Additionally, nanoparticles can be cleared through the renal system, where they are filtered by the kidneys and eventually excreted in the urine [50]. The size, surface properties, and surface charge of artificial oxygen carriers influence their clearance kinetics, with smaller particles typically being cleared more rapidly than larger ones. Furthermore, the stability and biodegradability of nanoparticles can also impact their clearance from the body. An optimal clearance of artificial oxygen carriers from the body is essential to avoid accumulation and prolonged organ retention [31].

4.5. Macrophages and immune response

Macrophages are specialized phagocytic cells that play a crucial role in the innate immune system. They have diverse functions, including recognizing, engulfing, and breaking down cellular debris, pathogens and foreign objects [9]. Phagocytosis, the process by which macrophages engulf and eliminate pathogens, foreign particles, and cellular debris, is a fundamental aspect of their function [51]. This process is triggered by the recognition of microbial patterns by surface receptors on macrophages, leading to phagocytosis and subsequent intracellular signalling events [52]. Macrophages' ability to phagocytose contributes to immediate defence against infections and the initiation of subsequent immune responses. Furthermore, macrophages participate in antigen presentation to T cells, serving as a bridge between innate and adaptive immunity [52]. They capture, process, and present antigens to T lymphocytes, initiating adaptive immune responses. Acting as antigen-presenting cells (APCs), macrophages express major histocompatibility complex (MHC) molecules, co-stimulatory molecules, and cytokines necessary for T cell activation [53].

In addition to their immune responses, macrophages also play a vital role in initiating inflammation by releasing cytokines and chemokines, which recruit other immune cells to the site of inflammation [10]. They are potent producers of these signalling molecules, regulating inflammation, immune cell recruitment, and tissue repair [10]. Pro-inflammatory cytokines such as tumour necrosis factor-alpha (TNF-alpha) and interleukin-1 beta (IL-1beta) contribute to pathogen defence and inflammation, while anti-inflammatory cytokines like interleukin-10 (IL-10) promote immune resolution and tissue repair. Another significant role of macrophages is immunomodulation, as they regulate immune cell functions and maintain immune tolerance

[54,55]. They interact with other immune cells such as dendritic cells, B cells, and T cells to shape the immune response. Macrophage-derived factors, including IL-10 and transforming growth factor-beta (TGF-β), promote regulatory T cell development and suppress excessive immune activation [53]. However, a dysregulation of macrophage functions is associated with various immune-related disorders such as sepsis [56,57].

Macrophages can originate from different sources, such as circulating monocytes derived from hematopoietic stem cells in the bone marrow or develop during embryonic development [58]. They exhibit different morphologies and phenotypes depending on their tissue location and function. Examples of tissue-resident macrophages include osteoclasts (bone), microglia (central nervous system), histiocytes (connective tissue), Kupffer cells (liver), dust cells (alveoli), and macrophages in the intestine, spleen, and peritoneum [58]. Macrophages are pivotal in integrating innate and adaptive immunity through their roles in phagocytosis, antigen presentation, cytokine secretion, tissue repair, and immunomodulation. Understanding the intricacies of macrophage functions and their regulation in different contexts is crucial for developing targeted therapies for immune-related disorders [54]. Furthermore, by comprehending the interactions between macrophages and AOCs, strategies can be developed to enhance the biocompatibility and therapeutic efficacy of AOCs.

4.5.1. Activation of Macrophages

Macrophages can become activated in two different ways: classically or alternatively [59]. When macrophages are activated in a classical manner, they are often referred to as M1 macrophages [60]. In laboratory experiments, M1 macrophages can be generated by introducing pathogens, LPS (lipopolysaccharide), granulocyte macrophage-colony stimulating factor (GM-CSF), TNF-alpha, or interferon gamma (IFN-γ) into the culture medium containing the cells [61]. The generation of M1 macrophages involves various pathways depending on the substance used, such as the interferon regulatory factor/signal transducer and activator of transcription (IRF/STAT), lipopolysaccharide/toll-like receptor 4 (LPS/TLR4), and nuclear factor-kappa B/phosphatidylinositol 3-kinase (NF-κB/PI-3 kinase) pathways [62]. M1 macrophages exhibit distinct characteristics, including strong antigen presentation [10] ability and high production of pro-inflammatory cytokines like interleukin 1 (IL-1), IL-6, TNF-alpha, as well as nitric oxide (NO) and reactive oxygen species (ROS) [11,10]. Additionally, M1

macrophages express high levels of major histocompatibility complex class II (MHC II), CD68, CD80, CD86, and Th1 cell-attracting chemokines, such as CXCL9 and CXCL12 [63,64].

Alternatively activated macrophages, known as M2 macrophages, are generated in response to parasitic or fungal infections, immune complexes, apoptotic cells, macrophage colony-stimulating factor (M-CSF), IL-13, TGF-b, T helper 2 (Th2) cytokine IL-4, as well as IL-33 and IL-25 through Th2 cells [65]. The transition of macrophages into the M2 state involves signalling pathways mediated by STAT6, IRF4, peroxisome proliferator-activated receptor delta (PPARδ), and peroxisome proliferator-activated receptor gamma (PPARγ). M2 macrophages exhibit lower production of inflammatory cytokines like IL-1, IL-6, and TNF-α [66,67]. These macrophages are important in pathogen clearance, anti-inflammatory responses, metabolism, wound healing, tissue remodelling, immunoregulation, tumour progression and malignancies [68]. M2 macrophages are characterized by the expression of CD206, CD163, CD209, FIZZ1, and Ym1/2. Chemokines expressed by this macrophage type include CCL1, CCL17, CCL18, CCL22, and CCL24 [69]. In contrast to classically activated (M1) macrophages that elicit a strong pro-inflammatory response, alternatively activated (M2) macrophages are associated with anti-inflammatory functions [70] (see figure 3).

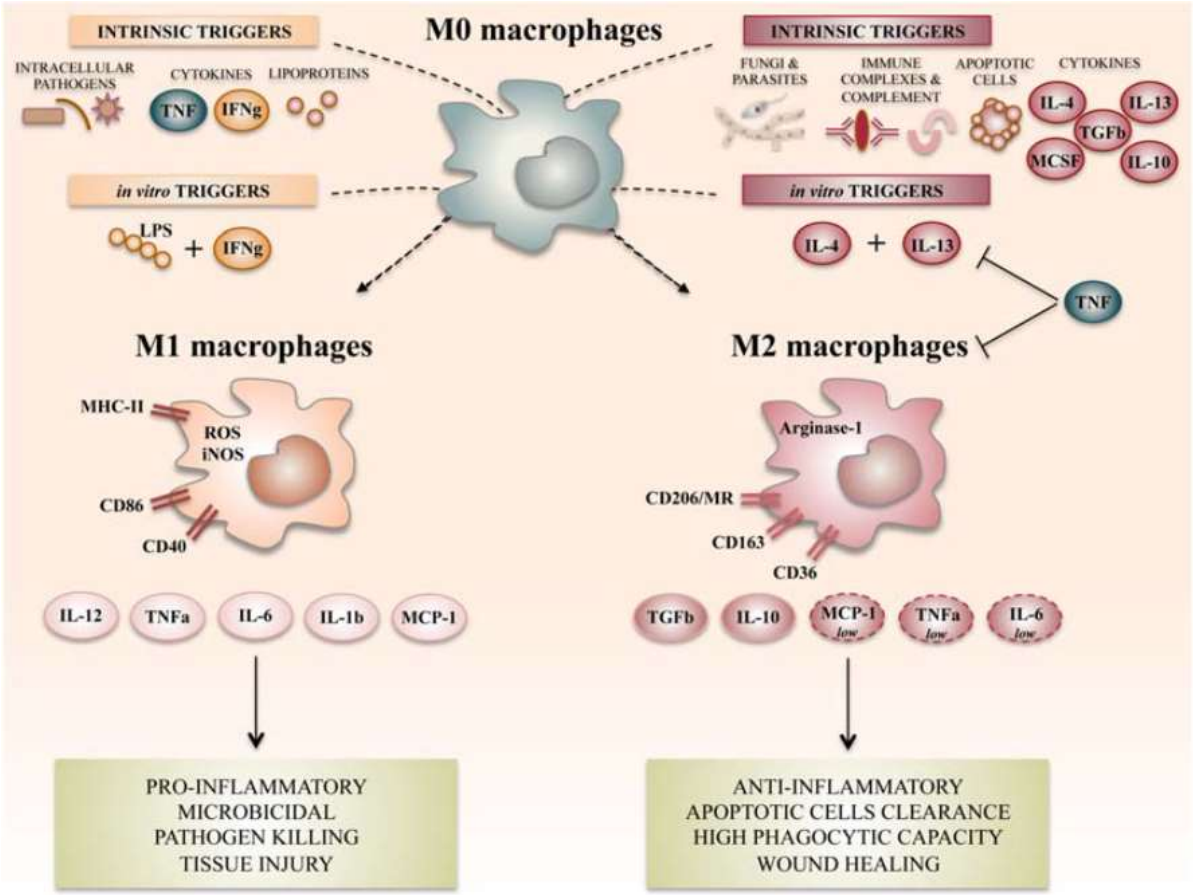

Figure 3: Summary of the primary polarization states of activated macrophages

Various stimuli and signaling pathways have been identified as triggers for M1-like or M2-like activation states, which are outlined here. In humans, M1-like or M2-like polarization has been associated with distinct defensive or healing functions. These polarization statuses serve multiple roles, with the classical association of pro- and anti-inflammatory macrophage activation linked to the M1-like/M2-like dichotomy. Specific inducers and markers for these states include LPS (lipopolysaccharide), MR (mannose receptor), TNF (tumor necrosis factor), IFNg (interferon gamma), IL (interleukin), MCP (monocyte chemoattractant protein), TGF (transforming growth factor), MCSF (macrophage colony-stimulating factor), ROS (reactive oxygen species), iNOS (inducible nitric oxide synthase), and MHC (major histocompatibility complex) (figure adapted from Atri et al. 2018).

4.5.1.1. Cellular adhesion: intercellular adhesion molecule 1 (ICAM1)

Cellular adhesion plays a crucial role in cell-to-cell interactions, and one key molecule involved in this process is intercellular adhesion molecule-1 (ICAM-1). ICAM-1 is a transmembrane glycoprotein with a structure similar to immunoglobulin G (IgG). Its molecular weight can vary from 60 to 114 kDa, depending on the degree of glycosylation on its Ig domains [71]. ICAM-1

is primarily known for mediating leukocyte adhesion to endothelial cells, facilitating the movement of leukocytes across the vascular wall [72]. During inflammatory processes, ICAM-1 expression is upregulated in various cell types, including macrophages. Studies have shown that ICAM-1 expression is induced during inflammatory macrophage polarization. Increased numbers of ICAM-1-expressing macrophages have been observed in inflamed colon tissue in a murine colitis model and in human inflammatory bowel disease [72]. Furthermore, ICAM-1 plays a role in facilitating the binding of macrophages to apoptotic cells [72]. Activation of macrophages, such as by lipopolysaccharide (LPS) exposure, can induce ICAM-1 expression, making it a potential marker for macrophage activation [73]. Overall, ICAM-1 is a crucial molecule involved in cellular adhesion and is dynamically regulated during inflammatory processes, playing a role in leukocyte recruitment and macrophage function [71,74]. Furthermore, Myeloid cells, such as macrophages, recruited to sites of bacterial inflammation encounter challenging conditions characterized by low oxygen levels (hypoxia) and high concentrations of inflammatory cytokines, which have a significant impact on their function [75]. Hypoxia often accompanies bacterial inflammation due to an increased oxygen demand, disrupted blood flow, or an altered oxygen utilization [75,76]. The primary regulator of hypoxia response, hypoxia-inducible factor 1 alpha (HIF-1α), is primarily controlled by oxygen levels [75]. However, ICAM-1 upregulation was observed in hypoxic tissue, where HIF-1 and NFκB signalling pathways are predominantly activated [71]. This suggests the presence of an indirect connection between ICAM-1 and HIF-1α through inflammatory and hypoxia-related signalling pathways.

4.5.1.2. Cellular migration of macrophages

Cellular migration of macrophages is a fundamental process essential for their diverse functions in immune responses and tissue homeostasis [77]. Macrophages, as key players of the innate immune system, exhibit remarkable plasticity and can adopt different phenotypes in response to microenvironmental signals. Their migration is crucial for various physiological and pathological processes, including immune surveillance, inflammation, wound healing, and tissue remodelling [78]. Macrophages migrate in response to chemotactic signals generated by damaged tissues or inflammatory stimuli, guided by chemokines and their corresponding receptors [79]. The migration of macrophages involves intricate cellular mechanisms, including cytoskeletal rearrangements, adhesion molecule interactions, and proteolytic remodelling of the

extracellular matrix [79]. Through their migratory capabilities, macrophages can efficiently navigate tissues, infiltrate inflammatory sites, and interact with other immune cells, contributing to the resolution of inflammation, tissue repair, and host defence [78,79]. Migration of activated macrophages is crucial for their recruitment to sites of inflammation, infection, or tissue damage.

4.5.2. Inflammation

Inflammation is a complex physiological response triggered by various stimuli, including tissue injury, infection, or immune dysregulation [80]. It plays a crucial role in the body's defense mechanisms and tissue repair processes. One key aspect of inflammation is the activation of hypoxia-inducible factor 1 (HIF-1) related genes and the involvement of oxidative stress [81]. HIF-1 is a transcription factor that regulates the cellular response to hypoxia, but its role extends beyond oxygen sensing. HIF-1 activation during inflammation is not only influenced by oxygen levels but also by the interplay of immune cells, cytokines, and other inflammatory mediators [81]. Additionally, inflammation is associated with increased oxidative stress, characterized by an imbalance between the production of ROS and the ability of antioxidant defenses to neutralize them [82,81] . The interaction between HIF-1 related genes and oxidative stress in the context of inflammation offers insights into the molecular mechanisms underlying inflammatory responses.

4.5.2.1. HIF-1 related genes and inflammatory conditions

Hypoxia-inducible factor 1 (HIF-1) and its related genes have emerged as critical players in the regulation of inflammatory conditions [83]. HIF-1 is a transcription factor that is activated in response to low oxygen levels, but it also responds to various other stimuli, including inflammation. Inflammatory conditions are characterized by the release of pro-inflammatory cytokines, chemokines, and other immune mediators, which can activate HIF-1 signaling [83]. HIF-1 activation in inflamed tissues contributes to the modulation of immune responses, as it regulates the expression of genes involved in angiogenesis, metabolism, cell survival, and inflammation itself [84]. HIF-1 promotes the production of inflammatory mediators, such as IL-1beta, TNF-alpha, and inducible nitric oxide synthase (iNOS), thereby amplifying the inflammatory cascade [83,84]. Moreover, HIF-1 influences the recruitment and activation of

immune cells, including macrophages and neutrophils, which are key players in the initiation and resolution of inflammation. The interplay between HIF-1 and inflammatory pathways is complex and tightly regulated, and dysregulation of this interaction can contribute to the pathogenesis of various inflammatory disorders. Understanding the role of HIF-1 related genes in inflammatory conditions provides valuable insights into the molecular mechanisms underlying inflammation.

4.5.2.2. The interplay of oxygen consumption, oxidative stress, and inflammatory conditions in macrophages

Macrophages, being highly metabolically active cells, consume a significant amount of oxygen to perform their various functions, such as phagocytosis and the oxygen burst [85]. The oxygen burst, which involves the rapid release of ROS during macrophage activation, serves as a potent mechanism for killing pathogens and initiating antimicrobial responses [85,86]. As macrophages become activated, their oxygen consumption rates increase in parallel with the oxygen burst, providing the energy required for the immune response [86]. This increased oxygen consumption supports the generation of ROS by the nicotinamide adenine dinucleotide phosphate (NADPH) oxidase enzyme complex. The balance between oxygen consumption and the oxygen burst ensures an adequate oxygen supply for macrophage activation and ROS production, effectively eliminating pathogens [87]. Macrophages have evolved intricate defense mechanisms to maintain redox homeostasis, including enzymatic antioxidants (superoxide dismutase and catalase) and non-enzymatic antioxidants (glutathione). However, excessive ROS production or impaired antioxidant defenses can lead to oxidative stress and damage cellular components, triggering inflammation and further ROS release [88]. This interplay between oxygen consumption, ROS generation, and oxidative stress plays critical roles in macrophage function, immune response, and the elimination of pathogens. Furthermore, oxidative stress can perpetuate inflammation and hinder tissue repair processes, highlighting the importance of maintaining redox homeostasis in macrophages and other immune cells. [89].

4.6. Cell death

Cell death is a fundamental biological process that plays a critical role in various physiological and pathological contexts [90]. Two prominent modes of cell death are characterized by distinct mechanisms and morphological features: necrosis and apoptosis [90]. Apoptosis, also known as programmed cell death, is a tightly regulated process involved in development, tissue homeostasis, and immune responses [90,91]. It is characterized by specific cellular changes, including nuclear condensation, DNA fragmentation, membrane blebbing, and the formation of apoptotic bodies [92]. In contrast, necrosis is generally considered an uncontrolled and accidental form of cell death that is associated with inflammation or tissue damage [93]. During cell death, various molecular events occur, leading to the release of intracellular components into the extracellular environment. Lactate dehydrogenase (LDH) release and the terminal deoxynucleotidyl transferase dUTP nick end labeling (TUNEL) assay are two commonly used methods for assessing cell death.

4.6.1. Lactate dehydrogenase (LDH) release

LDH release is a widely used method to assess cell death and cytotoxicity [94]. LDH is an intracellular enzyme that is present in various tissues and cells, including red blood cells, heart, liver, and other organs. Under normal physiological conditions, LDH remains within the cells, but when cell membrane integrity is compromised, LDH is released into the extracellular space [94]. This can occur due to various factors, such as cellular damage, injury, or cell death. Measurement of LDH release serves as an indicator of cellular damage and loss of membrane integrity. The assay involves quantifying the amount of LDH released from cells into the culture medium or biological samples by measuring the conversion of lactate to pyruvate (see figure 4). LDH release assays are commonly used in research and clinical settings to evaluate cell viability, assess cytotoxicity of substances or treatments, and monitor cell death in different experimental models [94,95]. LDH release is seen as an early occurrence in necrosis, whereas it occurs later in the process of apoptosis. Measuring LDH release, allow to gain insights into the extent and mechanisms of cell death, which is essential for understanding disease processes, evaluating drug efficacy or toxicity, and developing therapeutic strategies.

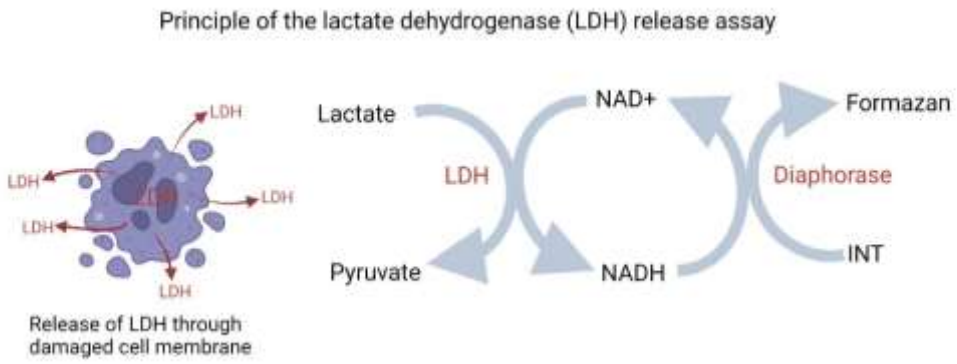

Figure 4: Principle of the lactate dehydrogenase (LDH) assay

The LDH assay principle relies on the conversion of lactate present in the sample and excess NAD+ in the buffer to pyruvate and NADH through the action of lactic dehydrogenase, accompanied by the simultaneous conversion of nitroblue tetrazolium to formazan, resulting in the formation of a red precipitate (created with BioRender.com).

4.6.2. Apoptosis:TUNEL assay

Apoptosis is a highly regulated form of programmed cell death that plays a crucial role in various physiological and pathological processes. The TUNEL (Terminal deoxynucleotidyl transferase dUTP Nick End Labeling) assay is a widely used technique to detect and visualize apoptotic cells [96]. The assay utilizes the ability of the enzyme terminal deoxynucleotidyl transferase (TdT) to incorporate labeled nucleotides at the free 3'-OH ends of DNA breaks, which are characteristic of apoptotic cell death. By labeling the fragmented DNA, the TUNEL assay allows for the identification and quantification of apoptotic cells. This technique provides valuable insights into the extent and distribution of apoptosis within tissues and experimental models [96].

4.7. Aim of the study

A−AOCs have emerged as innovative therapeutic agents for addressing critical oxygenation needs in various clinical scenarios. Understanding the interaction between A−AOCs and the immune system, particularly macrophages, is vital for assessing their biocompatibility, immune responses, and potential therapeutic applications. This study aims to investigate the immune system's response to A−AOCs through a comparative analysis of macrophage reactions. This analysis involved three commonly utilized macrophage models: primary human macrophages-like cells (PHM) a widely used *in vitro* model of macrophages, which result from the

differentiation of the human monocytic leukaemia cell line THP-1 into adherent macrophages by phorbol-12-myristate-13-acetate and murine macrophages (J774 and primary bone marrow-derived macrophages: BMDM).To assess the direct cytotoxicity of A−AOCs, viability tests including the LDH assay, tunnel assay were performed. Moreover, the impact of A−AOCs on cell migration and cell adhesion were determined to gain insights into their potential effects on cellular behavior. The biocompatibility profile of A−AOCs was further evaluated by examining the upregulation of immunologically relevant genes and proteins to elucidate the potential immunomodulatory effects of A−AOCs on macrophages and their role in immune responses. The uptake of A−AOCs was investigated using fluorescent dyes and electron microscopy to provide valuable information about the internalization mechanisms and intracellular localization of A−AOCs within macrophages. Lastly, oxygen consumption rate measurements and lipid peroxidation assay were performed to gain insights into potential metabolic and oxidative stress effects induced by A−AOCs exposure. By conducting these comprehensive analyses, we aim to gain a deeper understanding of the interaction between A−AOCs and macrophages, elucidating their biocompatibility, impact on cellular behavior, immunomodulatory potential, and cellular uptake.

5. Materials and methods

5.1. Laboratory equipment

The laboratory equipment used in this work is listed in table 1 below.

Table 1: Laboratory equipment, its designations, and manufacturers

Equipment	Designation	Manufacturer
Adjustable volume pipettes	Eppendorf Research® Plus G 0.5-10 ul/10-100 ul/100-1000 ul	Merck KGaA, Darmstadt, Germany
Autoklav	Systec VX-75	Systec GmbH, Linden, Germany
Balance	KERN 572	KERN, Balingen-Frommern, Germany
Benchtop centrifuge	uniCFUGE 5	LLG Labware, Meckenheim, Germany
Biological safety cabinet	HERAsafe	Thermo Fisher Scientific, Massachusetts, USA
Centrifuge	Biofuge primo R	Heraeus, Hanau, Germany
Confocal laser scanning microscope	LSM 5	Zeiss, Jena, Germany
Counting chamber	Neubauer Counting chamber	Becton Dickinson, Franklin Lakes, USA
Culture microscope	CK40	Olympus, Tokyo, Japan
Disperser	Ultra-Turrax T25 Basic	IKA-Werke, Staufen,
Dynamic light scattering (DLS)	Stabino NANO-flex	Particle Metrix, Meerbusch, Germany
ECL detection system	SuperSignalTM West Femto	Thermo cientific
Electrophoresis power supply		Bio-Rad, Düsseldorf, Germany

Epoch™ Microplate Spectrophotometer	Take3 plate	BioTek, Bad Friedrichshall, Germany
flow cytometer	FACSCanto™ II	BD Biociences, Heidelberg, Germany
Fluorescence mikroscope	Axiovert 100M	Zeiss, Jena, Germany
Fridge	Gastro line	Liebherr-International Germany, Biberach an der Riß, Germany
Fusion-FX7		PEQLAB Biotechnologie, Erlangen, Germany
Homogenizer	LM20 Microfluidizer	Microfluidics, Westwood, USA
Hypoxia station	Whitley H35	Don whitley scientific, West Yorkshire, UK
iCycler iQ5TM		Bio-Rad, Düsseldorf, Germany
Incubator	MCO-18AIC (UV)	SANYO, Osaka, JPN
Light microscope	AxioLab A.1	Zeiss, Jena, Germany
Objektive 10 x (light microscope)	A-Plan 10x/0.25	Zeiss, Jena, Germany
Objektive 20 x (light microscope)	A-Plan 20x/0,35	Zeiss, Jena, Germany
Objektive 40 x (light microscope)	A-Plan 40x/0.65	Zeiss, Jena, Germany
Objektive 40 x (LSM)	Achrostigmat 40x/1.3	

pH-Meter	765 Calimatic	Knick, Berlin, DEpH-Meter 765 Calimatic Knick, Berlin, Germany
Precision balance	ABT 220-5DNM	KERN, Balingen-Frommern, Germany
Respirometer	Oxygraph-2k	Oroboros Instruments, Insbruck, AUT
Roller pump	Rotarus standard 50	Hirschmann laboratory equipment, Eberstadt, Germany
Thermo Cycler	Biometra TOne	Biometra, Göttingen, Germany
Ultrapure water system	Q-Pod	Merck, Darmstadt, Germany
Ultraschallhomogenisator	UP 400 St	Hielscher, Teltow, Germany
Ultra-Turrax	T25 basic	IKA, Staufen, Germany
Vibrating mixer	GLW L46	Oehmen Labortechnik, Essen, Germany
Viscosimeter	MCR 92	Anton Paar, Ostfildern, Germany
Water bath	1002	GFL, Burgwedel, Germany
Water filter	Millipak Express 40	Merck, Darmstadt, Germany
Western Blot chamber	Mini Trans-Blot®	Bio-Rad, Düsseldorf, Germany

5.1. Consumables

The consumables used in this work are listed in table 2 below.

Table 2: Consumables used in this work

Consumable	Designation	Manufacturer
Cell culture flasks	T25, T75, T125	Sarstedt, Nümbrecht, Germany
Cell plates	6 well, 24 well, 96 well	Sarstedt, Nümbrecht, Germany
Cell scraper	Sterile Cell scraper	Sarstedt, Nümbrecht, Germany
Conical centrifuge tubes	15 ml, 50 ml	Sarstedt, Nümbrecht, Germany
Cover slips	hydrophobic	Engelbrecht, Edermünde, Germany
Gloves	Peha-soft-nitrile	Hartmann, Heidenheim, Germany
Ibidi dishes	ibidi Glass Bottom Dish 35 mm	Ibidi, Gräfelfing, Germany
Inserts	Transwell inserts (pore size 8 µm with 1-105 pores/cm^2)	Corning, Hagen, Germany
microscope slides	Superfrost™	Thermo Fisher Scientific, Massachusetts, USA
Paper towels	Prestige super soft	WEPA Professional, Arnsberg, Germany
Paraffin		McCormick Scientific, Missouri, USA
Pipette tips	10 µl, 200 µl, 1000 µl	Sarstedt, Nümbrecht, Germany
Plastic bags	18 cm x 30 cm	

Polyvinylidene fluoride (PVDF) membrane		Bio-Rad, Düsseldorf, Germany
Reaction tubes (safe lock)	0.5 ml	Eppendorf, Taufkirchen, Germany
Reagent tubes	1.5 ml, 2.0 ml	Sarstedt, Nümbrecht, Germany
Syringes	20 ml	Thermo Fisher Scientific, Massachusetts, USA

5.2. Chemicals

The chemicals used in this work are listed in table 3 below.

Table 3: List of chemicals

Chemical	**Manufacturer**
2-Thiobarbituric acid (TBA)	Sigma-Aldrich, Missouri, USA
4-(2-hydroxyethyl)-1-piperazineethanesulfonic acid (Hepes)	AppliChem, Darmstadt, Germany
Acetic acid (99 - 100 %)	Roth, Karlsruhe, Germany
Advanced minimum essential medium (MEM)	Gibco, Waltham, Massachussetts, USA
Agarose	AppliChem, Darmstadt, Germany
Albumin Fraction V	Roth, Karlsruhe, Germany
Albumin, Bovine Serum, Fraction V, Fatty Acid-Poor, Endotoxin-Free (BSA-Endotoxin-Free)	Sigma-Aldrich, Missouri, USA
Albumin, Fluorescein isothiocyanate Conjugate from bovine (FITC-BSA)	Sigma Aldrich, Missouri, USA
Ammonium hydroxide	Sigma-Aldrich, Missouri, USA
Ammonium persulfate (APS)	Bio-Rad, Düsseldorf, Germany

Bisacrylamide (30 %)	Bio-Rad, Düsseldorf, Germany
Blue S'Green qPCR Kit	Biozym, Hessisch Oldendorf, Germany
Bromphenol blue	Sigma-Aldrich, Missouri, USA
Concanavalin A (Con A) Conjugates	Invitrogen, California, USA
Deoxyribonucleic acid (DNA) ladder (100 bp)	Invitrogen, California, USA
Deoxyribonucleotide triphosphates (dNTPs)	Promega, Wisconsin, USA
Diethyl pyrocarbonate (DEPC)	Sigma-Aldrich, Missouri, USA
Dimethyl sulfoxide (DMSO)	Sigma-Aldrich, Missouri, USA
Disodium hydrogen phosphate	Roth, Karlsruhe, Germany
Dulbecco's modified eagle medium (DMEM)	Gibco, Waltham, Massachussetts, USA
Ethanol	Pharmacy of the University Hospital Essen, Germany
Ethidium bromide	Sigma-Aldrich, Missouri, USA
Ethylenediaminetetraacetic acid (EDTA)	Merck, Darmstadt, Germany
Fetal bovin serum (FBS)	Biochem GmbH, Karlsruhe, Germany
Fetal calf serum (FCS)	Biochrom AG, Berlin Germany
Glutaraldehyde (GA)- Solution 25 %	AppliChem, Darmstadt, Germany
GoTaq G2 polymerase	Promega, Wisconsin, USA
GoTaq G2 polymerase	Promega, Wisconsin, USA
GoTaq reaction buffer (5X)	Promega, Wisconsin, USA
Guanidinium thiocyanate (GTC)	Roth, Karlsruhe, Germany
H_2O_2 (30 %)	Merck, Darmstadt, Germany
Hoechst	Thermo Fisher Scientific, Massachussetts, USA

LDH kit	Promega, Missouri, USA
Lipopolysaccharide (LPS)	Sigma-Aldrich, Missouri, USA
Matrigel Matrix	Thermo Fisher Scientific, Massachussetts, USA
MEM non-essential amino acids (NEAA)	Thermo Fisher Scientific, Massachussetts, USA
Methanol	Sigma-Aldrich, Missouri, USA
Milk powder	DNG Farmland
M-MLV RT reaction buffer (5X)	Promega, Wisconsin, USA
Moloney murine leukaemia virus (M-MLV) reverse transcriptase (RT)	Promega, Wisconsin, USA
Mounting medium	Agilent, California, USA
Nonidet® P40 (NP40)	AppliChem, Darmstadt, Germany
oligo-dT primers	Invitrogen, California, USA
Paraformaldehyde (PFA)	Sigma-Aldrich, Missouri, USA
Paraformaldehyde 32 % Solution	Electron Microscopy Sciences, Pennsylvania, USA
Penicillin/streptavidin (10000 U/ml)	Invitrogen, California, USA
Perfluorodecalin (PFD)	F2 Chemicals, Lancashine, UK
Potassium chloride (KCl)	Applichem, Darmstadt, Germany
Potassium hydrogen phosphate (KH_2PO_4)	Merck, Darmstadt, Germany
Proteinase inhibitor (PI)	Sigma-Aldrich, Missouri, USA
Reagent A and B (protein assay)	Bio-Rad, Düsseldorf, Germany
RPMI 1640	Gibco, Waltham, Massachussetts, USA
Sodium acetate (NaOAc)	Sigma-Aldrich, Missouri, USA
Sodium azide (Na_3N)	Applichem, Darmstadt, Germany

Sodium chloride (NaCl)	Roth, Karlsruhe, Germany
Sodium dodecyl sulfate (SDS)	Sigma-Aldrich, Missouri, USA
Sodium hydrogen phosphate	Roth, Karlsruhe, Germany
Sodium hydroxide	Roth, Karlsruhe, Germany
Sodium Pyruvate	Sigma Aldrich, Missouri, USA
Tetramethylethylenediamine (TEMED)	Sigma-Aldrich, Missouri, USA
Trichloroacetic acid (TCA)	AppliChem, Darmstadt, Germany
Trimethyl phosphate (TMP)	Sigma-Aldrich, Missouri, USA
Tris(hydroxymethyl)-aminomethane (Tris)	AppliChem, Darmstadt, Germany
Triton-X 100	Sigma-Aldrich, Taufkirchen, Germany
Trypsin (0.5 % / 10X)	Gibco, Indianapolis, USA
TUNNEL kit	Roche, Grenzacherstrasse, Switzerland
Tween 20	Sigma-Aldrich, Taufkirchen, Germany
Vectashield	Vectro Laboratories, USA
Yeast from *Saccharomyces cerevisiae*	Sigma-Aldrich, Taufkirchen, Germany
β-mercaptoethanol	Merck, Darmstadt, Germany

5.3. Cell culture media and solutions

The cell culture media and Solutions used in this work are listed in table 4 below.

Table 4: Cell culture media and solutions

Solution	**Formula**
10X Phosphate-buffered saline (PBS)	137 mM NaCl 2.7 mM KCl 10 mM $Na2HPO_4$ 2 mM $KH2PO_4$

	pH 7.4
10X Tris-buffered saline (TBS)	137 mM NaCl 20 mM Tris pH 7.6
1X Tris-buffered saline with Tween 20 (TBS-T)	1X TBS 0.05 % Tween 20
4X Lower buffer	1.5 M Tris 13.9 mM SDS pH 8.8 4X SDS buffer 200 mM Tris 8 % SDS 10 % β-mercaptoethanol 0.02 % Bromphenol 40 % Glycine
4X Upper buffer	251 mM Tris 6.9 mM SDS pH 6.8
Diethyl pyrocarbonate (DEPC) water	0.1 % DEPC in H2O
Fluorescence-activated cell sorting (FACS) buffer	1X PBS 0.1 % FCS 0.02 % Na_3N
GTC solution (4M)	4 M GTC 250 mM NaOAc 0.75 % β-mercaptoethanol in DEPC water
J774 medium	500 ml RPMI 1640 10 % FBS 1 % penicillin/ streptomycin 1 % MEM NEAA

	1 % Sodium pyruvate 1 % Hepes 1M
MEM/Hepes	500 ml advanced MEM 1 % Hepes
MEM/K10	500 ml advanced MEM 10 % FBS 1 % Glutamine 1 % PS 1 % Pyruvate 1 % Hepes 1.5 µl ß-ME
PHEM solution	60 mM PIPES, 25 mM Hepes, 10 mM EGTA, 2 mM $MgCl_2$
Protein lysis buffer	20 mM Tris 150 mM NaCl 1 % NP40 5 mM Ethylenediaminetetraacetic acid (EDTA)
THP-1/ PHM medium	10 % FBS 1 % Penicillin/streptavidin 500 ml RPMI 1640
Tris-acetate-EDTA (TAE) buffer	40 mM Tris 0.11 % Acetic acid 1 mM EDTA pH 8.0
Wash buffer (ELISA)	1X PBS 0.05 Tween 20

5.4. Software

The software used in this work are listed in table 5 below.

Table 5: List of software

Software	Manufacturer
Anton Paar RheoCompass 1.26	Anton Paar, Ostfildern-Scharnhausen. Germany
BD FACSCanto™ Clinical and BD FACSDiva™	BD Biosciences
Citavi 6	Swiss Academic Software, Rotkreuz, Switzerland
Gen5 2.06	Agilent, California, USA
Graph Pad Prism 9	Graph Pad Software, La Jolla, CA, USA
IrfanView 64	Irfan Škiljan, Austria
LASX_Office_1.4.4_26810	Leica, Wetzlar, Germany
LSM5	Zeiss, Jena, Germany
Microsoft 365	Microsoft, Redmond, WA, USA
Microtrac FLEX 11.0.0.5	Microtrac, Krefeld, Germany
Oroboros DatLab 4.3.2.4	AUT
Take3	Agilent, California, USA
ZEN blue 2.3	Zeiss, Jena, Germany

5.5. A−AOC´s synthesis

5.5.1. Using high pressure homogenization (microfluidizer)

For the synthesis of A−AOCs using high pressure homogenization, 4 ml of PFD (Fluorochem Chemicals, Derbyshire, United Kingdom) was added in 20 ml of solution of 5 w/ v % Bovine Serum Albumin, Fraction V, Fatty Acid-Poor, Endotoxin-Free (BSA, Sigma-Adrich, Sigma-Aldrich, Taufkirchen, Germany) in cell culture medium corresponding to the cell line used in

the experiment. The emulsion (PFD and 5 % BSA) was homogenized using an Ultra-Turrax ® (IKA®-Werke GmbH & Co. KG, Staufen, Germany) for 20 seconds at speed level 3 (13500 1/min). The pre-emulsified suspension was subjected to a pressure of 1380 bar (20000 PSI) using a high-pressure homogenizer (Microfluidics, Westwood, MA) and the sample was collected directly after 1 passage through the high-pressure homogenizer (Microfluidics, Westwood, MA). During this process, the cooling coil was cooled with ice so that the temperature of the suspension was kept constant during the synthesis process. Before and after synthesis, the sample was transported in an ice-filled styrofoam box. The resulting suspension contained a volume fraction of approximately 17 vol % oxygen carriers, and it was preserved in a 50 ml Falcon tube (Sarstedt AG und Co. KG, Nümbrecht, Germany) at 4°C.

5.5.2. Using ultrasound technique

For the synthesis A−AOCs using ultrasound technique, 2 ml of PFD (Fluorochem Chemicals, Derbyshire, United Kingdom) was added in 10 ml of solution of 5 w/ v % Bovine Serum Albumin, Fraction V, Fatty Acid-Poor, Endotoxin-Free (BSA, Sigma-Aldrich, Sigma-Aldrich, Taufkirchen, Germany) in cell culture medium corresponding to the experiment's cell line. The Falcon was then securely fixed in an ice bath under the ultrasound device's tip. Subsequently, the ultrasound device (UP 400S, sonotrode H3) was positioned at the interface of the albumin solution and PFD, and sonication was performed at 40 % amplitude and 8100 Ws. The synthesis was conducted under a sterile bench to generate an aseptic suspension containing a volume fraction of approximately 17 vol % oxygen carriers. In this study, the ultrasound method was chosen to produce FITC-labelled A−AOCs, as FITC BSA is highly sensitive to elevated pressure, preventing its use in the 20000 PSI microfluidizer.

5.6. Measurement of particle size distribution and particle viscosity

The particle sizes were determined by dynamic light scattering using the Stabino Nano-Flex instrument, which is equipped with a 5-mW laser with a wavelength of 780 nm. To initiate the process, a calibration was conducted by placing 1 ml of Millipore water in a 2 ml reaction tube, ensuring that the laser sensor was positioned in the lower third of the solution and preventing the formation of air bubbles. Subsequently, the same procedure was applied to the sample. Each sample was measured three times consecutively in accordance with the standard operational

settings and the software averaged the obtained values. The standard operational settings included the following: set zero time: 300 seconds, measurement duration: 300 seconds, automatic measurement repetitions: 3, refractive index (particles): 1.30, particle shape: spherical, refractive index (medium): 1.35, viscosity at 20°c: 2.053, viscosity at 25°c: 1.776. The particle sizes of A−AOCs were assessed in both J774 medium and BMDM medium, respectively, at 0 h, 4 h, and 24 h of incubation.

In addition, the viscosity of the A−AOCs was determined using the AntonPaar MCR 92 viscometer. Similar to the particle size measurements, viscosity was evaluated after 0 h, 4 h, and 24 h of incubation, as well as in both J774 medium and BMDM medium, respectively. The viscosity measurements were conducted at temperatures of 20°C and 37°C, and at shear rates ranging from 10 1/s to 600 1/s. To perform the measurements, 1.1 ml of the sample was added to the measuring plate. The experiments mentioned in this section were carried out by Nico M. Uhde during the period from November 2022 to February 2023 as part of this bachelor's thesis, which I had the privilege to supervise.

5.7. Experimental cell lines/ cell models

The cell lines used in this work are listed in table 6 below.

Table 6: List of cell lines

Cell line	**Origin**
BMDM	*Mus musculus*, mouse bone marrow
J774	*Mus musculus*, mouse ascites mouse BALB/c monocyte macrophage
L cells	*Mus musculus*, mouse Fibroblasts
THP-1	*Homo sapiens*, human peripheral blood

5.7.1. Human monocytic cell line Tohoku Hospital Pediatrics-1

The human monocytic cell line Tohoku Hospital Pediatrics-1 (THP-1) was obtained from the Fandrey working group at the Institute of Physiology of the University of Duisburg-Essen. THP-1 cell line has undergone authentication at the Leibniz Institute DSMZ German Collection of Microorganisms and Cell Cultures GmbH in Braunschweig to ensure its correct genetic identity. It was identified as human monocytic leukaemia cells; ATCC, Manassas, VA, USA. THP-1 cell line was cultured in an RPMI 1640 GlutaMAX medium (Gibco, Waltham, MA, USA) supplemented with 10 % (v/v) heat-inactivated fetal bovine serum (FBS HI; Sigma-Aldrich, Saint Louis, MO, USA), 1 % penicillin/streptomycin (PS) and 0.05 mM β- mercaptoethanol. Cells were cultured in a humidified incubator at 37°C and 5 % CO_2. The density did not exceed 800000 cells per ml to avoid spontaneous cell differentiation. For all experiments, THP-1 cells were differentiated into Primary human macrophages-like cells (PHM). For the differentiation, they were seeded in culture plates (cell density not exceeding $1x10^6$/ml) and incubated with 10 ng/ml PMA for 72 h. The PMA-containing medium was then removed, and the cells were washed with PBS and incubated for 24 h in complete media without PMA (resting period).

5.7.2. Murine J774 macrophages (J774)

J774 cell line was kindly provided by the research group of Prof. Dr. Becker Flegler at the Institute of Molecular Biology of the University of Duisburg-Essen. J774 cell line has undergone authentication at the Leibniz Institute DSMZ German Collection of Microorganisms and Cell Cultures GmbH in Braunschweig to ensure its correct genetic identity. It was identified as murine J774A.1 (ATCC TIB-67) cell line. J774 cell line was cultured in an RPMI 1640 GlutaMAX medium (Gibco, Waltham, MA, USA) supplemented with 10 % (v/v) heat-inactivated fetal bovine serum (FBS HI; Sigma-Aldrich, Saint Louis, MO, USA), 1 % penicillin/ streptomycin, 1 % MEM non-essential amino acids (NEAA, Sigma-Aldrich, Saint Louis, MO, USA), 1 % Sodium pyruvate and 1 % Hepes 1M. Cells were cultured in a humidified incubator at 37°C and 5 % CO_2. For experiments the J774 was seeded and allowed to adhere overnight.

5.7.3. Primary macrophages from mouse

5.7.3.1. Cell culture of L cells

To obtain macrophage colony-stimulating factor (M-CSF) used in the differentiation of bone marrow-derived monocytes into macrophages, L cells were used. L-cell line was obtained from the Fandrey working group at the Institute of Physiology of the University of Duisburg-Essen. L cell line (*Mus musculus*, mouse, fibroblasts; strain: C3H/An) L cell line was cultured in DEMEM (DMEM, 4.5g/l D-glucose, L-Glutamine; Gibco) supplemented with 10 % (v/v) FBS and 1 % PS. When the cells reached confluence, they were split into five 75 cm^2 flasks. After reaching confluence again, they were split into five larger 175 cm^2 flasks. To perform the splitting, the supernatant medium was aspirated, and the cells were washed with cold PBS and detached with warm trypsin. The suspended cells were mixed with fresh DMEM, and 5 ml of the cell suspension was transferred to a new flask along with 25 ml of fresh DMEM. This process of splitting was repeated every two to three days and the cell culture supernatant containing the M-CSF was collected in 50 ml falcon tubes and stored at -80°C. These tubes were thawed, and the cell culture supernatant was pooled, filtrated, and used for subsequent BMDM cell culture.

5.7.3.2. Isolation and differentiation of primary bone marrow-derived macrophages from mouse femur and tibia

Murine bone marrow-derived macrophages (BMDM) are primary murine macrophages. They were isolated from the femur and tibia of a wild-type mice (Lyz2-cre+/+ animals) from the Epas1fl x Lyz2-cre mouse line obtained from the ZTL-internal application "Isolation of Immune Cells" of the Fandrey working group at the Institute of Physiology of the University of Duisburg-Essen. The mice, which were at least 4 months old, were euthanized for scientific purposes by breaking the neck in accordance with §4 Abs. 3 (TSchG). The neck breaking procedure was carried out by a competent individual (PD Dr. Sandra Winning, M.Sc. Linda Tchuendem, or Claudia Padberg, all from the Institute of Physiology). Subsequently, cell isolation was performed by Felix Bos, who completed his specialized internship in the master's program in chemistry under my guidance from September 2022 to January 2023.

To isolate bone marrow, the mouse was euthanized by cervical dislocation, and the hind legs were separated. The skin and muscle were removed from the legs, which were then briefly placed in ethanol and subsequently stored in PBS. Under sterile conditions, the femur and tibia

were cleared of tendons and muscles, opened at both ends, and placed in a 0.5 ml tube. This tube, pierced with a 0.9 mm cannula, was inserted into a 1.5 ml tube and centrifuged at 209 g for 5 min at RT (22°C). After centrifugation, the bone marrow obtained was resuspended in 6 ml MEM/K10 medium and incubated in a culture flask overnight at 37°C, 5 % CO_2. The next day, the medium was also collected, and the suspension was centrifuged at 209 g for 5 min at RT (22°C) and the cell pellet was resuspended in 10 ml of fresh MEM/K10. The cell number was determined using a counting chamber, and the cells were seeded in 6 well plates ($5x10^5$ or $2.5x10^5$cells /2 ml) or in 96 well plates ($0.5x\ 10^4$ cells/200 µl) depending on the subsequent experiments. To promote cell differentiation, 30-50 % L-cell supernatant containing MCSF was added to the well plates. After four days, fresh MEM/K10 medium with 20 % L-cell supernatant was added, and the cells were cultured for an additional three days and were washed with MEM/Hepes on the 7^{th} day of the differentiation. The BMDM were then ready for the subsequent experiments, which included the analysis of surface markers by flow cytometry, examination of gene expression, assessment of cytokine release, monitoring of LDH release, and conducting the phagocytosis assay.

5.8. Flow cytometry

5.8.1. Determination of the surface markers CD32 and CD14 in undifferentiated THP-1 and differentiated THP-1 (PHM) by flow cytometry

CD32 is a commonly used marker for monocytes, and it is expected to be present in high concentrations on undifferentiated THP-1 cells. On the other hand, CD14 is a typical marker for macrophages and is expected to be found in high concentrations on differentiated THP-1 cells. In this study, both undifferentiated and differentiated THP-1 cells were used for the measurements. To prepare the differentiated cells, they were scraped into the medium using a sterile cell scraper and then gently pipetted up and down with a blue pipette tip to separate them. Antibodies were mixed in FACS buffer at different dilutions and combinations. The antibody mix (100 µl) was added to the cells and the tubes were incubated for 15 min at room temperature in the dark. Subsequent washing steps were performed by adding 200 µl of FACS buffer, followed by centrifugation at 2516 g for 2 min. The supernatant was discarded, and the cells were resuspended in 250 µl of FACS buffer and washed again. Finally, the cells were resuspended in 400 µl of FACS buffer and transferred to FACS tubes for measurement using the FACSCantoTM II flow cytometer. The measurement results were analyzed using the

FACSDivaTM software. To identify dead cells, a fixable viability dye (FVD) was included in the antibody mix at a dilution of 1:100. Only FVD-negative, single cells (doublets were excluded in FSC-H over FSC-A graph) were considered in the analysis. Staining in each fluorophore channel was compared to an unstained control, and the gating for positive intensities was set to ensure less than 1% positive cells in the unstained control, thus avoiding false positive staining. Flow cytometer compensation was calculated prior to the measurement using an unstained control, and single-stained samples and the results were compared with the compensation calculated by the FACSDivaTM software. The antibodies used for flow cytometry are listed in table 7 below.

Table 7: FACS antibodies/dies with conjugated fluorophore and dilution factor

Antibody/dye	Manufacturer	Fluorophore	Dilution
CD14	BioLegend, Inc. San Diego, USA	APC	1:10
CD32	BioLegend, Inc. San Diego, USA	FITC	1:10
FVD	Invitrogen, California, USA	APC-Cy7	1:100

5.8.2. Determination of the surface markers CD11b and F4/80 in BMDM

To analyze the phenotype of BMDM, flow cytometry was performed to determine the expression of surface markers CD11b and F4/80. Bone marrow cells isolated from mice, were differentiated into BMDM for 7 days as described in section 5.7.3.2. and their phenotype was analyzed using flow cytometry. Thus, bone marrow cells ($5x10^5$/well/2 ml) were cultured in media containing M-CSF for 7 days and stained using anti-CD11b-Pacific Blue and anti-F4/80-APC antibodies (BioLegend). For the analysis $1x10^6$ live cell events were recorded. The differentiated cells were scraped into the medium with a sterile cell scraper and then carefully pipetted up and down with a blue pipette tip for separation. Antibodies were mixed in FACS buffer with different dilution factors (see Table 8). 100 µl of the antibody mix were added to the cells and the tubes were incubated for 15 min at RT in the dark. All following incubation

and centrifugation steps were carried out at RT and in the dark. To wash the cells, 200 µl of FACS buffer were added and the tubes were centrifuged for 2 min at 2516 g. The supernatant was discarded. Cells were resuspended in 250 µl of FACS buffer and the washed one more time. Finally, the cells were resuspended in 400 µl FACS buffer and filled in FACS tubes for the measurement with the FACSCantoTM II flow cytometer as described in section 5.8.1.

Table 8: FACS antibodies/dies with conjugated fluorophore and dilution factor

Antibody and dye	Manufacturer	Fluorophore	Dilution
FVD	Invitrogen, California, USA	APC-Cy7	1:1 00
CD11b	BioLegend, Inc. San Diego, USA	Pacific Blue	1:200
F4/80	BioLegend, Inc. San Diego, USA	APC	1:200

5.9. Protein isolation and analysis by Lowry protein assay

To isolate and analyze proteins using the Lowry protein assay, the following steps were performed. After incubation, the cells in the 6-well culture plates were placed on ice and washed with ice-cold PBS. To detach the cells, 50 µl of lysis buffer was added, and they were scraped from the bottom of the plates and transferred to Eppendorf reaction tubes. After a 20-minute incubation on ice, the lysates were centrifuged at 2516 g and 4°C for 15 min. The supernatant was then transferred to a new reaction tube and frozen at -80°C for further analysis.

For the Lowry protein assay, 5 µl of the sample or the BSA standards (ranging from 0.1 to 25 mg/ml) was diluted with 45 µl of H_2O. Then, 20 µl of each standard or sample was added in duplicate to a 96-well plate. Next, 20 µl of reagent A and 75 µl of reagent B from Bio-Rad Laboratories were added to each well. After 5 min incubation, the absorbance at 700 nm was measured using an ELISA reader (Epoch-Reader from BioTek). The protein concentration was calculated by the program using a standard curve with known BSA concentrations ranging from 0.1 to 25 mg/ml, and the average value of the duplicate determinations was reported. The Lowry protein assay is a colorimetric method used to determine the concentration of proteins in a solution. The principle of the assay is based on the reaction between proteins and a mixture of copper ions (Cu^{2+}), and a reagent called Folin-Ciocalteau reagent. In the presence of proteins,

the copper ions form a complex with the amide bonds in the proteins, resulting in the reduction of Cu^{2+} to Cu^{1+}. This reduced copper, along with certain aromatic amino acids (such as tyrosine and tryptophan) in the proteins, reacts with the Folin-Ciocalteau reagent, causing a color change from yellow to deep blue. The intensity of the blue color is proportional to the protein concentration in the sample. By comparing the absorbance of the sample to a series of known protein standards, the concentration of the protein in the sample can be determined.

5.10. Sodium dodecyl sulfate polyacrylamide gel electrophoresis (SDS-PAGE), and Western Blot

In order to compare band intensities, an equal amount (50 µg) of protein was mixed with 4x SDS buffer and heated at 95°C for 5-10 min. The proteins were then separated based on their size using a 5 % bisacrylamide collection gel followed by a 7.5 % bisacrylamide separation gel for a total of 90 min at 120 V.

For the Western blot analysis, the separated proteins were transferred from the gel to a PVDF membrane using the Trans-Blot® Turbo™ instrument from Bio Rad. The transfer process involved stacking papers soaked in buffer, the activated membrane in ethanol, and the SDS-PAGE gel in the cassette of the instrument as instructed by the manufacturer. The transfer was carried out at 25 V and 1.3 A for 10 min. The cassette was then cooled for 20 min at 4°C before being placed back in the turbo-blot instrument for an additional 7 min using the same settings.

To block nonspecific binding sites, the membrane was incubated in a 5 % milk solution for 1 hour. It was then washed three times for 3 min each with TBS-T. The membrane was subsequently incubated overnight at 4°C in a milk solution (5 %) containing the primary antibody (Anti-actin A2103 from Sigma Aldrich at a dilution of 1:1000; ICAM-1 Polyclonal Antibody from Novus Company at a dilution of 1:500). After three washes of 5 min each with TBS-T, the membrane was incubated for 1 hour at room temperature with the secondary antibody (see table 10). Following this, the membrane was washed again five times for 5 min each with TBS-T. For detection, the membrane was incubated with 300 µl of each of the two solutions from the ECL kit from GE Amersham for 2 min, and the chemiluminescent signal was captured using the Fusion FX700. The Composition of the stacking and the separating gel for SDS-PAGE are listed in table 9 below.

Table 9 Composition of the stacking and the separating gel for SDS-PAGE

Component	Stacking gel (5 %)	Separating gel (7.5 %)
Bisacrylamide (30 %)	0.83 ml	2.5 ml
4X Upper buffer	1.25 ml	-
4X Lower buffer	-	2.5 ml
A. dest.	2.92 ml	5 ml
APS	50 µl	100 µl
TEMED	5 µl	10 µl

Table 10: List of antibodies used for Western Blot

Antibody	Manufacturer	Dilution
Anti-Actin, antibody produced in rabbit	Sigma-Aldrich	1:5000
Anti-ICAM-1/Anti-CD54 antibody produced in mouse	Novus Biologicals	1:500
Anti-rabbit-HPS	Sigma-Aldrich	1:10000
Anti-mouse IgG	Sigma-Aldrich	1:10000

5.11. Enzyme-linked immunosorbent assay (ELISA)

The ELISA was employed to quantify the release of cytokines, specifically IL-1beta and TNF-alpha in PHM and IL-1alpha and TNF-alpha in J774 and BMDM. In the case of PHM, IL-1beta and TNF-alpha level were quantified from cell-free supernatants using commercially available colorimetric kits (Human TNF-α ELISA MAXTM and Human IL-1β ELISA MAXTM, BioLegend, Inc. San Diego). For J774 and BMDM, the release of IL-1alpha and TNF-alpha was determined in cell-free supernatants via the ELISA MAX™ Deluxe Set Mouse TNF-α and ELISA MAX™ Deluxe Set Mouse IL-1α kits (BioLegend, Inc. San Diego).

THP-1 cells were seeded at $5x10^5$ cells/well/ml in a 6-well plate and differentiated through incubation with 10 ng/ml PMA for 72 h, followed by 24 h of PMA-free rest. The resulting PHM were then exposed to varying concentrations of A−AOCs 10 %, 8 %, 6 %, 4 %, 2 %) medium,

5 % BSA, or LPS (1µg/ml), and incubated at 37°C with 5 % CO2 for 24 h. LPS, a potent macrophage activator, served as a positive control, while BSA and medium acted as negative controls. J774 cells ($5x10^5$ cells/2 ml) were seeded onto a 6-well plate and allowed to adhere overnight. Subsequently, they were treated with different A−AOCs concentrations, BSA, or LPS (1µg/ml), and incubated under standard conditions for 24 h. BMDM, on the other hand, were differentiated in a 6-well plate with $5x10^5$ cells/2 ml for 7 days as described in section 5.7.3.2. On the 7th day, BMDM ($5x10^5$ cells/ml) were exposed to varying A−AOCs concentrations, 5 % BSA, or LPS (1µg/ml), and incubated at 37°C with 5 % CO_2 for 24 h. After the 24-hour incubation, cell culture supernatants were collected and centrifuged at 2516 g, 4°C for 15 min. The resulting samples were snap-frozen in liquid nitrogen and stored at -80°C until subsequent ELISA measurements. The ELISA assay was carried out as per the manufacturer's instructions. A total of 100 µl of stop solution was added, and the absorbance was read at 450 nm and 570 nm within a 15-minute timeframe. The absorbance at 570 nm was subtracted from that at 450 nm to determine the final absorbance.

5.12. RNA isolation / cDNA synthesis

RNA isolation was performed using the Qiagen RNasy Kit. THP-1 cells were seeded at $1x10^6$ cells/ml in a 6-well plate and differentiated through incubation with 10 ng/ml PMA for 72 h, followed by 24 h of PMA-free rest. The resulting PHM were then exposed to varying concentrations of A−AOCs (10 %, 8 %, 6 %, 4 %, 2 %), medium, 5 % BSA, or LPS (1µg/ml), and incubated at 37°C with 5 % CO_2 for 24 h. J774 cells ($5x10^5$ cells/2 ml) were seeded onto a 6-well plate and allowed to adhere overnight. Subsequently, they were treated with different A−AOCs concentrations, BSA, or LPS (1µg/ml), and incubated under standard conditions for 24 h. BMDM, on the other hand, were differentiated in a 6-well plate with $5x10^5$ cells/2 ml for 7 days as described in section 5.7.3.2. On the 7th day, BMDM ($5x10^5$ cells/ml) were exposed to varying A−AOCs concentrations, 5 % BSA, or LPS (1µg/ml), and incubated at 37°C with 5 % CO2 for 24 h. After the 24-hour incubation, the samples for RNA isolation were stored at -20°C in a 4M GTC solution. Upon thawing, the samples were processed following the manufacturer's protocol. The concentration and purity of the RNA were measured using the Epoch™ Microplate Spectrophotometer and a Take3 plate. For short-term storage, RNA was kept at +4°C, while for longer-term storage, it was stored at -20°C.

To synthesize cDNA, 1 µg of RNA was mixed with deionized water to a total volume of 9.5 µl. The diluted RNA was then mixed with 2.5 µl of oligo-dT primers and heated to 68°C for 10 min. After a further 10 min on ice, 13 µl of the reaction mix (see Table 11) was added, and the cDNA synthesis reaction was initiated according to the specified parameters (see Table 12). A negative control, using deionized water instead of an RNA sample, was included to ensure the purity of the components. The newly synthesized cDNA was verified by performing a standard polymerase chain reaction targeting the housekeeping gene hypoxanthine phosphoribosyltransferase 1 (HPRT1).

Table 11: Reaction mix for cDNA synthesis

Reaction mix component	**Volume per sample (µl)**
5X M-MLV RT buffer	5
dNTPs	5
H_2O	2.5
Reverse transcriptase	0.5

Table 12: Protocol of cDNA synthesis in the mastercycler

Temperature	**Time (min)**
45°C	90
52°C	30
95°C	15

5.13. Polymerase chain reaction and quantitative PCR

5.13.1. Polymerase chain reaction (PCR)

The polymerase chain reaction (PCR) is a technique used to detect gene expression in a tissue or cell line. It involves amplifying a specific region of the gene of interest using DNA primers and a DNA polymerase. The amplified product is then visualized on an agarose gel with ethidium bromide. In this study, cDNA synthesized from PHM, BMDM or J774 cells was analyzed using PCR to determine the mRNA expression levels of certain genes. For the PCR

reaction, 0.5 µl of cDNA template was mixed with a reaction mix containing the polymerase, its reaction buffer, dNTPs and gene-specific primers (see Table 13). A negative control without DNA template was included to ensure the purity of the water and primers. The cDNA templates were mixed with the reaction mix and the PCR program was started in the mastercycler. The program consisted of an initial denaturation step, followed by 35 cycles of denaturation, annealing, and elongation. A final extension step completed the reaction. The annealing temperature was set at 60°C for all reactions in this study. The synthesized PCR products were visualized on a 2 % agarose gel containing 0.08 % ethidium bromide. A 100 bp DNA ladder was loaded in the first slot of the gel to serve as a reference for analyzing the PCR products. The PCR products from the samples were loaded in separate slots on the gel. After 45 min of electrophoresis at 100 V, the gel was photographed under ultraviolet (UV) light. Qualitative PCR reactions were performed to test the specificity of the primers or to confirm the success of cDNA synthesis using primers for the housekeeping gene HPRT1.

Table 13: Reaction mix for a PCR per sample

Component	**Volume per sample (µl)**
5X GoTaq reaction buffer	5
dNTPs	2
Primer 5’ / 3’ (200 µM)	0.5
GoTaq G2 polymerase	0.1
H_2O	17

Table 14: The PCR program

Phase	Temperature	Duration
Initial phase	96°C	3 min
Denaturation	96°C	1 min
Annealing	60°C	1 min
Elongation	72°C	1 min
Terminal synthesis	72°C	10 min

5.13.2. Quantitative PCR (qPCR)

To quantify the expression of a gene of interest in an mRNA sample, a quantitative PCR (qPCR) was performed using the corresponding cDNA and gene-specific primers. For this analysis, 0.5 µl of cDNA served as the template and was combined with the necessary reaction components (see table 15). Subsequently, 9.5 µl of the reaction mixture plus 0.5 µl of cDNA were pipetted into a well of a 96-well plate. To obtain duplicate determinations, an additional 9.5 µl of the reaction mixture plus 0.5 µl of cDNA were added to the subsequent well. The first two wells were reserved for a negative control without the DNA template, where 9.5 µl of the reaction mixture plus 0.5 µl of dd water were pipetted into those wells. The 96-well plate was then placed into the iCycler iQ5TM, and the PCR program was initiated according to the parameters specified in table 16. All qPCR runs were conducted at an annealing temperature of 60°C for 40 cycles of denaturation, annealing, and elongation. Periodically, to ensure primer purity and exclude the presence of side products, a melting curve of the PCR product was measured for each primer pair. The iCycler iQ5TM detected the amount of PCR product through fluorescence emitted by the SYBR Green dye and reported the Cycle of Threshold (CT) with an automatically calculated threshold. To determine fold change values in comparison to untreated samples, the CT value was normalized to the housekeeping gene HPRT1 using the ΔΔCT method [97]. The primer sequences used for PCRs and quantitative PCRs are listed in tables 17 and 18.

Table 15: Reaction mixture for qPCR

Component	Volume per sample (µl)
Blue S'Green qPCR Kit	12.5
Primer 5' / 3' (200 µM)	0.5
H2O	11

Table 16: The qPCR program

Phase	Temperature	Duration
Initial phase	95°C	10 min
Denaturation	95°C	15 s
Annealing and elongation	60°C	90 s

Table 17: Sequence of human primers used for PCR and RT-qPCR

Designation	Oligonucleotide		Reference sequence ID
HPRT1	Forward primer	CCTGGCGTCGTGATTAGTGA	NM_000194.3
	Reverse Primer	CGAGCAAGACGTTCAGTCCT	
ICAM1	Forward Primer	TTGGGCATAGAGACCCCGTT	NM_000201.3
	Reverse Primer	GCACATTGCTCAGTTCATACACC	
VCAM1	Forward Primer	GATTCTGTGCCCACAGTAAGGC	NM_001078.4
	Reverse Primer	TGGTCACAGAGCCACCTTCTTG	
TNFA	Forward Primer	GAGGCCAAGCCCTGGTATG	NM_000594.4
	Reverse Primer	CGGGCCGATTGATCTCAGC	
CXCL8	Forward Primer	ACTGAGAGTGATTGAGAGTGGAC	NM_000584.4
	Reverse Primer	AACCCTCTGCACCCAGTTTTC	

CD86	Forward Primer	CTGCTCATCTATACACGGTTACC	NM_175862.4
	Reverse Primer	GGAAACGTCGTACAGTTCTGTG	
CCR2	Forward Primer	CAGGTGACAGAGACTCTTGGGA	NM_001123041.3
	Reverse Primer	GGCAATCCTACAGCCAAGAGCT	
IL1B	Forward Primer	CCACAGACCTTCCAGGAGAATG	NM_000576.3
	Reverse Primer	GTGCAGTTCAGTGATCGTACAGG	
GLUT1	Forward Primer	TTGCAGGCTTCTCCAACTGGAC	NM_006516.4
	Reverse Primer	CAGAACCAGGAGCACAGTGAAG	

Table 18: Sequence of murine primers used for PCR and RT-qPCR

Designation	**Oligonucleotide**		**Reference sequence ID**
Hprt1	Forward Primer	CTGGTGAAAAGGACCTCTCGAAG	NM_013556.2
	Reverse Primer	CCAGTTTCACTAATGACACAAACG	
Icam1	Forward Primer	AAACCAGACCCTGGAACTGCAC	NM_010493.3
	Reverse Primer	GCCTGGCATTTCAGAGTCTGCT	
Vcam1	Forward Primer	GCTATGAGGATGGAAGACTCTGG	NM_011693.3
	Reverse Primer	ACTTGTGCAGCCACCTGAGATC	
Tnfalpha	Forward Primer	GGTGCCTATGTCTCAGCCTCTT	NM_001278601.1
	Reverse Primer	GCCATAGAACTGATGAGAGGGAG	
Cd86	Forward Primer	GACCGTTGTGTGTGTTCTGG	NM-019388.3
	Reverse Primer	GATGAGCAGCATCACAAGGA	
Ccr2	Forward Primer	GGAAGAGCAGGTCAGAGATGG	NM_009915.2
	Reverse Primer	TACGATGATGGTGAGCCTTGT	
Il1alpha	Forward Primer	GCACCTTACACCTACCAGAGT	NM_010554.4

	Reverse Primer	AAACTTCTGCCTGACGAGCTT	
Glut1	Forward Primer	CAGTTCGGCTATAACACTGGTG	NM_011400.3
	Reverse Primer	GCCCCCGACAGAGAAGATG	

5.14. Uptake of A−AOCs

5.14.1. Uptake of A−AOCs detected by confocal laser scanning microscopy

To assess the uptake of A−AOCs by macrophages, an assay was conducted using differentiated THP-1 cells (PHM), J774 and BMDM and 4 % of FITC A−AOCs. Initially, a coverslip was placed in each well of a 6-well plate, and then 1 ml of a 0.2 % gelatine solution was added to each well. The plate was incubated at 37°C for 2 h. Afterwards, the gelatine solution was removed, and the cell suspension was added to the coverslips and allowed to adhere or to differentiate. THP-1 was allowed to differentiate as described in section 5.7.1. J774 ($5x10^5$ cells/ml) was added to the coverslips and allowed to adhere overnight. BMDM ($2.5x\ 10^5$ cells/2 ml) was differentiated in MEM/K10 medium containing M-CSF as described in section 5.7.3.2. On the experimental day, concanavalin A (Con A, Invitrogen, USA) was centrifuged at 10062 g for 10 min to obtain a pellet. A solution of 100 µg/ml Con A was prepared using cold serum-free medium and 1 ml of this solution was added to the wells. After 30 min of incubation, the solution was aspirated. The cells were washed three times with warm PBS (for PHM and J774) or with warm MEM/Hepes medium (for BMDM). Subsequently, 1 ml of a 4 % FITC A−AOCs solution was added to each well, and two wells were incubated for 30 min and 120 min, respectively. At the end of the incubation period, cold PBS was used to wash the cells again, and then 1 ml of a 2 % PFA solution was added to each well to fix the cells for 30 min at room temperature. The cells were washed three more times with PBS, and the coverslips were mounted on slides using Vectashield Mounting Medium to preserve fluorescence. 10-20 images per well were captured using a confocal microscope at wavelengths of 488 nm and 543 nm. The uptake of A−AOCs in J774 and BMDM was investigated by Nico M. Uhde.

5.14.2. Uptake of A−AOCs detected by electron microscopy

This experiment was conducted to confirm the uptake of A−AOCs by PHM, J774 and BMDM and for a more detailed analysis. The phagocytosis assay was performed on the three target cell lines. All target cell lines were seeded in Ibidi dishes ($2.5\text{-}5x10^5$ cells/ per dish), to be

compatible with TEM imaging. Samples were prepared as described in section 5.21.1, with adaptions of the fixation procedure. For the fixation, the cells were covered with 2 ml of the respective medium, to which 2 ml of double fixans were added, and then left for 15 min at room temperature. The wells were subsequently aspirated, and 1 ml of 1x fixans was added to each well for a 3-hour fixation period. After the fixation process, the samples were stored in 1% FA in a 0.1M PHEM solution. The Samples were transported to the imaging centre of the university hospital Essen for the further processing procedure: after incubation with 1% OsO4 in PHEM buffer and contrastation with 1% uranyl acetate 55 µm-ultrathin sections were cut from Epon embedded samples. Sections were mounted on 200 MESH copper grids and micrographed by a TemCam-F416 on a Jeol JEM 1400 Plus TEM. Electron microscope images were captured by PD Dr. Holger Jastrow.

5.14.3. Correlative light and electron microscopy (CLEM)

To achieve a precise identification of our A−AOCs within the macrophages, we conducted a CLEM using J774 cells. J774 cells ($5x10^5$ cells/dish) were plated on Ibidi dishes and allowed to adhere overnight. On the following day, the cells were treated with TRITC-Concanavalin A (100 µg/ml) for 30 min to enable labelling. Subsequently, the cells were incubated with 4 % FITC-labelled A−AOCs (1 mg/ml) for 120 min. After the incubation period of 120 min, the cells underwent three washes with warm PBS, followed by the addition of fresh warm medium. Subsequently, the dish containing the cells was transported to the imaging centre of the University Hospital Essen for further processing. This involved visualizing the cells using both regular light and a 580 nm wavelength under a fluorescent microscope. Additionally, the cells underwent examination using transmission electron microscopy (TEM). The resulting fluorescent and TEM images were then correlated to analyse the localization of the green fluorescence, which is indicative of FITC-labelled A−AOCs, in both the Light Microscopy and Electron Microscopy images of the same cells. Dr. Mike Hasenberg and PD Dr. Holger Jastrow generated the CLEM images.

5.15. Cell viability assay (LDH assay, TUNEL assay)

5.15.1. LDH assay

For the cell viability assay, the LDH (lactate dehydrogenase) activity was measured in cell-free supernatants using a commercially available colorimetric kit (CytoTox 96® Non-Radioactive Cytotoxicity Assay, Promega Corporation (USA). To determine the influence of A−AOCs on cell viability, the LDH assay was conducted with PHM, J774 and BMDM after 4h and 24 h of incubation with A−AOCs, 5 % BSA, LPS, medium. The positive control was obtained by adding the lysis buffer (included in the LDH assay Kit) into the untreated cells (medium) at the dilution factor of 1:10, 45 min before the end of the exposure time.

For the 4 h LDH assay, PHM ($1x10^4$ cells/well/100 µl), J774 ($0.5x10^4$ cells/well/100 µl) and BMDM ($0.5x10^4$ cells/well/100 µl) were seeded in 96 well plates and were treated with different concentrations of A−AOCs (17%: undiluted A−AOCs, 10 %, 8 %, 6 %, 4 %, 2 %) medium, 5 % of BSA or LPS (1µg/ml), respectively, and incubated at 37°C with 5 % CO_2 for 4 h. As a positive control for maximum release, cells were incubated with culture medium, and 45 min before adding CytoTox 96 reagent, 10 µl of 10x lysis solution was added to the positive control wells containing. A total of 50 µl of the cell supernatant was mixed with an equal volume of reconstituted substrate mix. The plate was covered with foil and incubated at room temperature for 30 min, protected from light. Following this, 50 µl of stop solution was added, and the absorbance was read at 490 nm. Nico Uhde conducted the LDH assay in J774, and the obtained results were utilized in his bachelor's thesis.

$$\text{Percent cytotoxicity} = 100 \times \frac{\text{Experimental LDH Release (OD490)}}{\text{Maximum LDH Release (OD490)}}$$

For the 24 h LDH assay, PHM ($5x10^5$ cells/well/ml), J774 ($5x10^5$ cells/well/2 ml) and BMDM ($5x10^5$ cells/well/ml) were seeded in 6 well plates and were treated with LPS (1 µg/ml), medium, 5% of BSA or 10 −2 % of A−AOCs for 24 h. This assay was carried out using an identical cell count per well and the same amount of medium as employed in the ELISA assay to ensure better comparability of the results between both assays. After the 24-hour incubation, cell culture supernatants were collected and centrifuged at 2516 g, 4°C for 15 min. The resultant samples were promptly frozen in liquid nitrogen and stored at -80°C until further LDH measurements were conducted by Eva Hillen at the Institute of Physiological Chemistry.

5.15.2. TUNEL assay

Using the TUNEL assay, dead cells were labeled in PHM. For the TUNEL staining, PHM ($1x10^4$ cells/ml) were then treated with different concentrations of A−AOCs (17 %: undiluted A−AOCs, 10 %, 8 %, 6 %, 4 %, 2 %), medium, 5 % of BSA or LPS (1µg/ml), respectively, and incubated at 37°C with 5 % CO_2 for 4 h. After washing the cells three times with PBS, the cells were fixed with 4 % PFA in PBS (200 µl/well) for 1 hour at room temperature. The cells were then rinsed once with PBS and stored at 4°C overnight. On the second day, for the positive control, a solution of DNase I recombinant was prepared by mixing 87 µl deionized water, 10 µl DNAse buffer solution, and 3 µl DNA recombinant (Roche) in a ratio of 3:100 (3000 Units). The 100 µl DNAse solution was added to the fixed and permeabilized cells and incubated for 30 min at 37°C. For the negative control, 50 µl of the label solution was added to the fixed and permeabilized cells, and 100 µl of the label solution was removed (2 negative controls) per tube. The TUNEL reaction mixture was prepared by adding 50 µl of enzyme solution to the remaining 450 µl of the label solution. Then, 50 µl of the TUNEL reaction mixture was added to the sample, including the positive control. The plate was covered with parafilm and incubated in a humidified atmosphere for 60 min at 37°C in the dark. After rinsing three times with PBS, the cells were stained with Hoechst solution (1.5 µM) by adding 200 µl of the solution to each sample and incubating for 30 min at room temperature in the dark. The cells were then rinsed three times with PBS. The analysis was performed using a fluorescence microscope with the green filter for TUNEL staining and the blue filter for Hoechst staining. The images were merged using ImageJ software. In general, a solution of DNase I recombinant dissolved in Tris-HCl buffer at pH 7.4 was used for the positive control, and the cells were incubated for 30 min at 37°C.

5.16. Cell migration assay

For the migration assay, a 24-well plate from Sarstedt was used. Transwell inserts with pore sizes of 8 µm ($1\text{-}10^5$ pores/cm^2) were purchased from Millipore. Matrigel was thawed and liquefied on ice, and then 50 µl of Matrigel was added to each well of a 24-well transwell insert and allowed to solidify overnight at room temperature to form a thin gel layer. The Matrigel was diluted with serum-free cooled medium at a ratio of 1:3. All work was performed under sterile conditions and on ice to prevent premature polymerization of the Matrigel. Pre-cooled pipette tips were used as well. THP-1 cells were differentiated for 72 h, followed by a resting

period of 24 h. The resulted PHM (1x 10^6 cells/ml), incubated with lipopolysaccharides (LPS, 1 µg/ml), medium, 5 % bovine serum albumin (BSA), 10 % of A−AOCs or 4 % of A−AOCs for 18h. PHM were detached from the cell culture plate using a cell scraper. The cells were pelleted by centrifugation in a 15 ml conical tube, the supernatant was aspirated, and the cells were resuspended in culture media. A total of 150 µl of the PHM cell suspension (1x10^6 cells/ml) was plated on top of the filter membrane in a transwell insert, and 600 µl of cell culture medium was added to each well containing the insert to facilitate contact between both areas and simulate invasion through the extracellular matrix. PHM were exposed to a Matrigel for 90 min at 37 °C, 21 % O_2 and 5 % CO_2 to allow the cells to migrate. Afterwards, the inserts were washed three times with PBS to remove non-migrated cells. The cells were fixed with 400 µl of 2 % PFA solution at room temperature for 30 min, followed by three washes with PBS. Subsequently, the cells were stained with Hoechst dye (Hoechst 33342, 1 µM) for 30 min at room temperature, and then washed three times with PBS. Evaluation under the microscope was performed the next day. Until then, the inserts were coated with PBS to prevent the matrix from drying out and were stored at 4°C.

5.17. Measurement of oxygen consumption in macrophages

To assess the influence of A−AOCs on macrophage oxygen consumption, we employed a respirometer (Oxygraph-2k, Oroboros Instruments, Innsbruck, Austria) to measure oxygen consumption in PHM and J774 (cell suspension) over a 10-min period. Prior to respirometer measurements, PHM and J774 were incubated with medium, BSA, LPS, and A−AOCs at a concentration of 4%, respectively, for 24 h. After incubation, cells were detached using a cell scraper, collected in 15 ml conical centrifuge tubes, and counted using a counting chamber. Cell viability (live and dead cells) was determined using the trypan blue dye exclusion test. The cells were then adjusted to a concentration of 1.10^6 living cells/ml in fresh warm medium and maintained at 37°C during the measurements with the Oxygraph-2k. The Oxygraph-2k measures the changes in oxygen concentration within a closed chamber. It consists of a respirometer chamber equipped with Clark-type oxygen electrodes, which are sensitive to oxygen levels. The electrodes are connected to an oxygen sensor that measures the oxygen tension in the chamber. Prior to each set of measurements, a background calibration was performed. For this purpose, the chambers of the Oxygraph-2k were filled with a total volume of 2 ml of water and tempered to 37°C. The water was stirred and incubated at atmospheric

pressure, until a constant oxygen content was reached. Based on this maximum value of oxygen content and the theoretical oxygen capacity of water under the indicated conditions (209 nmol/ml), the correction factor F (O2) was calculated.

$$F(O_2)\ [mmol] = \frac{\text{max. } O_2 \text{ content}_{H2O} \text{ (adjusted)}}{\text{max. } O_2 \text{ content}_{H2O} \text{ (actual)}}$$

The chambers of the Oxygraph-2k were filled with phosphate buffer (50 mM) and hermetically sealed. Oxygen dissolved in buffer was removed by adding 96 µl of yeast (83 mg/ml in phosphate buffer) and 50 µl glucose (1 M in phosphate buffer). Subsequently, 60 µl of potassium cyanide (100 mM in phosphate buffer) was added to prevent aerobic metabolism of the yeast in the processing experiment. Subsequently to the calibration, 2.2 ml of cell suspension (1.10^6 cells/ ml) was pipetted into the chamber of the Oxygraph-2k and hermetically sealed. The oxygen concentration in the chamber was measured for 10 min and the oxygen consumption in the cell was calculated at a time point (tx).

$$\text{oxygen consumption}_{tx} = \frac{\text{oxygen consumption}_{tx} - \text{oxygen consumption}_{t0}}{\text{oxygen consumption}_{tx}}$$

5.18. Malondialdehyde (MDA) detection

THP-1 cells were seeded at a density of $5x10^5$ cells per well in a 6-well plate and subjected to differentiation. The differentiation process involved incubation with 10 ng/ml PMA for 72 h, followed by a subsequent 24-hour resting period in PMA-free medium. The resulting PHM were exposed to varying concentrations of A−AOCs (10 %, 8 %, 6 %, 4 %, 2 %) medium, 5 % BSA, or LPS (1µg/ml), respectively, and then incubated at 37°C with 5 % CO_2 for a duration of 24 h. After 24 h incubation, cell culture supernatant was collected and centrifuged at 2516 g, 4°C for 15 min. The samples were then snap frozen in liquid nitrogen and stored at -80°C for later use. The MDA detection was performed using the spectrophotometric thiobarbituric acid reactive substances (TBARS) test. For this purpose, 500 µl of the sample was combined with

250 µl of 30 % trichloroacetic acid (AppliChem, Darmstadt, Germany) and then centrifuged at 10062 g at room temperature for 5 min. Subsequently, 500 µl of the resulting supernatant was transferred to a fresh tube and mixed with 250 µl of 1 % thiobarbituric acid (Sigma Aldrich, Darmstadt, Germany). The mixture was incubated for 10 min at 99°C using a sealed vessel in an Eppendorf® ThermoMixer® (Eppendorf, Hamburg, Germany) and its absorbance was read at 532 nm in a 96-well plate using a photometer (Gen5 2.06, Agilent, California, USA).

5.19. Statistical analysis

The statistical analysis was conducted using PRISM® software (GraphPad), version 9. For pairwise comparisons of two datasets, the student's t-test was employed, while analyses involving more than two datasets utilized one-way ANOVA followed by Dunnett's Multiple Comparison. The significance level, set at $p \leq 0.05$, was illustrated on the figures in the results section using asterisks: *$p < 0.05$, **$p < 0.01$, *** $p < 0.001$, and ****$p < 0.0001$.

6. Results

6.1. Differentiation of THP-1 cells into primary human macrophage-like cells

Initially, under microscopic examination, the undifferentiated THP-1 cells exhibited a round morphology, suspended within the culture medium (figure 5 A). Following the differentiation process with 10 ng/ml PMA, the differentiated THP-1 cells transitioned into an adherent state. This was characterized by elongated protrusions on some cells and an expansion in cytoplasmic volume (figure 5 B). Subsequently, the result of flow cytometry assessing monocytic and macrophagic surface markers (figure 5 C), showed that 97.37 % of undifferentiated THP-1 cells demonstrated positivity for CD32, whereas 77.77 % of differentiated THP-1 cells exhibited CD32 positivity. In contrast, 83.62 % of differentiated THP-1 cells expressed CD14, a distinctive surface marker of macrophages. In comparison, only 10.45 % of undifferentiated THP-1 cells displayed CD14 expression. The statistical analysis using Two tailed, unpaired t test indicated a significant difference in CD32 and CD14 expression between undifferentiated and differentiated THP-1 cells. Interestingly, CD32 was prominently expressed in undifferentiated THP-1 cells, while CD14 showed a significantly higher expression in the differentiated THP-1 cells, also referred to as PHM or M0 macrophages in this study. To avoid artificial gene upregulation as well as to detect responses of PHM to weak stimuli [98], all further experiments were performed with only 10 ng/ml PMA.

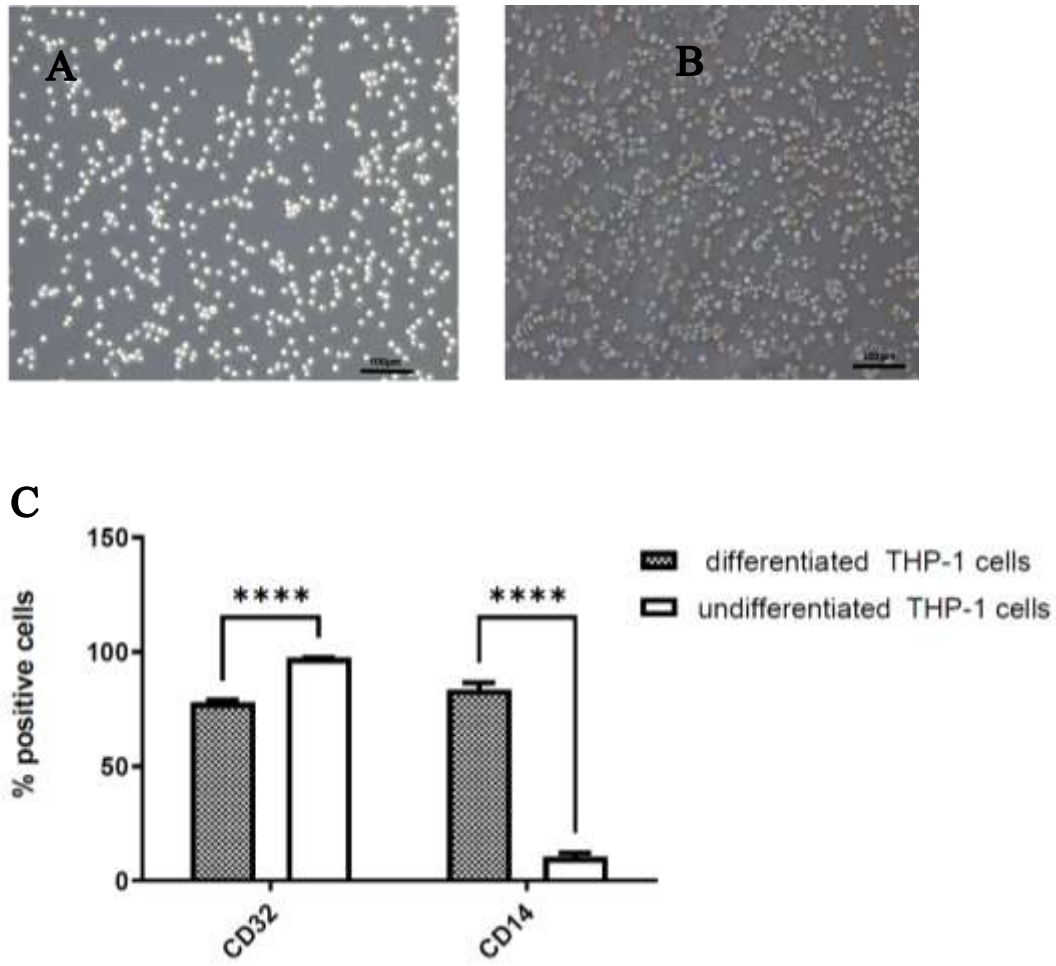

Figure 5: Characterization and identity verification of THP-1 and PHM

THP-1 cells before differentiation (A) and after differentiation with 10 ng/ml of PMA (B: differentiated THP-1 cells = PHM or M0 macrophages). Magnification: 10x; Bars, 100 µm; representative images from 4 fields of view (FOV) for each condition. CD32 and CD14 expression in undifferentiated and differentiated THP-1 cells was analysed by FACS using FITC-labelled anti-human CD32 monoclonal antibody and APC-labelled anti-human CD14 monoclonal antibody (C). Bar plots indicate percentages of positive cells. Results are expressed as mean percentages of positive cells ± SEM. Asterisks represent a significant difference; ****p< 0.0001; Two tailed, unpaired t test; n= 12

6.2. Differentiation of bone marrow derived monocytes into BMDM

To generate BMDM, bone marrow cells were directly isolated from mice's femur and tibia and then subjected to differentiation using MEM/K10 supplemented with L-cell supernatant containing M-CSF. This differentiation process involved culturing the isolated cells in MEM/K10 containing 30-50 % L-cell supernatant for a duration of 7 days. The resulting macrophages, designated as BMDM, were subjected to both visual examination under a microscope and molecular analysis through flow cytometry. Initially, when observed under a

microscope, the isolated bone marrow cells revealed a round morphology while suspended in the culture medium (figure 6 A). However, after undergoing the differentiation process in the presence of M-CSF, the resulting BMDM exhibited adhesion, along with the development of elongated projections and an increase in their cytoplasmic volume (figure 6 B). Subsequent flow cytometry results that assessed macrophage surface markers (figure 6 C) indicated that both CD11b and F4/80 were expressed in BMDM at rates of 84.48 % for CD11b and 90.59 % for F4/80, respectively. Statistical analysis, utilizing an unpaired t test, demonstrated that F4/80 was significantly more prominently expressed compared to CD11b.

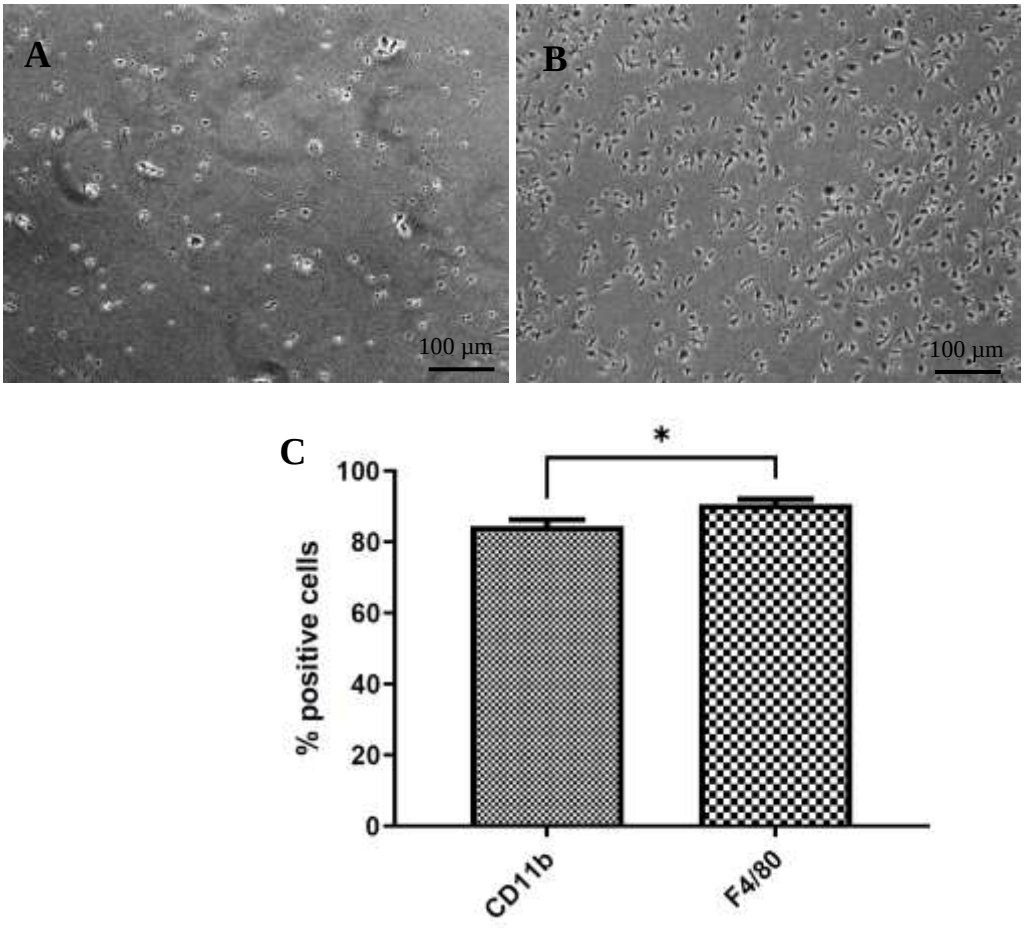

Figure 6: Characterization and identity verification of BMDM

BMDM were cultured in MEM/K10 without M-CSF (A) or in MEM/K10 containing M-CSF (B) for 7 days. Magnification: 10x; Bars, 100 µm; representative images from 4 FOV for each condition. Subsequently, CD11b and F4/80 expression in BMDM was analysed by FACS using Pacific, Blue-labelled anti-mouse CD11b monoclonal antibody and APC-labelled anti-mouse F4/80 monoclonal antibody (C). Bar plots indicate percentages of positive cells; Results are expressed as mean percentages of positive cells ± SEM; *p< 0.05; Unpaired t test; n =12.

6.3. The influence A−AOCs on cell extravasation and cell migration in PHM

6.3.1. Western Blot analysis of ICAM-1 Expression

The impact of A−AOCs on the expression of ICAM-1, which is linked to pro-inflammatory cytokine-induced conditions, was investigated using western blot analysis (see figures 7 A and 10 B). The results of the analysis exhibited a tendency towards increased ICAM-1 expression in PHM treated with LPS with a ratio ICAM-1/ß-actin of 2.73 compared to medium with a ratio ICAM-1/ß-actin of 1.68. In contrast, ICAM-1 expression significantly decreased in PHM cells treated with 10−2 % of A−AOCs which showed a ratio ICAM-1/ß-actin of 0.13, 0.16, 0.16, 0.06 for A−AOCs at the concentrations of 10%, 8 %, 4 % and 2 % respectively compared to the control group (medium). Remarkably, the expression of ICAM-1 in the control group as well as in cells treated with BSA was nearly identical with ratios ICAM-1/ß-actin of 1.68 and 1.67 respectively.

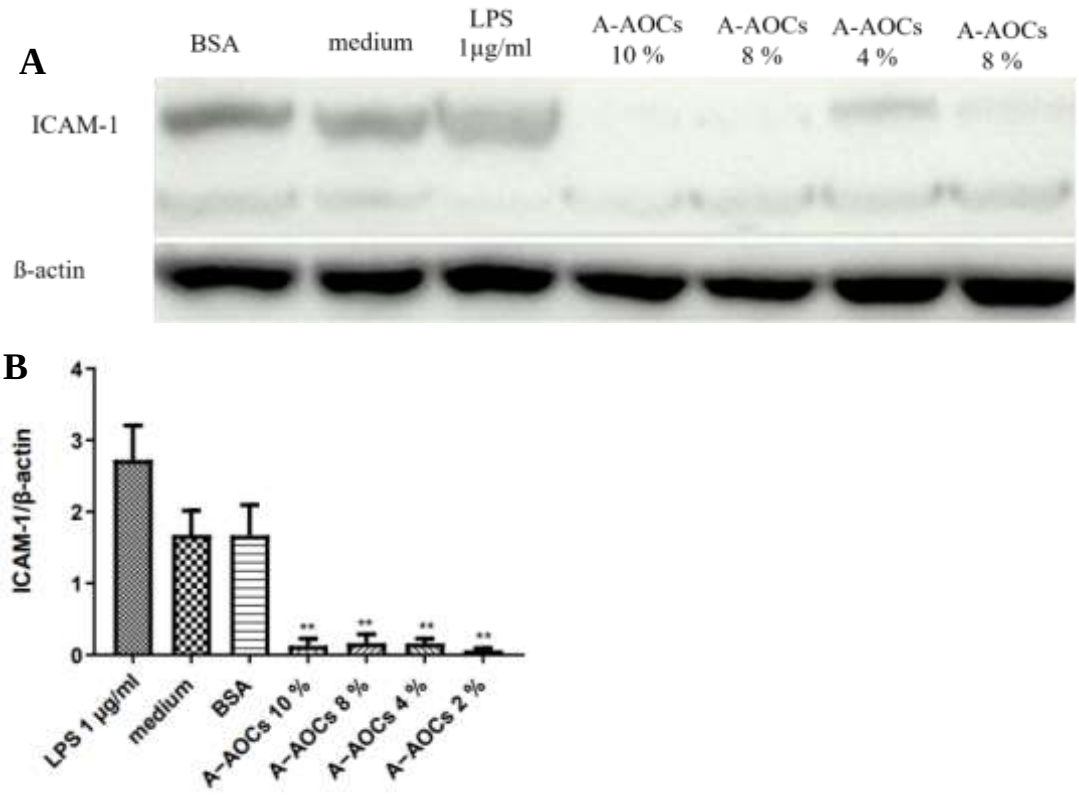

Figure 7: Western blot analysis of ICAM-1 protein expression

PHM, treated with 5 % bovine serum albumin (BSA), medium, lipopolysaccharides (LPS, 1 µg/ml) a potent activator of macrophages or 10−2 % of A−AOCs, respectively, were exposed to 21 % O_2 (normoxia) for 24 h. (A): Western blot of ICAM-1 with ß-actin as loading control. (B): bar plots represent the values of ICAM-1 normalized to ß-actin. Results are expressed as mean values of ICAM-1 normalized to ß-actin ± SEM. **p< 0.01; one-way ANOVA; n = 5.

6.3.2. Migration assay

The influence of A−AOCs on cell migration was investigated with a migration assay using matrigel coated inserts (see figure 11). The results of migration assay showed a tendency of decreasing number of migrated cells in PHM treated with 10 % with 172.3 cells (see figures 8 D and F) as well as 4 % with 180.0 cells (see figure 8 E and F) of A−AOCs respectively. Cells treated with LPS (1 µg/ml) showed a similar migration rate with 178.6 migrated cells. Notably, the number of migrated cells significantly decreases in PHM treated with BSA with 170.8 cells (see figures 8 C and F) as compared to medium with 187.7 cells (see figures 8 B and F).

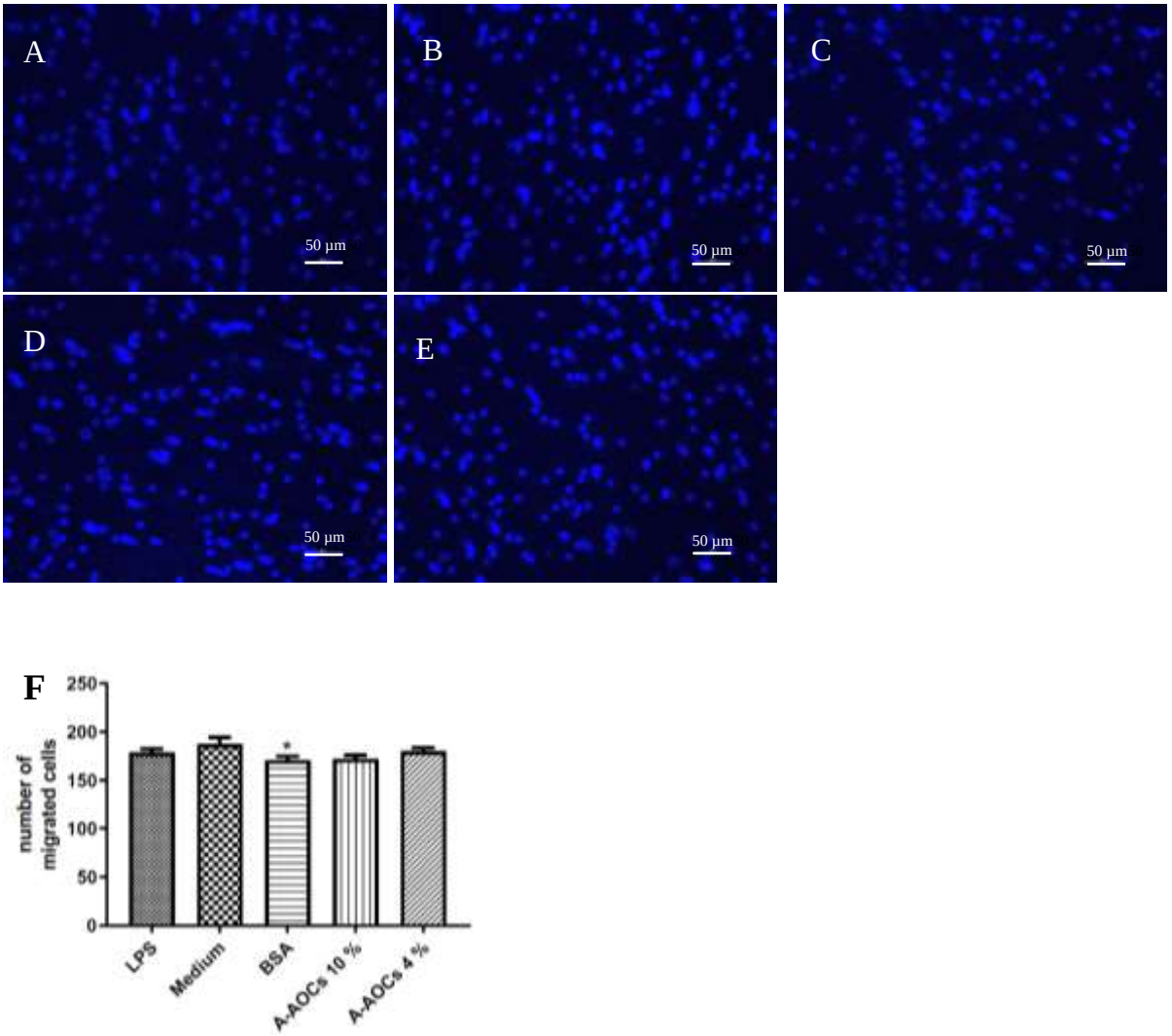

Figure 8: Number of migrated cells in PHM

PHM (1x 10^6 cells/ml), incubated with lipopolysaccharides (LPS, 1 µg/ml; A), medium (B) 5 % bovine serum albumin: BSA (C), 10 of A−AOCs (D) or 4 % of A−AOCs (E) for 18h, were exposed to a Matrigel for 90 min. (A), (B), (C), (D) and (E) are representative images of 20 FOV for each condition. Magnification: 20x; Bars, 50 µm. Bar plots represent the number migrated cells (F). Results are expressed as mean number of migrated cells ± SEM. Data were analyzed by one-way ANOVA followed by Dunnett's Multiple Comparison against medium; *p< 0.05; n=3.

6.4. Cell viability measured by LDH assay

6.4.1. Cell viability in PHM measured by LDH assay

The results of LDH assay (see figure 9 A) show that A−AOCs did significantly not affect cell viability, even at the highest tested concentration of 17%, following a 4-hour incubation period. The percent cytotoxicities for PHM treated with A−AOCs at concentrations of 17 %, 10 %, 8 %, 6 %, 4 %, and 2 % were 22.56 %, 22.07 %, 20.95 %, 22.25 %, 16.97 % and 18.17 % respectively. Notably, significant toxicity was only observed in PHM treated with LPS (1 µg/ml) and the positive control, with percent cytotoxicities of 24.68 % and 100 %, respectively, when compared to the medium. PHM in the medium and BSA exhibited similar percent cytotoxicities of 17.48 % and 14.25 %, respectively. Subsequently, as shown in figure 9 B, the percent cytotoxicity remained even lower in PHM treated with A−AOCs at concentrations of 10 %, 8 %, 6 %, 4 %, and 2 %, with percent cytotoxicities ranging from 2.13 % to 0.02 %, -0.27 %, 15.44 %, and 7.39 %, respectively, after 24 h of exposure, when compared to untreated cells (medium) with a percent cytotoxicity of 18.73%. Similar to the 4-hour results, significant toxicity was only observed in PHM exposed to LPS and the positive control, with percent toxicities of 52.92 % and 100 %, respectively, after 24 h, compared to the medium. Cell viability in the medium and BSA remained nearly identical, with percent cytotoxicities of 18.73 % and 17.94 %, respectively.

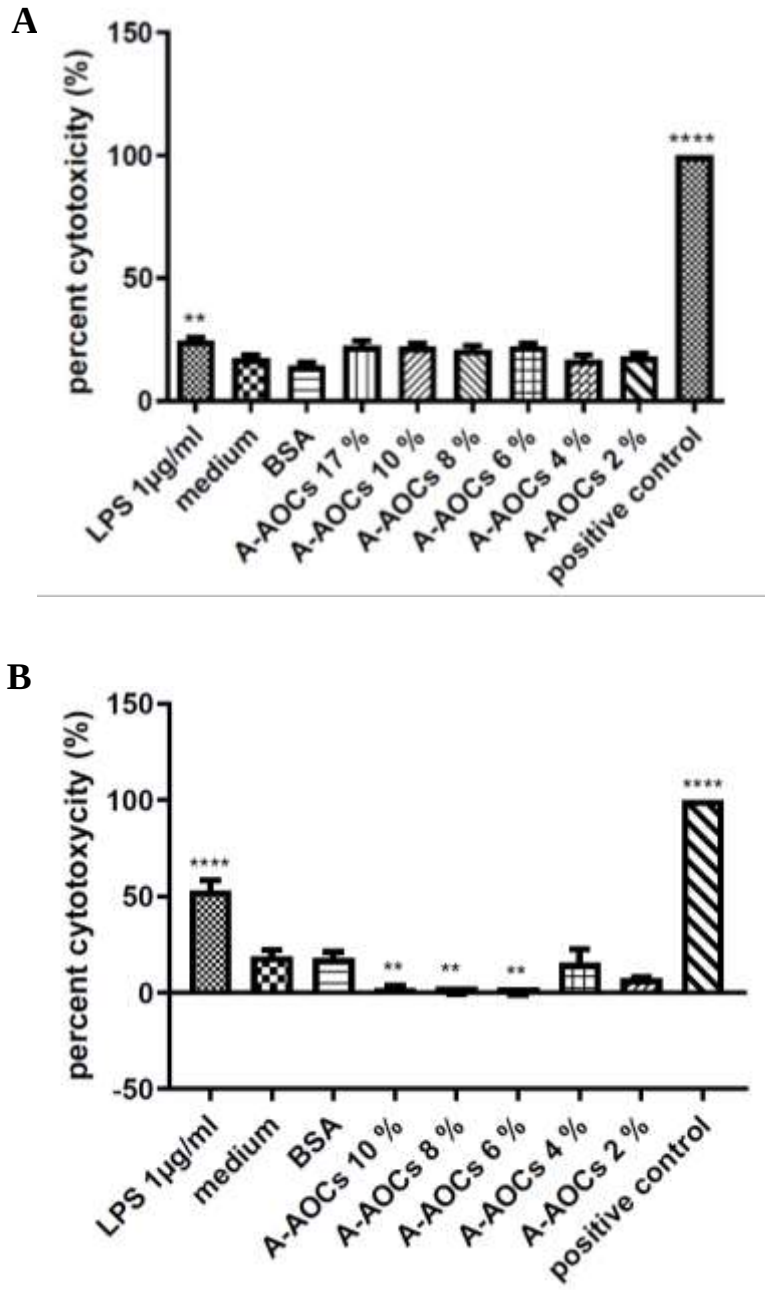

Figure 9: LDH assay in PHM after 4 h and 24 h incubation

PHM were treated with LPS (1 µg/ml), medium, 5 % of BSA or 17 −2 % of A−AOCs for 4 h and 24 h. A: Bar plots represent percent cytotoxicity normalized to positive control after 4 h of exposure. Results are expressed as mean percent cytotoxicity ± SEM: n = 24. B: Bar plots represent percent cytotoxicity normalized to positive control after 24 h of exposure. Results are expressed as mean percent cytotoxicity ± SEM: n = 12. **p< 0.01; ***p< 0.001; **** p< 0.0001; one way ANOVA followed by Dunnett's Multiple Comparison against medium.

6.4.2. Cell viability in J774 measured by LDH assay

Referring to the LDH assay results for J774 (see figure 10 A), a dose-dependent toxicity of A−AOCs was evident after 4 h of exposure, with percent cytotoxicities of 10.31 %, 15.71 %, 27.78 %, 38.94 %, 36.61 %, and 33.60 % for J774 treated with A−AOCs at concentrations of 2 %, 4 %, 6 %, 8 %, 10 %, and 17 %, respectively. Notably, the percent cytotoxicity in J774 treated with A−AOCs at concentrations of 6 %, 8 %, 10 %, and 17 % was significantly higher than that of the medium. Interestingly, cell viability in J774 treated with LPS, 5 % BSA (in medium), and A−AOCs at concentrations of 2% and 4% was not significantly impacted with percent cytotoxicities of 9.70 %, 14.04 %, 10.31 %, and 15.71 %, respectively as compared to medium with a percent cytotoxicity of 17.53 %. However, the positive control demonstrated significant toxicity after 4 h of exposure, with a percent cytotoxicity of 100 %.

The results of LDH assay presented in figure 10 B show that A−AOCs did not significantly affect cell viability of J774 up to the highest tested concentration of 10 % after 24 h incubation with percent cytotoxicities of 34.60 %, 38.79 %, 26. 69 %, 36.29 % and 17.33 % for J774 treated with A−AOCs at the concentrations of 2 %, 4 %, 6 %, 8 % and 10 % respectively. Similarly, LPS and BSA did not significantly impact the cell viability of J774 exhibiting percent cytotoxicities of 18.09 % and 13.86 % as compared to medium. A significant toxicity was only noted in the positive control with a percent cytotoxicity of 100 %, in comparison to the medium with a percent cytotoxicity of 3.74 %.

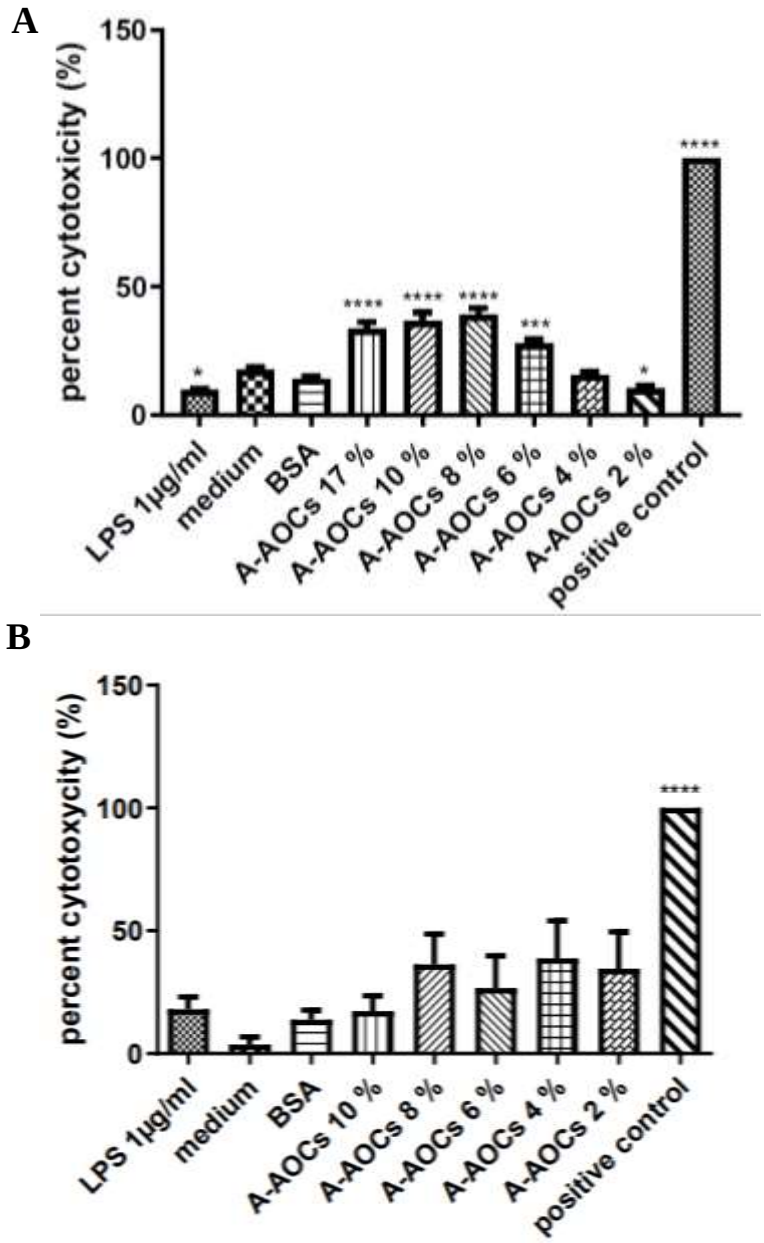

Figure 10: LDH assay in J774 exposed to A−AOCs for 4 h and 24 h

J774 were treated with LPS (1 µg/ml), medium, 5 % of BSA or 17 −2 % of A−AOCs for 4 h or 24 h. (A): Bar plots represent percent cytotoxicity normalized to positive control after 4 h of exposure (A) or 24 h of exposure (B): n = 36 and 12 respectively. Results are expressed as mean percent cytotoxicity ± SEM *p< 0.05; ***p< 0.001; **** p< 0.0001; one way ANOVA followed by Dunnett's Multiple Comparison against medium.

6.4.3. Cell viability in BMDM measured by LDH assay

In line with the J774 results, the LDH assay results for BMDM (see figure 11) indicated a dose-dependent toxicity of A−AOCs after 4 h of exposure, with percent cytotoxicities of 20.65 %, 24.60 %, 27.40 %, 29.44 %, 28.69 %, and 54.21 % for BMDM treated with A−AOCs at concentrations of 2 %, 4 %, 6 %, 8 %, 10 %, and 17 %, respectively. Furthermore, the percent cytotoxicity in BMDM treated with A−AOCs at concentrations of 6 %, 8 %, 10 %, and 17 % was significantly higher than that of the medium. Notably, cell viability was unaffected in BMDM treated with LPS, 5 % BSA (in medium), A−AOCs at concentrations of 2 % and 4 %, with percent cytotoxicities of 19.95 %, 20.65 %, 24.60 %, and 24.60 %, respectively, compared to the medium with a percent cytotoxicity of 21.54 %. However, the positive control exhibited significant toxicity after 4 h of exposure, with a percent cytotoxicity of 100 %.

Lastly, the results presented in figure 11 revealed that A−AOCs did not significantly affect cell viability in BMDM, even at the highest tested concentration of 10 %, after 24 h of incubation, with percent cytotoxicities of 62.14 %, 70.72 %, 62.66 %, 73.84 % and 62.61 % for BMDM treated with A−AOCs at the concentrations of 2 %, 4 %, 6 %, 8 % and 10 % respectively. Similarly, LPS and BSA did not significantly impact the cell viability of BMDM, exhibiting percent cytotoxicities of 11.86 % and 21.04 %, respectively, compared to the medium with a percent cytotoxicity of 41.17 %. Notably, significant toxicity was only observed in the positive control, with a percent cytotoxicity of 100 %, in comparison to the medium.

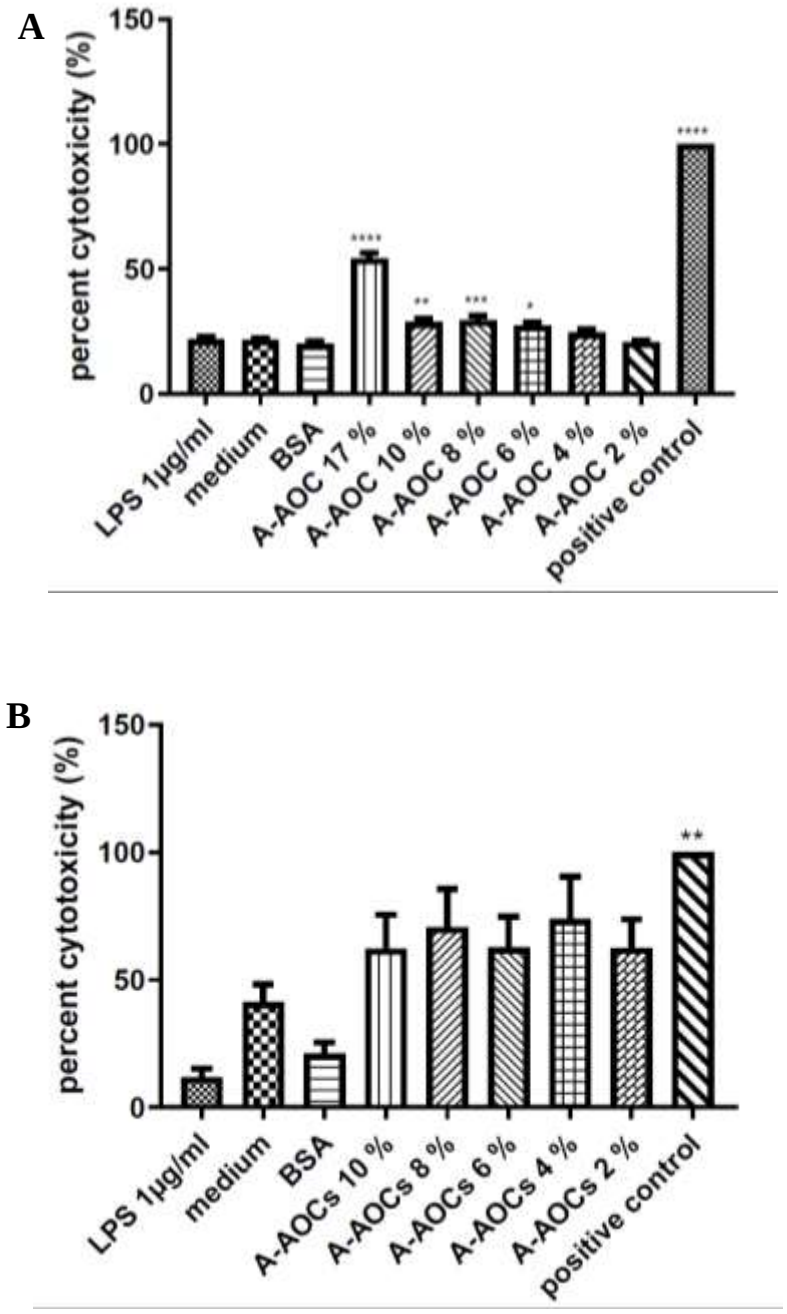

Figure 11: LDH assay in BMDM exposed to A−AOCs for 4 h and 24 h

BMDM were treated with LPS (1 µg/ml), medium, 5% of BSA or 17 −2 % of A−AOCs for 4 h or 24 h. Bar plots represent percent cytotoxicity normalized to positive control after 4 h of exposure (A) or 24 h of exposure (B): n = 51 and 14 respectively. Results are expressed as mean percent cytotoxicity ± SEM.*p< 0.05; **p< 0.01; ***p< 0.001; **** p< 0.0001; one way ANOVA followed by Dunnett's Multiple Comparison against medium.

6.5. Cell death measured by Tunnel assay

The results of TUNEL assay presented in figure 12 show that A−AOCs did not affect cell viability of PHM up to the concentration of 10 % after 4h incubation. The percentage of dead cells for PHM treated with A−AOCs at concentrations of 10 %, 8 %, 6 %, 4 %, and 2 % were 3.91%, 4.45 %, 2.90 %, 3.44 % and 1.47 % respectively. The percentage of dead cells in PHM treated with BSA was also very low (2.30 %). However, the percentage of dead cells significantly increased in PHM treated with LPS (1 µg/ml), positive control and with A−AOCs at the concentration of 17 % with percentage of dead cells of 8.11 %, 109.8 % and 7.19 %, in comparison to medium with a percentage of dead cells of 1.28 % (see figure 12 k). Based on these results the subsequent experiments were performed with A−AOCs up to the concentration of 10 %.

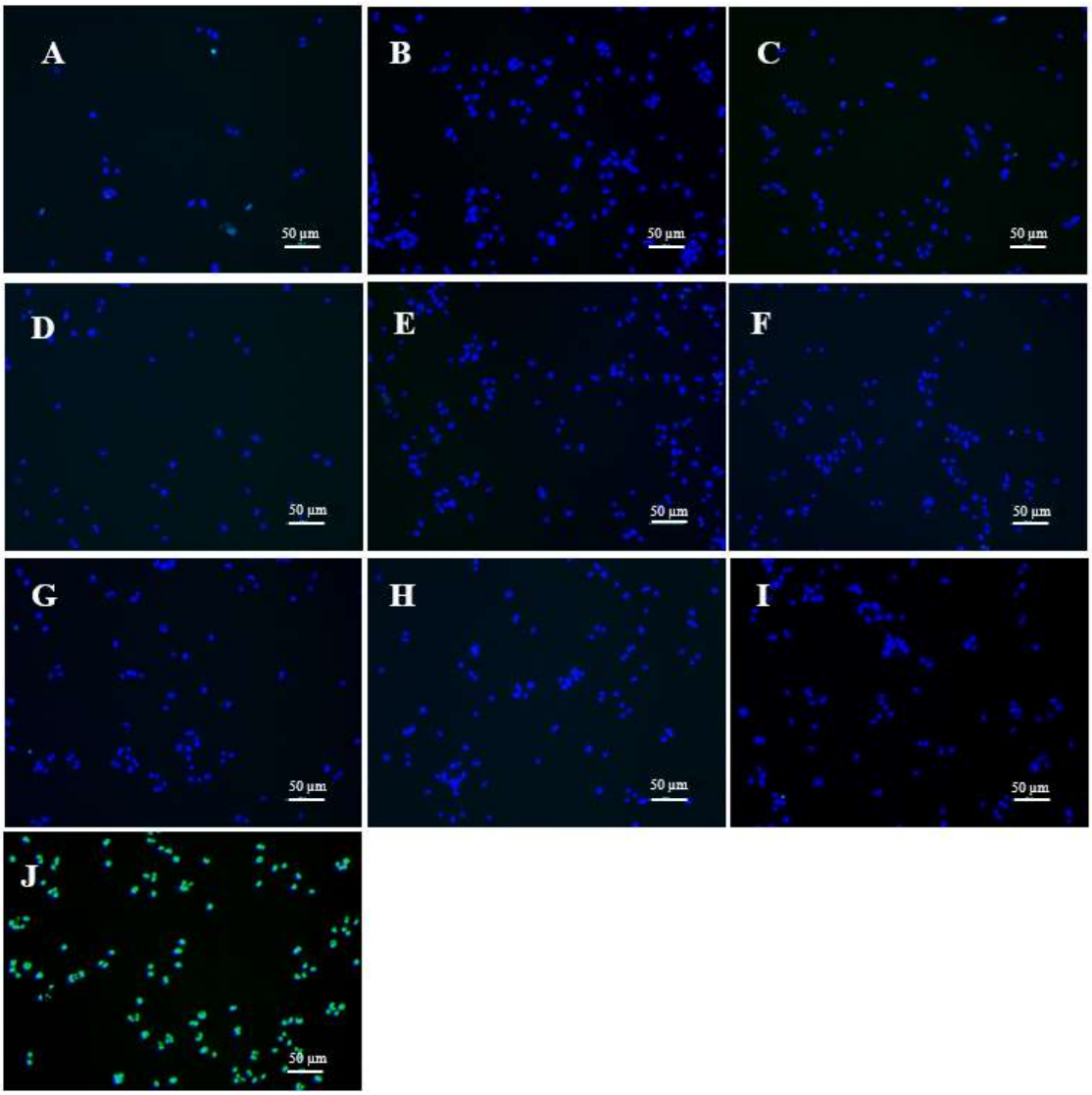
A
50 µm
B
50 µm
C
50 µm
D
50 µm
E
50 µm
F
50 µm
G
50 µm
H
50 µm
I
50 µm
J
50 µm

K

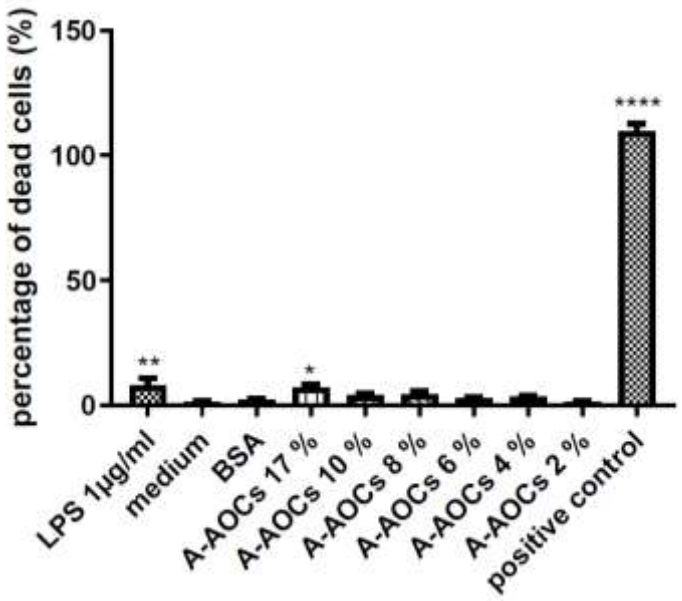

Figure 12: Tunnel assay in PHM exposed to A−AOCs for 4h

PHM ($1x10^4$) were treated with LPS (1 µg/ml), medium, 5% of BSA or 17 −2 % of A−AOCs for 4h. Using the TUNEL assay, dead cells were labelled in PHM. The cell nucleus labelled with Hoechst dye, appear in blue colour and the dead cells appear as green spots. (A): LPS, (B): medium, (C): BSA, (D):17 % of A−AOCs, (E): 10 % of A−AOCs, (F): 8 % of A−AOCs, (G): 6 % of A−AOCs, (H): 4 % of A−AOCs, (I): 2 % of A−AOCs and (J): positive control are representative merge images of 14 FOV for each condition. Bar plots represent the percentage of apoptotic cells normalized to positive control. Results are expressed as mean percentage of dead cells ± SEM. *p< 0.05 **p< 0.01; **** p< 0.0001; one way ANOVA followed by Dunnett's Multiple Comparison against medium; n = 14.

6.6. Cytokine production measured by ELISA

ELISA was performed to measure the protein levels of the selected cytokines TNF-alpha and IL-1 beta in PHM (see figure 13) or TNF-alpha and IL-1 alpha in J774 and BMDM (see figure 14 and 15), respectively. Treatment with 10 −2 % A−AOCs for 24 h had no significant impact on the production of the selected cytokines. In the culture medium, the levels of TNF-alpha ranged from 1 pg/ml to 0 pg/ml in PHM, 0.02 to 0.0 pg/ml in J774, and 1.51 to 4.11 pg/ml in BMDM. As for IL-1beta in PHM after the 24-hour exposure to 10 −2 % A−AOCs, concentrations ranged from 7.45 to 1.93 pg/ml. Furthermore, following a 24-hour exposure to 10 −2 % A−AOCs, IL-1alpha concentrations ranged from 0.02 to 0 pg/ml in J774 and from 0.68 to 0.11 pg/ml in BMDM, respectively.

However, when treated with LPS (1 µg/ml), a potent activator of macrophages, PHM, J774, and BMDM showed a significant increase in cytokine production. In PHM, the concentrations

were 616.3 pg/ml for TNF-alpha and 440.1 pg/ml for IL-1beta. In J774, the concentrations were 343.7 pg/ml for TNF-alpha and 16.48 pg/ml for IL-1alpha. In BMDM, the concentrations were 302.6 pg/ml for TNF-alpha and 28.13 pg/ml for IL-1alpha, all compared to the control medium. In the control medium, the concentration of IL-1beta was 8.9 pg/ml, while the concentrations of TNF-alpha ranged from 1.53 to 7.75 pg/ml, and the concentrations of IL-1alpha ranged from 0.0 to 0.01 pg/ml.

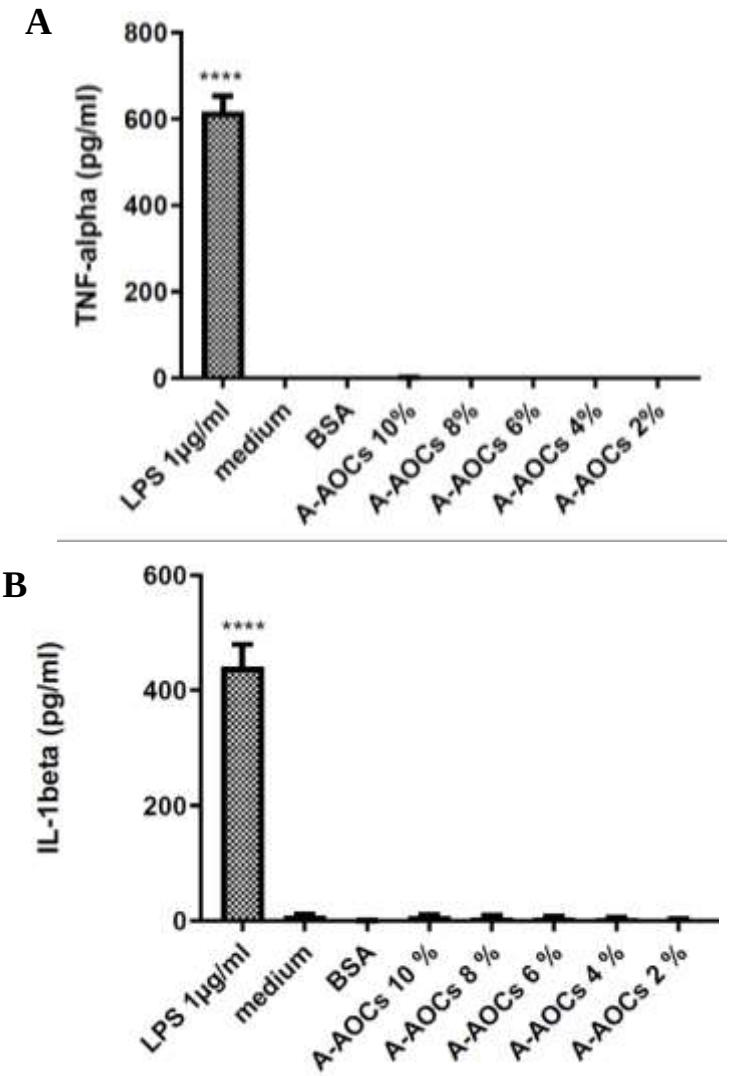

Figure 13: ELISA measurement of TNF-alpha and IL-1beta release in PHM

PHM ($5x10^5$/ ml) were treated with medium, 10 −2 % of A−AOCs, LPS or medium with 5 % BSA for 24 h. Subsequently, the concentrations of TNF-alpha (A) and IL-1beta (B) in the cell culture supernatant were measured using ELISA. Bar plots represent the concentrations of TNF-alpha in pg/ml (A) or IL-1beta in pg/ml (B); results are expressed as mean concentration ± SEM. ****p < 0.001; one-way ANOVA followed by Dunnett's Multiple Comparison against medium; TNF-alpha: n = 7 and IL-1beta: n = 8.

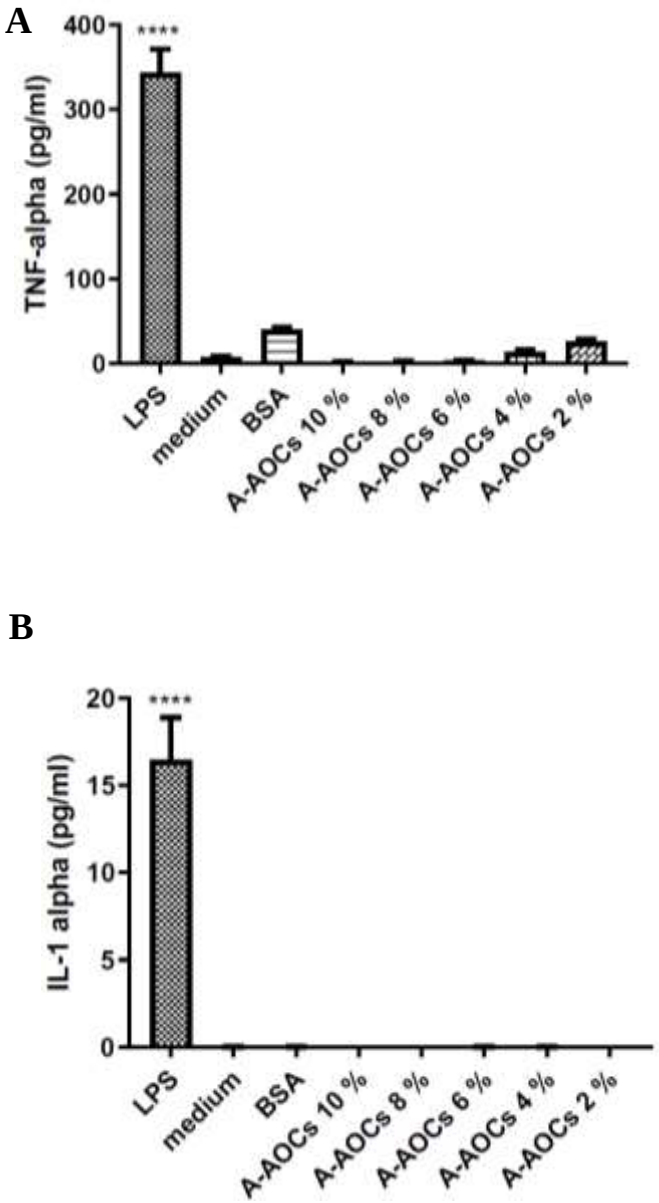

Figure 14: ELISA measurement of TNF-alpha and IL-1 alpha release in J774

J774 were treated with medium, 10 −2 % of A−AOCs, LPS (1µg/ml) or medium with 5 % BSA for 24 h. Subsequently, the concentrations of TNF-alpha (A) and IL-1 alpha (B) in the cell culture supernatant were measured using ELISA. Bar plots represent the concentration of TNF-alpha in pg/ml (A) or IL-1 alpha in pg/ml (B); results are expressed as mean concentration ± SEM. ****p < 0.001; one-way ANOVA followed by Dunnett's Multiple Comparison against medium; TNF-alpha: n = 5 and IL-1alpha: n = 4.

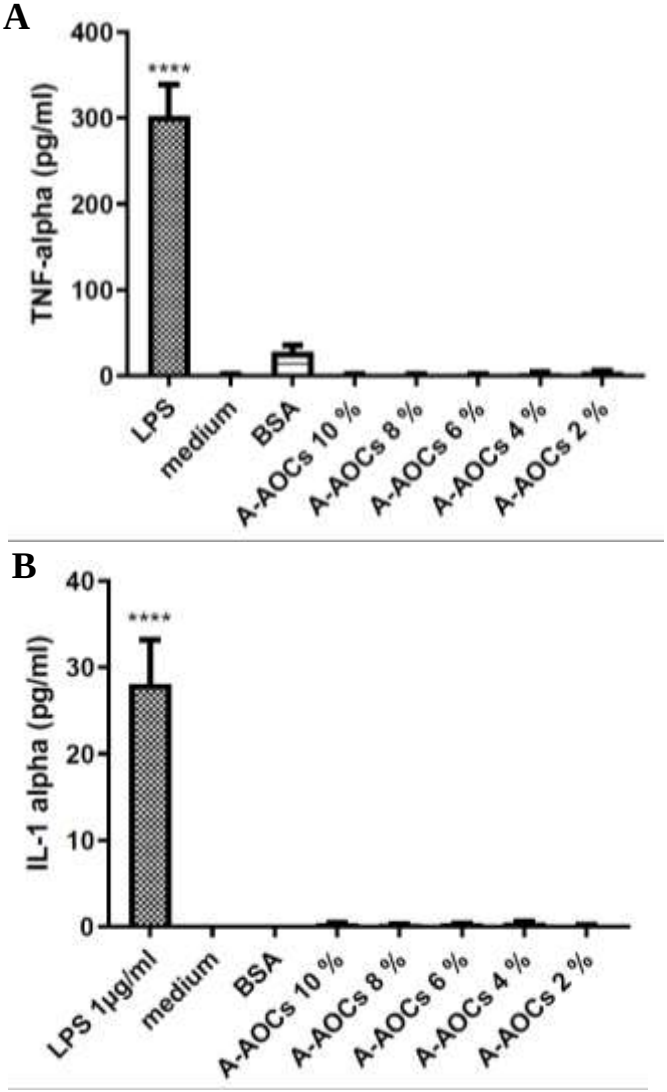

Figure 15: ELISA measurement of TNF-alpha and IL-1alpha release in BMDM

BMDM were treated with medium, 10 −2 % of A−AOCs, LPS (1µg/ml) or medium with 5 % BSA for 24 h. Subsequently, the concentrations of TNF-alpha (A) and IL-1alpha (B) in the cell culture supernatant were measured using ELISA. Bar plots represent the concentration of TNF-alpha in pg/ml (A) or IL-1alpha in pg/ml (B); results are expressed as mean concentration ± SEM. ****$p < 0.001$; one-way ANOVA followed by Dunnett's Multiple Comparison against medium; n = 5.

6.7. mRNA expression of immunologically relevant genes

RT-qPCR was employed to compare ELISA findings with the mRNA expression profiles of selected immunologically relevant genes. Specifically, we analysed TNFA and IL-1B in PHM, and *Tnfalpha* and *Il-1alpha* in J774 and BMDM. Additionally, we investigated other pertinent genes including ICAM1, VCAM1, GLUT1, CXCL8, CD86, and CCR2 in PHM, and *Icam1*, *Vcam1*, *Glut1*, *Cd86*, and *Ccr2* in J774 and BMDM.

In line with the ELISA data, the treatment with A−AOCs at the concentration of 10 −2 % did not have any significant effect on production of the selected cytokines at the mRNA levels in PHM (see figure 16 A and B), J774 (see figure 17 A and B) and BMDM (see figure 18 A and B) after 24 h of exposure. In PHM, the mRNA levels for TNFA and IL1B ranged from 0.8 to 1.7 and 1.4 to 8.9, respectively. In J774 and BMDM, the mRNA levels for *Tnfalpha* ranged from 2.1 to 3.5 and 1.1 to 6.8, respectively, while for *Il-1alpha*, the levels ranged from 0.3 to 4.9 in J774 and 1.0 to 2.1 in BMDM, all compared to a baseline of 1, which represents the medium control's mRNA levels. RT-qPCR confirmed a significant increase in the production of the selected cytokines at the mRNA level only for PHM, J774, and BMDM when treated with LPS (1 µg/ml), a potent activator of macrophages. In the LPS-treated PHM group, mRNA levels of 9.1 (TNFA) and 2289.6 (IL1B) were detected. In the case of J774 and BMDM, mRNA levels of 3.7 (*Tnfalpha* in J774) and 13.1 (*Tnfalpha* in BMDM), as well as 38.27 (*Il-1alpha* in J774) and 40.327 (*Il-1alpha* in BMDM) were measured.

In PHM treated with LPS (1 µg/ml), the mRNA levels of ICAM1, VCAM1, GLUT1, and CXCL8 (see figure 17 C, D, E, and F, respectively) were significantly upregulated with mRNA levels of 82.1, 70.5, 6.1 and 4350, respectively compared to the medium control with mRNA levels of 1. However, when PHM were treated with A−AOCs at a concentration of 10 −2 %, the mRNA levels of these genes remained relatively low with mRNA levels ranging from 2.7 to 9.0, 1.4 to 4.5, 0.6 to 1.9 and 4.5 to 24.2, respectively. The mRNA levels of CD86 (see figure 16 G) significantly increased in PHM treated with both LPS and BSA with mRNA levels of 3.7 and 4.8, respectively compared to the medium control, but this increase was not observed in PHM treated with A−AOCs at a concentration of 10 −2 %, where CD86 mRNA levels remained markedly low with mRNA levels ranging from 0.2 to 0.5. Interestingly, the mRNA levels of CCR2 (see figure 16 H) significantly increased in PHM treated with 5 % BSA, going up to 1.5, while in PHM treated with LPS (1 µg/ml) and A−AOCs (10 −2 %), the mRNA levels of CCR2 significantly decreased. In the case of LPS, it went down to 0.03, and for A−AOCs, it ranged from 0.02 to 0.07 compared to the medium control set at 1.

In contrast, none of the treated J774 showed a significant increase in the mRNA levels of *Icam1*, *Vcam1*, and *Glut1* (see figure 17 C, D and E) with mRNA levels ranging from 0.5 to 1.2; 0.4 to 1.5 and 1.2 to 1.9, respectively when compared to the medium control with mRNA levels set at 1. Notably, the mRNA levels of *Cd86* (see figure 17 F) significantly increased only in J774 treated with A−AOCs at a concentration of 6 % with mRNA levels of 5.5, but not in those

treated with LPS with mRNA levels of 2.5 and other concentrations of A−AOCs with mRNA levels ranging from 1.9 to 4,4, when compared to medium. The mRNA levels of *Ccr2* (see figure 17 G) were significantly decreased in all treated J774 with mRNA levels ranging from 0.1 to 0.3 compared to the medium with mRNA levels set at 1.

Similar to PHM, the mRNA levels of *Icam1* (see figure 18 C) significantly increased in LPS-treated BMDM with mRNA levels of 5.3, but not in those treated with A−AOCs with mRNA levels ranging from 0.6 to 1.6, when compared to the medium control with mRNA levels of 1. However, there was no significant difference in the mRNA levels of *Vcam1* (see to figure 18 D) in any of the treated BMDM with mRNA levels ranging from 0.4 to 1.4 compared to the medium control with mRNA levels of 1. A trend of upregulation in the mRNA levels of *Glut1* and *Cd86* (see figure 18 E and F) was observed in LPS-treated BMDM with mRNA levels of 18.1 and 11.41 respectively, but A−AOCs-treated BMDM exhibited relatively low mRNA levels of these genes with mRNA levels ranging from 1.6 to 9.0 and 0.8 to 1.1for *Glut1* and *Cd86* respectively, when compared to the medium control. No significant difference in the mRNA levels of *Ccr2* (see figure 18 G) was observed in all treated BMDM with mRNA levels ranging from 0.4 to 1.4, when compared to the medium control with mRNA levels set at 1.

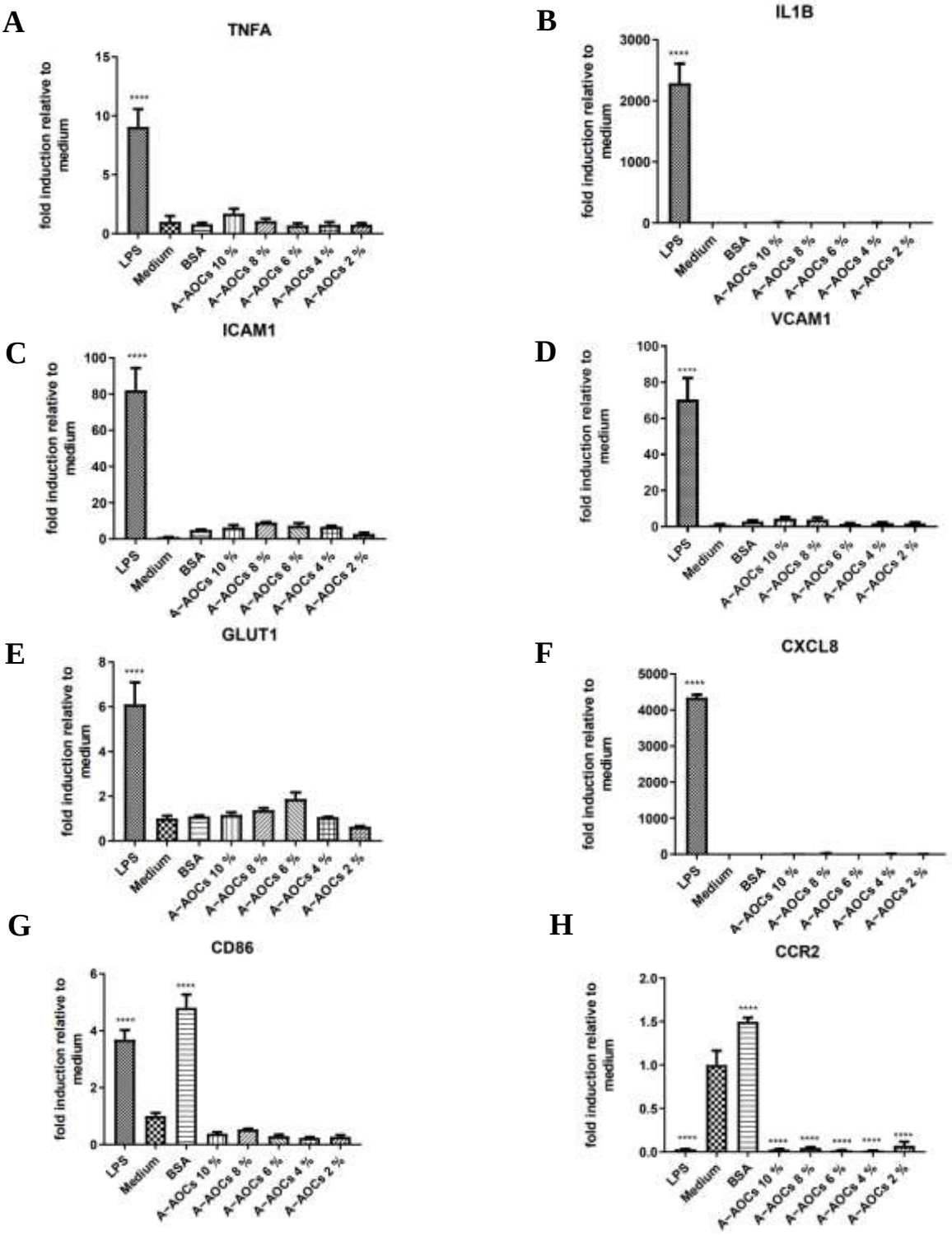

Figure 16: Real-time PCR quantification of fold changes in transcripts of selected immunologically relevant genes in PHM

PHM were treated with medium, 10 −2 % of A−AOCs, LPS (1µg/ml) or medium with 5 % BSA for 24 h. Subsequently, the fold changes in transcripts of TNFA (A), IL1B (B), ICAM1 (C), VCAM1 (D), GLUT1 (E), CXCL8 (F), CD86 (G) and CCR2 (H) were quantified using qPCR. The level of mRNA was normalized to the untreated cells (medium). Bars represent the mean ± SEM; ****p< 0.0001; one way ANOVA followed by Dunnett's Multiple Comparison against medium; n = 4

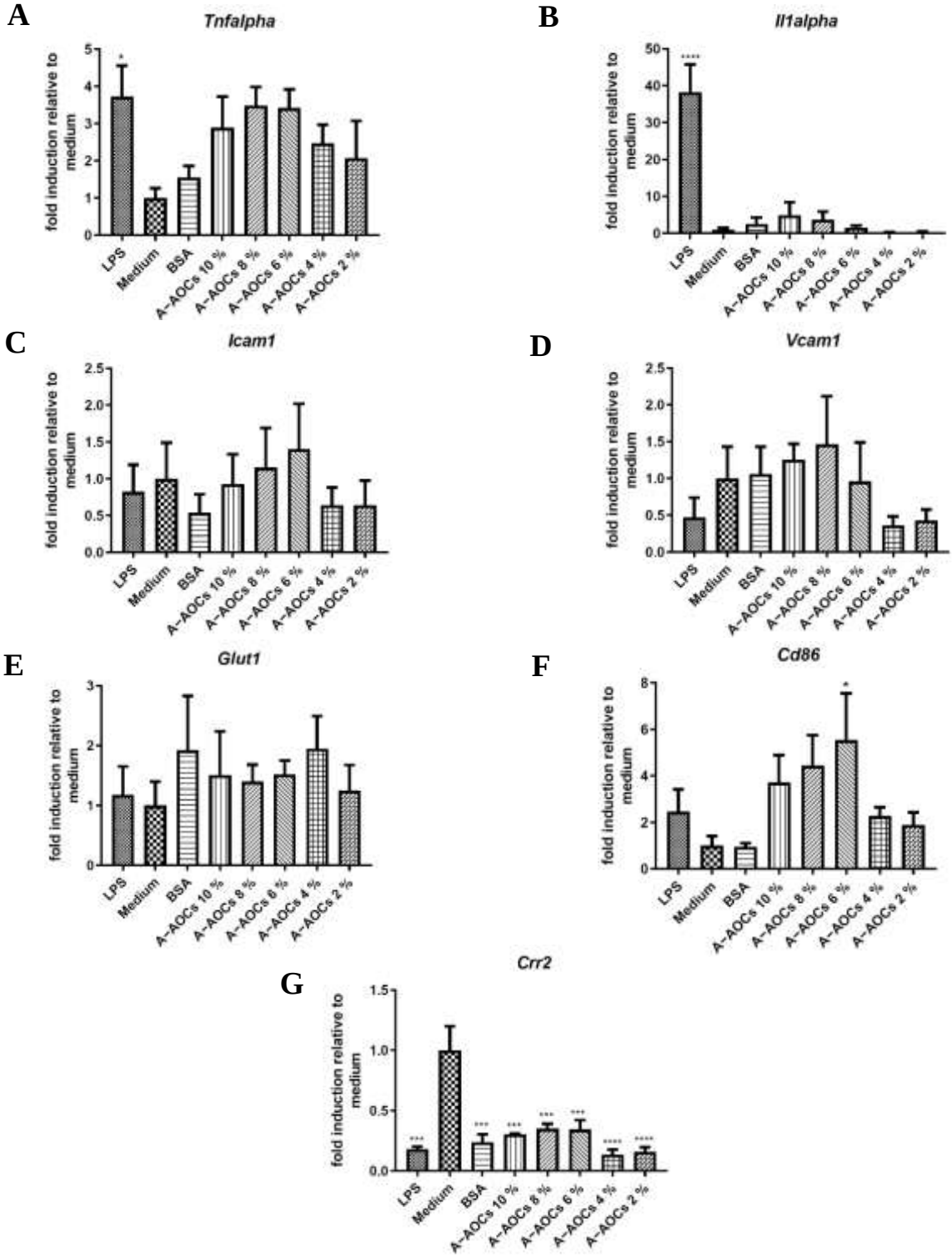

Figure 17: Real-time PCR quantification of fold changes in transcripts of selected immunologically relevant genes in J774

J774 were treated with medium, 10 −2 % of A−AOCs, LPS (1µg/ml) or medium with 5 % BSA for 24 h. Subsequently, the fold changes in transcripts of *Tnfalpha (A), Il1alpha (B), Icam1(C), Vcam1 (E), Glut1 (F), Cd86 (G)* and *Ccr2 (H)* were quantified using qPCR. The level of mRNA was normalized to the untreated cells (medium). Bars represent the mean ± SEM; *p< 0.05; ***p< 0.001; ****p< 0.0001; one way ANOVA followed by Dunnett's Multiple Comparison against medium; n = 3.

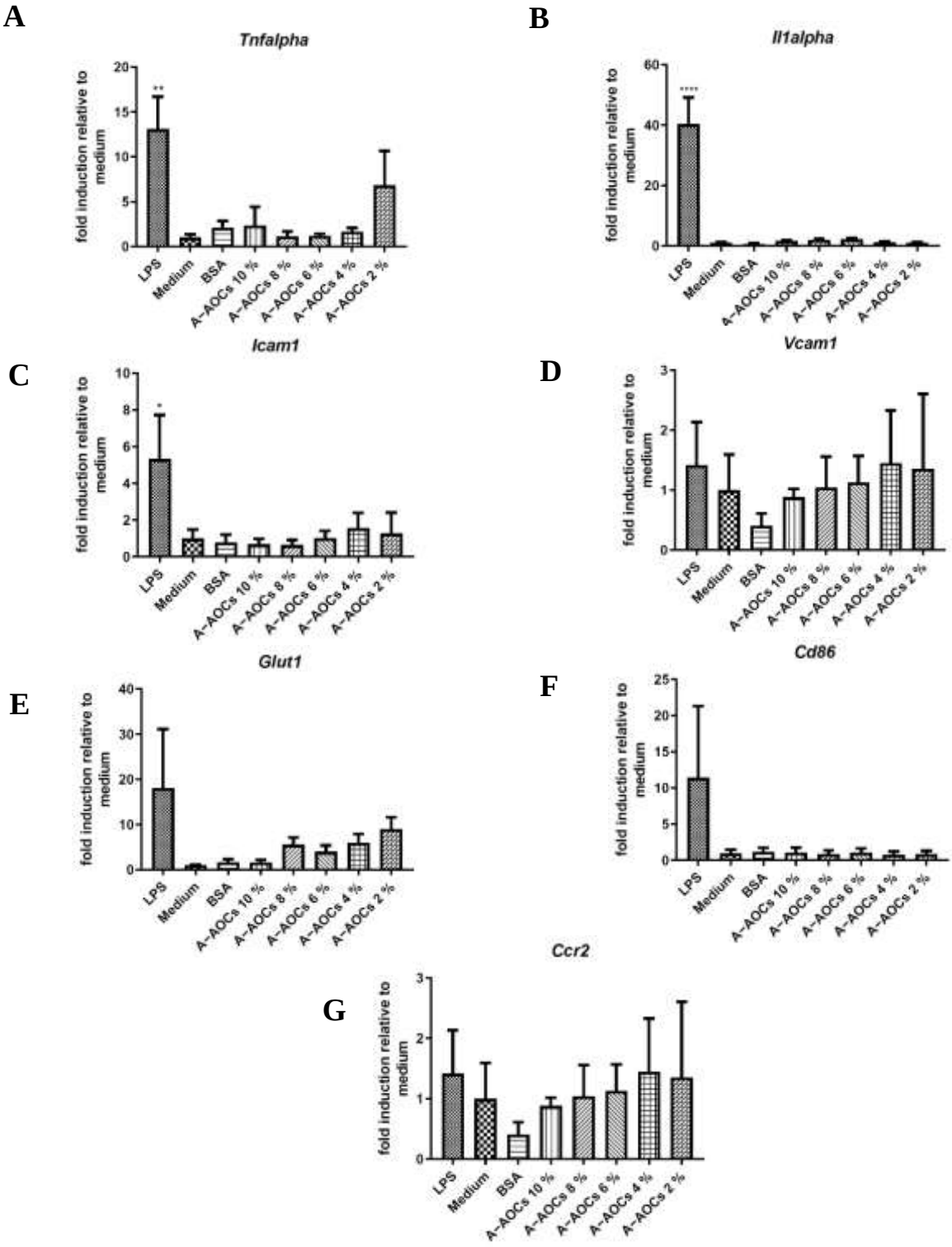

Figure 18: Real-time PCR quantification of fold changes in transcripts of selected immunologically relevant genes in BMDM

BMDM were treated with medium, 10 −2 % of A−AOCs, LPS (1µg/ml) or medium with 5 % BSA for 24 h. Subsequently, the fold changes in transcripts of *Tnfalpha* (A)*, Il1alpha* (B)*, Icam1*(C), *Vcam1*(D), *Glut1* (E), *Cd86* (F) and *Ccr2* (G) were quantified using qPCR. The level of mRNA was normalized to the untreated cells (medium). Bars represent the mean ± SEM; *p< 0.05; **p< 0.01; ****p< 0.0001; one way ANOVA followed by Dunnett's Multiple Comparison against medium; n = 3.

6.8. Uptake of A−AOCs shown by confocal microscopy

Confocal microscopy revealed the uptake of 4 % A−AOCs (green) by 32.54 % of PHM (red) within just 30 min (see figure 19 A and C), and this uptake increased to 57.91 % of PHM after 120 min (see figure 19 B, C) of incubation. Similarly, confocal microscopy demonstrated that J774 (red) exhibited the phagocytic property of macrophages, with 34.29 % uptake of 4 % A−AOCs (green) after 30 min (see figure 20 A and C), which substantially increased to 81.17 % after 120 min of incubation (see figure 20 B and C). Furthermore, the analysis showed that BMDM (red) displayed remarkable phagocytic behaviour as they took up 74.25 % of 4 % A−AOCs (green) within 30 min (see figure 21 A and C), and this uptake further escalated to 94.51 % after 120 min of incubation (see figure 21 B and C). The yellow spots in the confocal images indicate the co-localization of A−AOCs (green) and the cells (red).

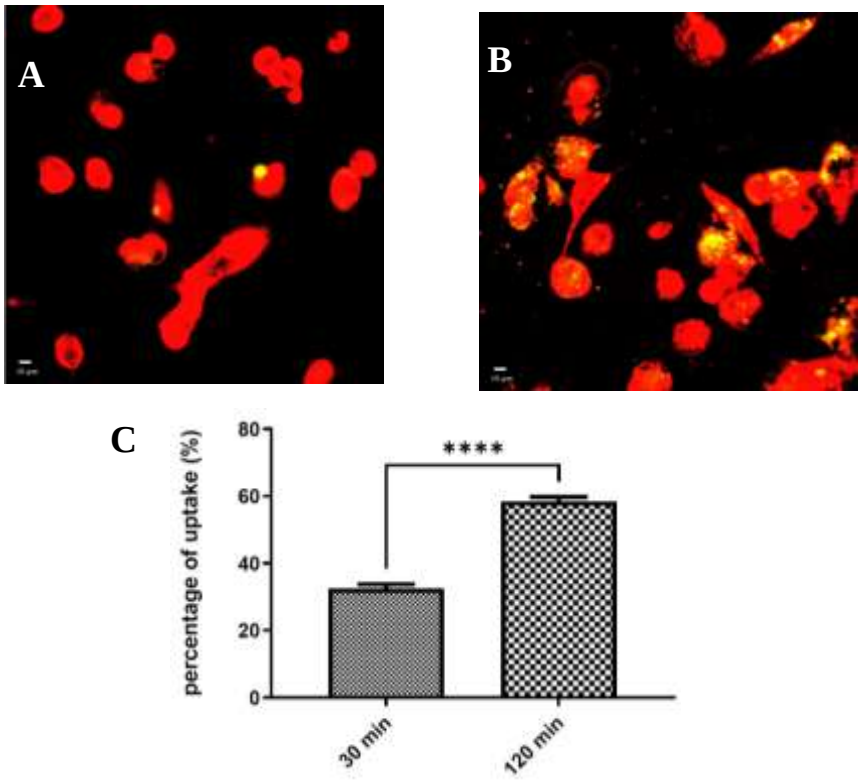

Figure 19: Uptake of A−AOCs by PHM shown by confocal microscopy

PHM were labelled with TRITC-Concanavalin A (100 µg/ml) for 30 min and subsequently incubated with 4 % of FITC-labelled-A−AOCs (1mg/ml) for 30 min (A) or 120 min (B) and visualized at 488 nm and 543 nm with a confocal microscope. The yellow spots in the confocal images (A, B) indicate the co-localization of A−AOCs (green) and the PHM (red). Bar plots represent the percentage of uptake (C). Results are expressed as mean percentage of uptake ± SEM. Magnification: 40x; Bars: 10 µm; representative images from 127 fields of view (FOV) for each time point. Bars represent the mean of 127 FOV, respectively ± SEM; ****$p < 0.0001$; Two tailed, unpaired t test; n = 8.

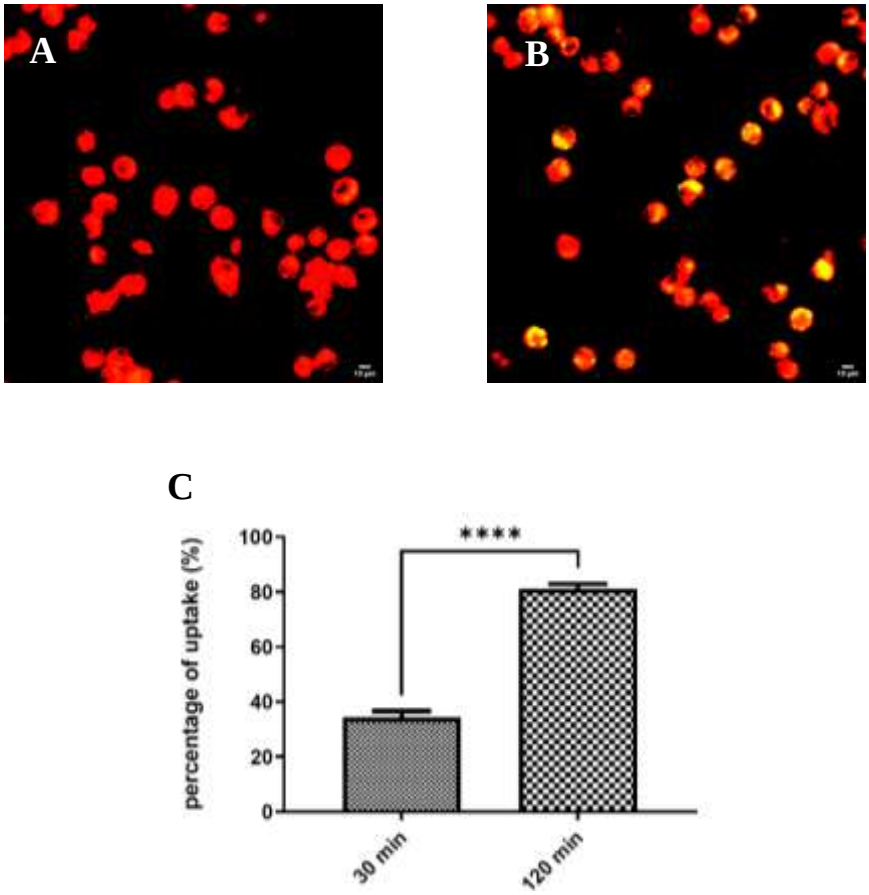

Figure 20: Uptake of A−AOCs by J774 shown by confocal microscopy

J774 were labelled with TRITC-Concanavalin A (100 µg/ml) for 30 min and subsequently incubated with 4 % of FITC-labelled-A−AOCs (1mg/ml) for 30 min (A) or 120 min (B) and visualized at 488 nm and 543 nm with a confocal microscope. The yellow spots in the confocal images (A and B) indicate the co-localization of A−AOCs (green) and the J774 (red). Bar plots represent the percentage of uptake in % (C). Results are expressed as mean percentage of uptake ± SEM. Magnification: 40x; bars: 10 µm; representative images from 53 fields of view (FOV) for each time point. Bars represent the mean of 53 FOV, respectively ± SEM; ****$p < 0.0001$; Two tailed, unpaired t test; n = 8.

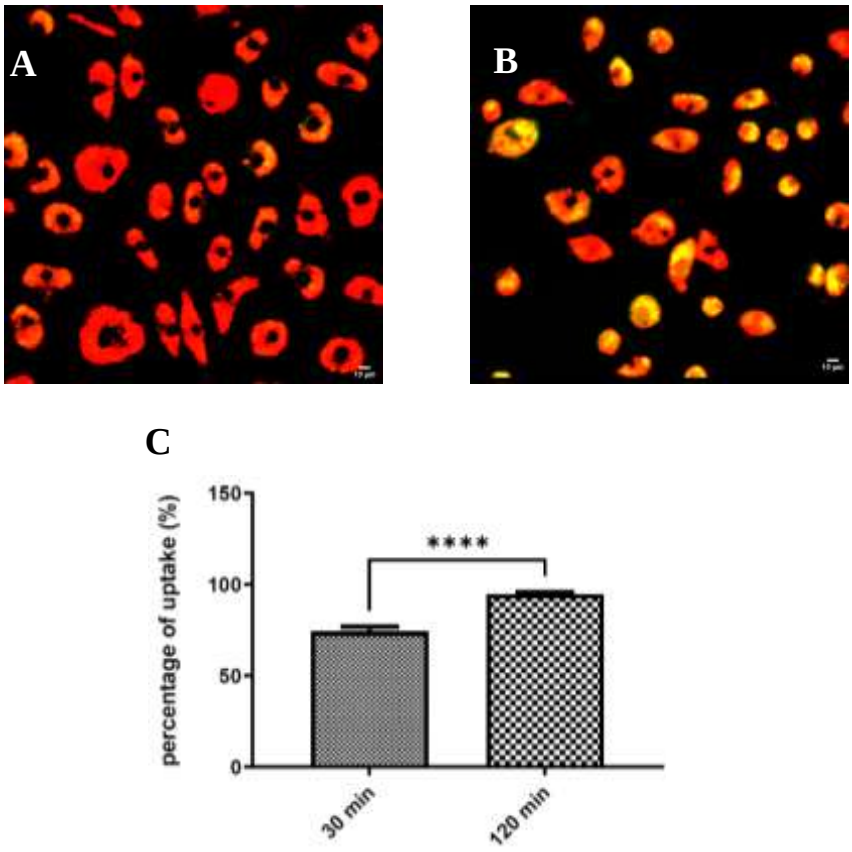

Figure 21: Uptake of A−AOCs by BMDM shown by confocal microscopy

BMDM were labelled with TRITC-Concanavalin A (100 µg/ml) for 30 min and subsequently incubated with 4 % of FITC-labelled-A−AOCs (1mg/ml) for 30 min (A) or 120 min (B) and visualized at 488 nm and 543 nm with a confocal microscope. The yellow spots in the confocal images (A and B) indicate the co-localization of A−AOCs (green) and the BMDM (red). Bar plots represent the percentage of uptake in % (C). Results are expressed as mean percentage of uptake ± SEM. Magnification: 40x; bars: 10 µm; representative images from 114 fields of view (FOV) for each time point. Bars represent the mean of 114 FOV, respectively ± SEM; ****p< 0.0001; Two tailed, unpaired t test; n = 8.

6.9. Uptake of A−AOCs confirmed by TEM

Transmission electron microscopy (TEM) was utilized to validate the confocal microscopy observations and to investigate the intracellular morphology following exposure to A−AOCs. As depicted in figure 22 A and B, TEM imaging affirmed the internalization of A−AOCs by PHM within just 30 min of exposure (figure 22 A), and this internalization persisted even after 120 min of exposure (figure 22 B). Similarly, TEM imaging confirmed the uptake of A−AOCs by J774 and BMDMs at both time points (figure 22 C and D; E and F). It is notable that A−AOCs were predominantly located within lysosomes and heterolysosomes, as indicated by the orange arrows.

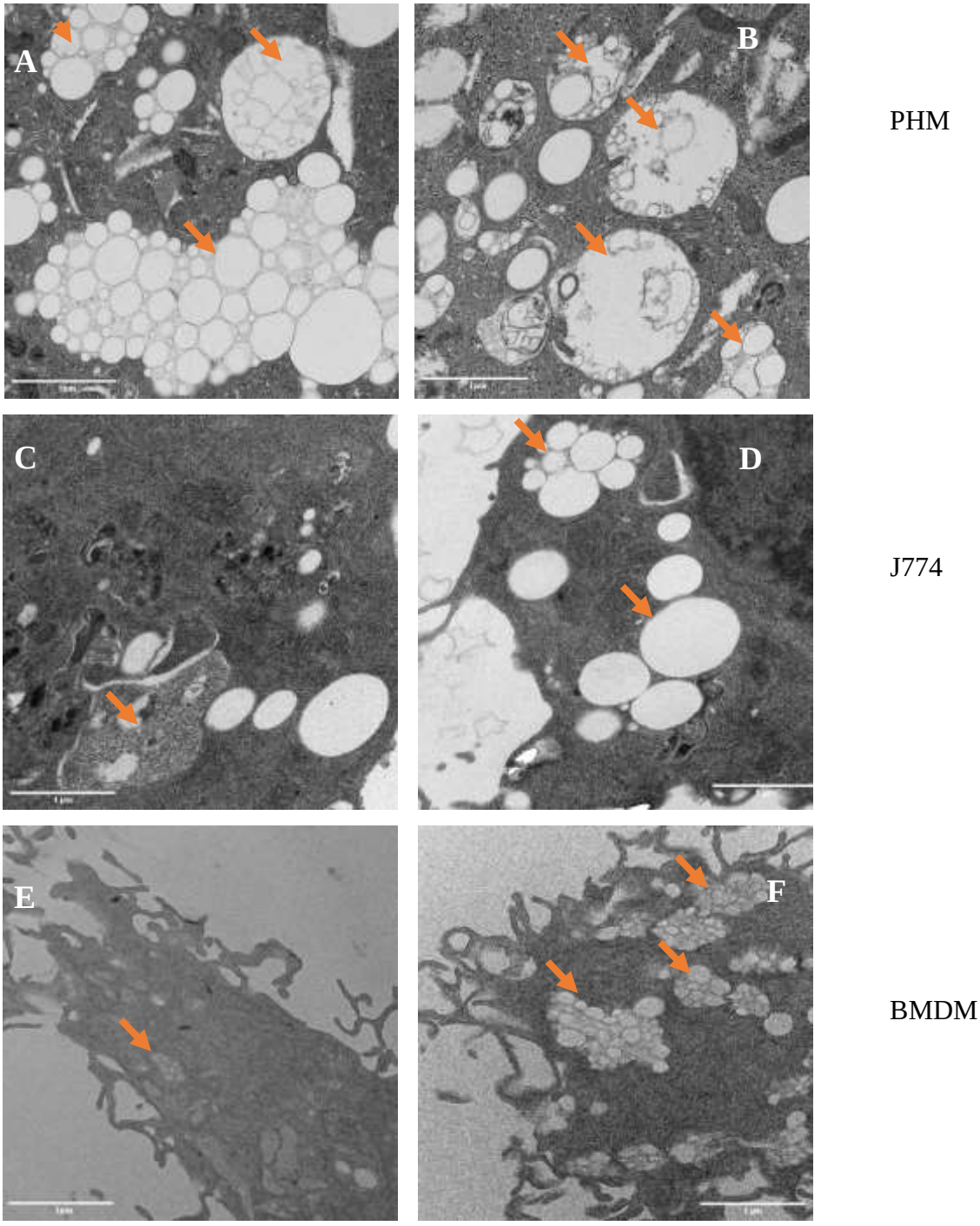

Figure 22: Uptake of A−AOCs by PHM, J774, and BMDM confirmed by TEM

The direct effect of A-AOCs on PHM, J774, and BMDM was observed using transmission electron microscopy (TEM). Cells were treated with 4% A-AOCs for either 30 min or 120 min. Representative TEM images of 26 and 31 FOV are shown for PHM at 30 min (A) and 120 min (B), respectively, 26 and 30 FOV for J774 at 30 min (C) and 120 min (D), respectively, and 29 and 35 FOV for BMDM at 30 min (E) and 120 min (F), respectively. The magnification used was 10000x, and the scale bars represent 1 µm, n = 1.

6.10. Uptake of A−AOCs by J774 confirmed by correlative light and electron microscopy (CLEM)

To confirm the internalization of A−AOCs within cells and to unequivocally pinpoint their presence within macrophages, we exploited CLEM. The outcomes of CLEM, as illustrated in figure 23, validated the presence of FITC-labelled-A−AOCs visually represented as green particles within the cells (see figure 23 A). An example of a cell that exhibited green fluorescence and was still detectable after electron microscopy processing is shown in figure 23 B. Employing the correlation technique, we juxtaposed both, the fluorescent image and TEM image of a selected J774 macrophage, to precisely determine the localization of A−AOCs within the macrophage (see figure 23 C).

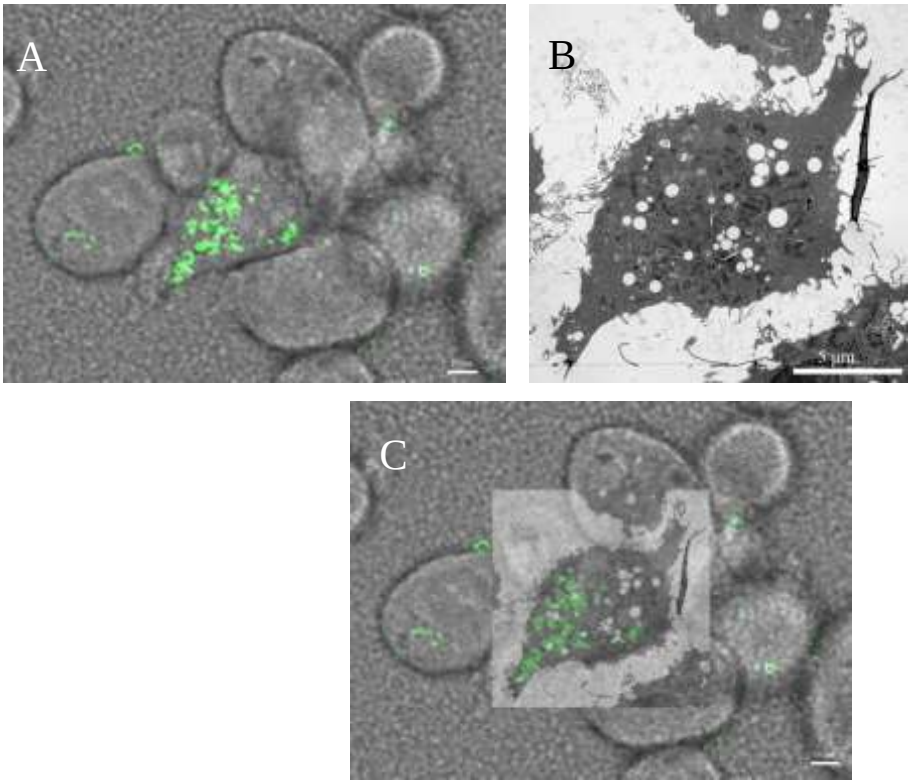

Figure 23: Uptake of A−AOCs by J774 confirmed by CLEM

J774 were labelled with TRITC-Concanavalin A (100 µg/ml) for 30 min and subsequently incubated with 4 % of FITC-labelled-A−AOCs (1mg/ml) for 120 min & visualized regular light and 580 nm with a fluorescent microscope. Additionally, the same sample was examined using TEM. (A) Representative fluorescent images of 75 FOV showing green fluorescence indicative of FITC-labelled-A−AOCs; (B): representative TEM image of a selected cell from 29 FOV; (C): correlation of both, fluorescent image and TEM image of a selected J774 macrophage. The imaging was performed at a magnification of 40x, with scale bars of 10 µm for the fluorescent images and 5000x, with a scale bar of 5 µm, for the TEM images, n = 1.

6.11. Oxygen consumption measured by Oxygraph-2k

To investigate the effect of A−AOCs exposure on the cellular metabolism, we assessed the oxygen consumption rate in both, PHM and J774. Without any cells oxygen level remained constant with 101.6 % in PHM and 102.4 % in J774 (see figure 24 A and B). In the presence of cells, oxygen concentration decreased within the first 10 min indicating vital cells. Importantly, oxygen consumption rate was unaffected by all treatments and was not significantly different to cells treated with pure medium. In PHM we detected 85.6 % (medium), 94.1 % (LPS), 87.4 % (BSA) and 94.3 % (4%A-AOCs) after 10 min measurement. In J774 we detected 77.8 % (medium), 78.7 % % (LPS), 84.1 % (BSA) and 88.8 % (4%A-AOCs) after 10 min of measurement.

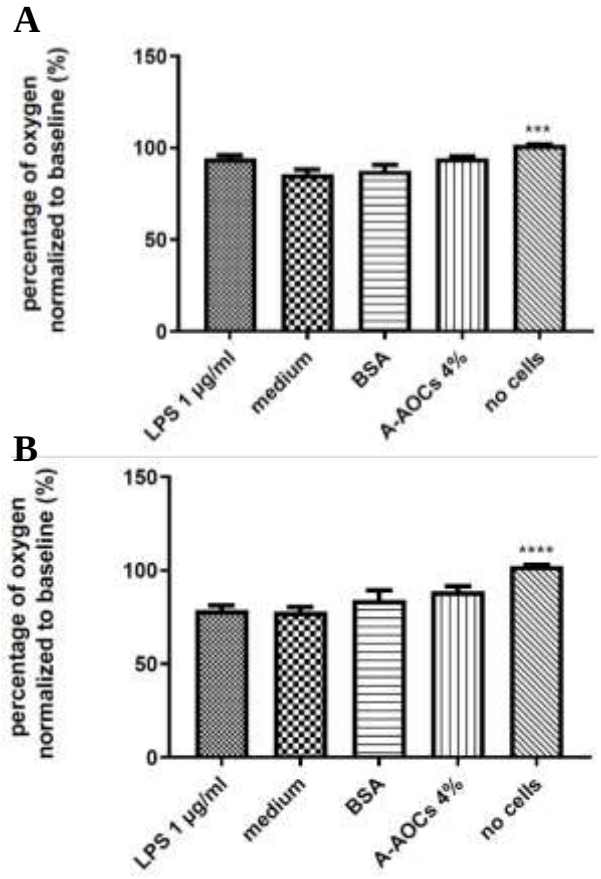

Figure 24: Oxygen consumption rate in PHM and J774

PHM and J774 were treated with medium, 4 % of A−AOCs, LPS (1µg/ml) or medium with 5 % BSA, respectively, for 24 h. After incubation, the oxygen consumption rate in PHM (A) or J774 (B) ($1x10^6$ cells/ml) was measured for 10 min using Oxygraph-2k and the oxygen concentration 10 min after the start of measurement was normalized to the oxygen concentration at 0 min (baseline, start of measurement). Results are presented as mean percentage of oxygen ± SEM. ***$p < 0.001$; one way ANOVA followed by Dunnett's Multiple Comparison against medium; PHM: n = 4; J774: n = 5.

6.12. Lipid peroxidation measured by malondialdehyde (MDA) detection

To assess oxidative stress, we quantified the level of malondialdehyde (MDA), a byproduct of lipid peroxidation, in PHM. The results (see figure 25) demonstrated a significant decrease in MDA levels within PHM treated with 2-10% A−AOCs with MDA concentrations ranging from 0.48 to 0.55 µM, as compared to the control medium with an MDA concentration of 2.17 µM. However, there was no significant difference observed between the control medium and PHM treated with LPS (1µg/ml) with an MDA concentration of 1.95 µM.

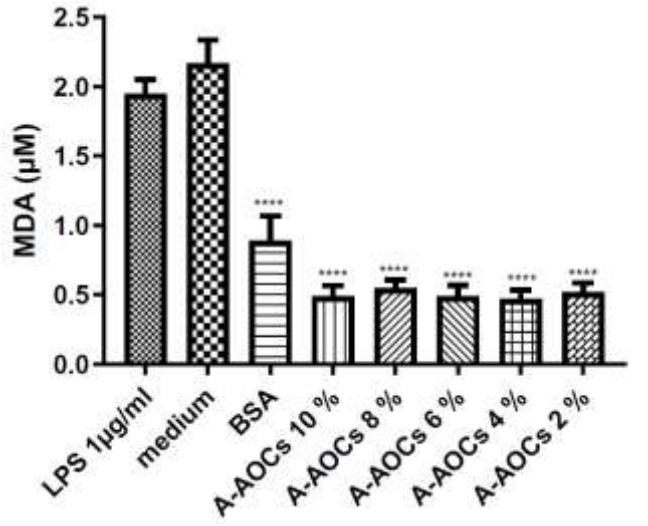

Figure 25: Measurement of MDA release in PHM

PHM ($5x10^5$ cells/ ml) were treated with medium, 10 −2 % of A−AOCs, LPS (1µg/ml) or medium with 5 % BSA, respectively, for 24 h. Subsequently, the concentration of MDA in the cell culture supernatant was measured using the spectrophotometric thiobarbituric acid reactive substances (TBARS) test. Bar plots represent the concentration of MDA in µM. Results are expressed as mean concentration ± SEM; ****p < 0.001; one-way ANOVA followed by Dunnett's Multiple Comparison against medium; n = 4

6.13. Particle size measured by dynamic light scattering (DLS) and viscosity measured by viscosimeter

To assess the stability of A−AOCs in complete cell culture media, 17 % A−AOCs were synthesized in J774 medium or in BMDM medium and their size and viscosity were measured at three time points: immediately after synthesis (0h); after 4h incubation at 37°C (4 h); after 24 h incubation at 37°C (24 h). Moreover, the viscosity of the A−AOCs 17 % was measured at 20°C and at 37°C. In addition, the viscosity at was measured at different shear rates including 100 s-1 and 200 s-1.

For A−AOCs synthesized in J774 medium (see table 19 below), the particle diameter exhibited a significant decrease (from 194.61 ± 48.09 nm to 149.08 ± 15.95 nm after 4 h of incubation, followed by a tendency to increase (from 194.61 ± 48.09 nm to 243.37 ± 77.29 nm) after 24 h. In terms of polydispersity (see table 19 below), there was a significant decrease (from 1.12 ± 0.97 to 0.76 ± 0.1) after 4 h of incubation, followed by a subsequent significant increase (from 1.12 ± 0.97 to 4.19 ± 2.20) after 24 h compared to the initial time point (0 h). The viscosity of A−AOCs in J774 medium (see table 19 below), measured at 20°C with a shear rate of 100 s-1, showed a significant increase after 24 h (3.10 ± 0.35 mPa.s) compared to the initial time point (0h: 2.37 ± 0.23 mPa.s). There were no significant differences in viscosity measured at a shear rate of 100 s-1 at 37°C across the three time points. Similarly, no significant difference was noticeable in viscosity measured at a shear rate of 200 s-1 at 37°C across the three time points. The measurements show that the viscosity decrease with an increased shear rate.

For A−AOCs synthesized in BMDM medium (see table 20) there was no significant difference in particle diameter or polydispersity index in comparison to the 0-hour time point (see table 20). The particle diameter revealed a tendency decrease (from 155.88 ± 10.18 to 121.70 ± 11.71 nm after 4 h of incubation, followed by a tendency to increase (from 155.88 ± 10.18 nm to 170.49 ± 36.36) after 24 h. Regarding the polydispersity (see table 20), a tendency to decrease (from 0.93 ± 0.21 to 0.78 ± 0.24) was observed after 4 h of incubation, followed by a tendency to increase (from 0.93 ± 0.21 to 1.23 ± 0.67) after 24 h compared to the initial time point (0 h). In addition, no significant difference was observed in the viscosity of A−AOCs in BMDM medium (see table 20), measured at both 20°C and 37°C with both shear rates of 100 s-1 and 200 s-1, at the 4h and 24 h time points compared to the initial time point (0 h). However, a tendency for the viscosity to increase from 1.62 ± 0.19 mPa.s to 2.08 ± 0.10 mPa.s and from 1.50 ± 0.17 mPa.s to 1.84 ± 0.17 mPa.s was noticed after 24 h compared to the initial time point (0 h), for the viscosity measured at 37°C with both shear rates of 100 s-1 and 200 s-1 respectively.

Table 19. Particle size measured by DLS, and viscosity measured by viscosimeter for A−AOCs synthesized in J774 medium

Sample	Particle diameter [nm]	polydispersity index (PDI)	Viscosity (at 100 s-1 shear rate) at 20°C [mPa.s]	viscosity (at 100 s-1 shear rate) at 37°C [mPa.s]	viscosity (at 200 s-1 shear rate) at 37°C [mPa.s]
J774 0 h	194.6 ± 48	1.12 ± 1.0	2.4 ± 0.2	1.6 ± 0.3	1.5 ± 0.2
J774 4 h	149.1 ± 16**	0.8 ± 0.1**	2.7 ± 0.4	2.0 ± 0.4	1.7 ± 0.2
J774 24 h	243.4 ± 77	4.2 ± 2****	3.1 ± 0.4**	2.1 ± 0.3	2 ± 0.3

Asterisks indicate significant results. Values represent the mean of four replicates ± SEM; $p < 0.01$ = **; $p < 0.0001$ = ****; one-way ANOVA followed by Dunnett's Multiple Comparison against the initial time point (0 h), n=4.

Table 20. Particle size measured by DLS, and viscosity measured by viscosimeter for A−AOCs synthesized in BMDM medium

Sample	Particle diameter [nm]	PDI	viscosity (at 100 s-1 shear rate) at 20°C [mPa.s]	viscosity (at 100 s-1 shear rate) at 37°C [mPa.s]	viscosity (at 200 s-1 shear rate) at 37°C [mPa.s]
BMDM 0 h	156 ± 10.2	0.9 ± 0.2	2.4 ± 0.2	1.6 ± 0.2	1.5 ± 0.2
BMDM 4 h	122 ± 11.7	0.8 ± 0.2	2.8 ± 0.5	2.0 ± 0.7	1.7 ± 0.4
BMDM 24 h	170.5 ± 36.4	1.2 ± 0.7	2.6 ± 0.4	2.1± 0.1	1.8 ± 0.2

Values represent the mean of four replicates ± SEM; one-way ANOVA followed by Dunnett's Multiple Comparison against the initial time point (0h), n=4.

7. Discussion

Artificial oxygen carriers hold great potential as substitutes for red blood cells in specific medical situations, especially during emergencies, trauma, and major surgeries where rapid and efficient oxygen delivery is crucial [22]. Artificial oxygen carriers could be used to provide immediate oxygenation to tissues and organs when whole blood transfusion is not immediately available or suitable [18]. Additionally, in regions with limited access to blood banks or cases of significant blood loss, such as during major surgeries or trauma artificial oxygen carriers could help maintain oxygen delivery to tissues and organs until the patient's own blood volume is restored or until a compatible blood transfusion is available [25]. Despite their potential advantages, artificial oxygen carriers are not yet widely used in clinical practice due to ongoing research into potential side effects and the stringent approval processes by regulatory bodies like the Food and Drug Administration (FDA) and the European Medicines Agency (EMA). Some existing artificial oxygen carrier products have been tested in clinical trials, but none have been approved for use in Western Europe or the USA due to reported side effects [1]. Recently, a new development of oxygen carriers known as A−AOCs has shown better biocompatibility and longer half-life circulation, resulting in improved oxygen transportation in various animal models [2,99,3]. These A−AOCs have demonstrated good tolerance upon intravenous administration, higher oxygen transport capacity compared to Perftoran®, and stable body parameters that aid in better oxygenation [2]. Studies suggest that A−AOCs can mitigate hypoxic tissue damage and decrease decompression sickness lesions and mortality rates in animal models [4,36,100]. However, the interactions of A−AOCs with immune cells have not been extensively investigated. To address this gap, the current research aimed to evaluate their effects on the immune system using three commonly used macrophage models: PHM, derived from the differentiation of the human monocytic leukaemia cell line THP-1, murine macrophages (J774 and BMDM).

7.1. 10 ng/ml PMA suffice to ensure stable differentiation of THP-1 cells into PHM

Because of their metabolic and morphological similarities, the human monocytic cell line THP-1 can be differentiated into macrophages using PMA. These differentiated THP-1 macrophages are commonly used as an in vitro model for human macrophages, especially to study macrophage functions [8]. In the past, to prepare macrophages from THP-1 cells, PMA has

been used at concentrations as high as 400 ng/ml (540 nM) without considering the upregulation of certain genes [101]. For instance, in some studies, macrophages were differentiated with concentrations of 100 ng/ml PMA that likely exceed physiological levels to assess their effects in *in vitro* macrophage models [98]. Consequently, it was essential to optimize PMA concentrations to minimize the upregulation of genes and prevent the masking of effects from secondary stimuli caused by PMA. Previous research has shown that the expression of various genes, including TNF-a, IL-8, MIP-1b, and IL-1b, significantly increases in THP-1 cells differentiated with PMA at concentrations ranging from 25 ng/ml to 100 ng/ml [98]. Therefore, for the present study, THP-1 cells were differentiated using a lower PMA concentration of only 10 ng/ml. The differentiation process involved incubating THP-1 cells with 10 ng/ml of PMA for 72 h, followed by a 24-hour resting period. The resulting macrophages, referred to as PHM, were evaluated subsequently both, visually under a microscope and molecularly through flow cytometric analysis. When observed under light microscopy, the PHM exhibited attachment and spreading (which display the typical phenotype of macrophages) on the culture plate, even after being washed with PBS (see figure 5 A). To further confirm the effectiveness of using only 10 ng/ml PMA for the differentiation, the expression levels of CD14 were analysed using flow cytometry. CD14 up-regulation is known to be a surface marker of macrophages and, thus, served as an indicator of successful differentiation. Flow cytometry analysis demonstrated a significant increase in CD14 expression in PHM (83.62 %) compared to undifferentiated THP-1 cells (10.45 %), confirming the successful acquisition of the M0 phenotype at the molecular level (see figure 5 B). This outcome supports the notion that 10 ng/ml PMA is adequate for inducing stable differentiation of THP-1 cells into PHM. Consequently, to prevent artificial gene upregulation and enable the detection of PHM responses to mild stimuli, all subsequent experiments were conducted using only 10 ng/ml PMA.

7.2. Our differentiation protocol ensures the stable differentiation of isolated bone marrow cells into fully functional BMDM

BMDM, which stands for Bone Marrow-Derived Macrophages, served as another significant cell line in this study. BMDM, being primary murine macrophages, were obtained from bone marrow cells directly isolated from the bone marrow of mice. The isolated bone marrow cells undergo differentiation in a specific medium enriched with M-CSF to become fully functional BMDM. To verify the successful differentiation of bone marrow cells into BMDM, the cells

were subjected to a 7-day differentiation process. Under light microscopy, the BMDM displayed characteristic phenotypes of macrophages, namely attachment and spreading (see figure 6 A). To further confirm the differentiation of bone marrow-derived monocytes into BMDM at the molecular level, flow cytometry was performed using Pacific Blue-labelled anti-mouse CD11b monoclonal antibody and APC-labelled anti-mouse F4/80 monoclonal antibody. This allowed the analysis of CD11b and F4/80 expression in BMDM, providing additional evidence of successful differentiation. The results revealed significant expression of both CD11b (84.48 %) and F4/80 (90.59 %) in BMDM (see figure 6 B). CD11b is a marker for myeloid cells and F4/80 is well-known as a major marker for identifying murine macrophages (dos Anjos Cassado 2017). This outcome indicates that our differentiation protocol ensures the stable differentiation of isolated bone marrow cells into fully functional macrophages (BMDM).

7.3. A−AOCs result in reduced cell extravasation with no notable impact on cellular migration in PHM

Cell extravasation also called cell adhesion cascade is a critical step during inflammation that involve the expression of ICAM-1. To assess the influence of A−AOCs on cellular extravasation, Western blot analysis of ICAM-1 protein expression in PHM exposed to A−AOCs for 24 h was performed. The result of western blot analysis showed a non-significant increase in ICAM-1 expression in LPS-treated control (see figure 7). However, ICAM-1 significantly decreased in A−AOCs-treated cells (see figure 7). ICAM-1 expression is associated with pro-inflammatory, cytokine-induced conditions [102]. This result suggests that A−AOCs might decrease the induction of pro-inflammatory cytokines that might lead to a decrease in cell extravasation as there is no inflammation to fight. Moreover, the result of the migration assay showed a significant decrease in the number of cells migrated only for BSA-treated PHM but not for A−AOCs-treated PHM (see figure 8). The reduced migration in BSA-treated PHM could be due to higher viscosity of the medium which might increase in the presence of BSA. Higher viscosity can impede cell movement and hinder their ability to migrate efficiently [103]. Furthermore, when A-AOCs are present, cells may receive improved oxygen supply through them, leading to a lack of motivation for migration. This result suggest that A−AOCs has no significant effect on cellular migration.

7.4. A−AOCs at a concentration of up to 4 % are well tolerated by PHM, J774 and BMDM

In PHM, the cell viability was assessed by the LDH as well as Tunnel assay. LDH results after 4 h of exposure revealed a significant increase in cytotoxicity for cells treated with LPS or the lysis buffer (positive control), but no notable cytotoxicity was observed in cells treated with A−AOCs (see figure 9 A). This indicates that A−AOCs did not negatively affect cell viability even at the highest tested concentration of 17 %. On the other hand, LPS and the lysis buffer caused a significant decrease in cell viability after 4 h of exposure. After 24 h of exposure, LDH results confirmed a substantial increase in cytotoxicity for cells treated with LPS and the lysis buffer, while cells treated with A−AOCs at 10-6 % showed a significant decrease in cytotoxicity (see figure 9 B). This supports the conclusion that A−AOCs are well-tolerated by PHM. The tunnel assay results after 4 h of exposure also supported these findings. The results of TUNEL assay, which detects apoptotic cells through immunofluorescent staining, showed a significant rise in the percentage of dead cells for LPS-treated PHM, positive control and for PHM treated with A−AOCs at 17% (see figure 12). However, there was no notable apoptotic cells in PHM exposed to 10 −2 % of A−AOCs (see figure 12). This finding confirms that our A−AOCs, up to a concentration of 10%, are well-tolerated by PHM and do not induce apoptosis in these cells.

In J774 cells, LDH results after 4 h of exposure demonstrated a significant increase in cytotoxicity for cells treated with A−AOCs at 10-6 % or the lysis buffer (positive control) (see figure 10 A). However, no significant increase in cytotoxicity was observed in cells treated with A−AOCs at 4 % (see figure 10 A). This suggests that low doses of A−AOCs are well-tolerated by J774 cells and do not negatively affect their viability. After 24 h of exposure, LDH results showed no significant increase in cytotoxicity in J774 cells, indicating that they might adapt to A−AOCs exposure over 24 h (see figure 10 B).

Similarly, in BMDM, LDH results after 4 h of exposure showed a significant increase in cytotoxicity for cells treated with A−AOCs at 10-6 % or the lysis buffer (positive control) (see figure 11 A). Similar to J774, no significant increase in cytotoxicity was observed in BMDM treated with A−AOCs at 4 % for 4 h (see figure 11 A). This suggests that low doses of A−AOCs are well-tolerated by BMDM as well and do not negatively affect their viability. After 24 h of exposure, LDH results showed no significant increase in cytotoxicity in BMDM, suggesting that they might adapt to A−AOCs exposure over 24 h (see figure 11 B). It appears that J774 and BMDM are more sensitive to A−AOCs compared to PHM and show a dose dependent

cytotoxicity after 4 h exposure. A dose dependent cytotoxicity of iron oxide nanoparticles after 3 and 6 h of incubation was also reported in J774 [104].

Overall, to avoid any cytotoxicity, it would be recommended to use A−AOCs at concentration of 4 %. In earlier research conducted by Jägers and collaborators in 2022, it was demonstrated that A−AOCs at a concentration of 4 % effectively supplied the kidney with oxygen and proved to be the most efficient in preserving the kidney's physiological function [47]. Additionally, in Langendorff-heart experiments, A−AOCs at a 4% concentration also demonstrated the best performance [3].

7.5. Potential activation of macrophages in the presence of A−AOCs

Results from the ELISA measurements showed a significant increase in TNF-alpha and IL-1beta only in the PHM that were treated with LPS, a potent activator of macrophages (see figure 13). However, there was no significant increase in TNF-alpha and IL-1beta observed for PHM exposed to A−AOCs (see figure 13). TNF-alpha and IL-1beta are known for their strong pro-inflammatory and immunomodulatory properties. These cytokines have been shown to bind to their respective receptors, triggering the activation of transcription factors such as activator protein 1 (AP-1) and nuclear factor-kappa B (NF-κB), which further induce genes involved in chronic and acute inflammatory responses [105,106]. TNF-alpha serves various functions, including acting as a potent chemoattractant for neutrophils, stimulating phagocytosis in macrophages, and promoting the production of other pro-inflammatory cytokines like IL-6 and IL-8 [105]. On the other hand, IL-1beta initiates and amplifies a wide array of effects associated with innate immunity and the host's responses to microbial invasion and tissue injury [107]. Previous research has also observed increased TNF-alpha and IL-1beta production in response to LPS exposure in both in vitro experiments using human and murine macrophages [8,108,106]. The findings indicate that LPS exposure leads to a significant rise in TNF-alpha and IL-1beta production in PHM, indicating an enhanced pro-inflammatory response driven by macrophage activation and the release of these cytokines. Contrarily, exposure to A−AOCs did not result in any significant increase in TNF-alpha and IL-1beta production in PHM, suggesting that A−AOCs do not activate PHM (see figure 13). The ELISA results indicated a striking similarity in the production of TNF-alpha and IL-1alpha in both, J774 (see figure 14) and BMDM (see figure 15). A significant increase in TNF-alpha and IL-1alpha was observed

exclusively in J774 and BMDM treated with LPS, a potent macrophage activator (see figure 14 and 15, respectively). However, no significant increase in TNF-alpha and IL-1alpha was found in J774 and BMDM exposed to A−AOCs (see figure 14 and 15, respectively). The elevated levels of TNF-alpha and IL-1alpha indicate that LPS effectively stimulated these macrophages to become activated (M1 phenotype) and exert their immune functions. Activated macrophages become more efficient in phagocytosis, enabling them to engulf and eliminate pathogens [109]. Furthermore, they enhance antigen presentation, contributing to an improved immune response. Additionally, the release of these cytokines from macrophages triggers the production of other pro-inflammatory cytokines like IL-6 and IL-8, further amplifying the immune response [105]. The results demonstrate that A−AOCs up to 10 % concentration do not activate J774 or BMDM, as no significant increase in TNF-alpha and IL-1alpha was observed in response to their exposure to A−AOCs up to 10 %. In this study, we focused on assessing the release of IL-1alpha in J774 and BMDM, as it has been shown to play a more crucial role in activated murine macrophages than IL-1beta. Previous research findings support this emphasis. For example, Hirano's study in 2017 showed that IL-1alpha played a more critical role than IL-1beta in inducing IL-6 release in murine macrophages exposed to fibrous titanium dioxide [110]. Moreover, Keneko's study in 2019 reported that IL-1alpha exhibited greater potency than IL-1beta in inducing neutrophil recruitment and lung inflammation in mice following intratracheal administration [111].

Using Quantitative Polymerase Chain Reaction (qPCR), we observed a significant increase in the expression of key immune-related genes, specifically TNFA, IL1B, ICAM1, VCAM1, GLUT1, and CXCL8, exclusively in PHM that were treated with LPS, a potent activator of macrophages (see figure 16 A, B, C, D, E and F, respectively). However, there was no notable increase in PHM exposed to 10 −2 % of A−AOCs (see figure 16). The heightened expression of VCAM-1 and ICAM-1, recognized indicators of pro-inflammatory states, was linked to the presence of TNF-α and IL-1beta [112]. These cell adhesion molecules play a crucial role in facilitating the attachment of leukocytes to endothelial surfaces [112]. This suggests that these adhesion molecules present on macrophages and other antigen-presenting cells, such as dendritic cells and B cells, might assist in lymphocyte adhesion, thus contributing to antigen presentation and lymphocyte activation [112]. Another significant finding was the elevated expression of GLUT1, a glucose transporter isoform, in LPS-treated PHM (see figure 16 E). This suggests that activated PHM have increased energy demands, and GLUT1 facilitates

glucose transport into these cells to meet their heightened energy requirements. Elevated GLUT1 expression results in enhanced glucose uptake, metabolism, and a potentially hyper-inflammatory state [113]. Notably, the study of Obaid in 2021 indicated that LPS induces GLUT1 expression in macrophages through various signaling pathways, including NF-κB, reflecting a metabolic adaptation that supports immune functions and overall survival [114]. Furthermore, CXCL8, also known as IL-8, was found to be significantly increased in PHM cells treated with LPS (see figure 16 F). CXCL8 acts as a potent chemoattractant, guiding neutrophils to sites of tissue injury [115]. In contrast, CCR2 mRNA expression showed an increase in PHM cells treated with BSA, but a decrease in cells treated with LPS or A−AOCs (see figure 16 H). These findings suggest that macrophages may tend to accumulate at sites rich in LPS, attracting other innate immune cells, particularly neutrophils, through the production of CXCL8, rather than relying on CCR2. Interestingly, the mRNA level of CD86 increased significantly in both, LPS- and BSA-treated PHM cells (see figure 16 G). The increase in CD86 expression could enhance immune responses by engaging with CD28 on the surface of T cells, providing a co-stimulatory signal [116,117]. Contrariwise, the interaction between CD86 and inhibitory receptors like cytotoxic T-lymphocyte antigen 4 (CTLA-4) on T cells might downregulate T cell activation, preventing excessive immune reactions and promoting immune tolerance [116,117]. Hence, we postulate that the elevated CD86 expression in PHM treated with LPS could potentially engage with CD28 receptors on T cell surfaces, reinforcing T cell activation and intensifying the T cell's reaction to the antigen. Contrarily, in PHM treated with BSA, the elevated CD86 levels may interact with inhibitory receptors like CTLA-4 on T cells, preventing excessive immune reactions and promoting immune tolerance. These results of qPCR are consistent with ELISA results, confirming that while LPS at a concentration of 1µg/ml fully activates PHM, A−AOCs up to a concentration of 10 % do not activate PHM.

In analyzing J774 cells, qPCR showed significant increases in *Tnfalpha* and *IL1alpha* expression in LPS-treated cells but not in those treated with A−AOCs (see figure 17 A and B). This aligns with ELISA results, confirming that A−AOCs do not activate J774 cells, even at the mRNA level. Moreover, *Icam1* expression was significantly increase in LPS-treated cells but not in those treated with A−AOCs (see figure 17 C). *Icam1* expression is associated with pro-inflammatory, cytokines-induced conditions [102]. Intriguingly, Vcam1 expression did not significantly increase after 24 h of exposure to LPS and A−AOCs in J774 (see figure 17 D). Glut1 expression did not significantly increase after 24 h of exposure to LPS and A−AOCs in

J774 (see figure 17 E), indicating that glucose consumption remained relatively stable during the period investigated. Interestingly, *Cd86* significantly increased only in A−AOCs at a concentration of 6 % (see figure 17 F). Given this, we postulate that *Cd86,* induced by A−AOCs, may interact with inhibitory receptors like CTLA-4 on T cells, thereby preventing excessive immune reactions and promoting immune tolerance [116,117]. Ccr2 expression significantly decreased in J774 treated with both LPS and A−AOCs (see figure 17 G). This finding is consistent with previous research by Zhou and his colleagues in 1999 [118] which demonstrated a LPS-induced down-regulation of *Ccr2* expression.

In BMDM, *Tnfalpha, Il1alpha*, and *Icam1* were significantly elevated only in LPS-treated BMDM, with no notable increase observed in A−AOCs-treated BMDM following 24 h of exposure (see figure 18 A, D and C). This is congruent with ELISA findings, affirming that A−AOCs, even up to 10 %, do not activate BMDM at the mRNA level. Intriguingly, *Vcam1* and *Ccr2* expression did not significantly increase after 24 h of exposure to LPS and A−AOCs in BMDM (see figure 18 D and G). *Glut1* and *Cd86* expression showed a tendency to increase significantly in LPS-treated BMDM (see figure 18 E and F), suggesting heightened glucose uptake, metabolism, and a potentially hyper-inflammatory state, in line with prior research [113].

Overall, the collective results from ELISA and qPCR experiments demonstrate that A−AOCs up to 10% do not activate PHM, J774, and BMDM. However, subtle differences in gene expression were observed among these three cell lines.

To investigate cellular uptake upon exposure to 4 % A−AOCs, we employed LSM on PHM, J774, and BMDM. LSM demonstrated an uptake of A−AOCs by all three cell types: PHM, J774, and BMDM within just 30 min of exposure (see figures 19 A, 20 A and 21 A, respectively). This uptake increased further after 120 min of exposure (see figure 19 B, 20 B and 21 B). The colocalization of A−AOCs and macrophages showed up as yellow fluorescence in the overlay between green fluorescent A−AOCs and the red fluorescent macrophage. Many nanoparticles were observed within the macrophages, indicating their rapid entry into the cell cytoplasm, in line with findings from previous studies [119,120]. For instance, in a study conducted by Nicolete and her colleagues in 2011 using poly lactic-co-alycolic acid nanoparticles with J774 macrophages, LSM revealed that a significant portion of the

nanoparticles were localized intracellularly, and enhanced uptake was observed after 4 h of incubation [119].

To confirm cellular uptake and investigate intracellular morphology upon exposure to 4 % A−AOCs, we employed TEM on PHM, J774, and BMDM. While TEM is commonly utilized for nanoparticle characterization, concerns regarding potential specimen damage from high-voltage electron beams have been reported [121]. However, in our study, the primary aim of TEM was to detect the presence of A−AOCs within cells. TEM imaging confirmed the internalization of A−AOCs by all three cell types: PHM, J774, and BMDM (see figure 22). These particles were predominantly located in the form of aggregates and agglomerates within cellular vesicles, particularly heterolysosomes. This distribution pattern suggests that the internalization of particles likely occurred through an active process, possibly involving endocytosis. This outcome aligns with the observations made by Brzicova and her colleagues in 2019, illustrating the internalization of nanoparticles by THP-1 macrophage-like cells using transmission electron microscopy [8].

Confirmation of A−AOCs uptake by J774 macrophages was achieved through correlative light and electron microscopy (CLEM). CLEM result indicated that the green fluorescence indicative of FITC-labelled-A−AOCs which was visualized in J774 with Light Microscopy was indeed present in the electron microscopy imaging of the same cells (see figure 23). This alignment provided robust evidence that the green fluorescence associated with FITC-labelled-A−AOCs accurately corresponds to the localization of A−AOCs in the TEM images. This outcome enabled the clear identification of our A−AOCs within the macrophages. The application of CLEM has been employed in numerous studies to investigate the cellular internalization of nanoparticles [122,123].

In summary, our results indicate that macrophages did, in fact, take up A−AOCs, as demonstrated by TEM, LSM, and CLEM analyses. However, subsequent activation by A−AOCs post-internalization was not observed, as confirmed by our cytokine and mRNA measurements.

7.6. A-AOCs do not exert a significant influence on mitochondrial respiration and, in fact, lead to a reduction in MDA release.

Using the Oxygraph-2k to measure oxygen consumption rate, we found that there was no significant change in the rate of oxygen consumption in both, PHM and J774 cells, after being exposed to LPS and A−AOCs for 24 h, compared to cells in the culture medium (see figure 24). Since oxygen consumption rate reflects mitochondrial respiration [124], these findings suggest that A−AOCs might not have a significant impact on mitochondrial respiration. Interestingly, there was a tendency for oxygen consumption to decrease after 24 h of exposure to LPS (see figures 24). Previous research has shown that immediately after treating mouse aortic endothelial cells with LPS (at 5 and 10 µg/ml) and NADPH (at 100 µM), the oxygen consumption rate significantly increased, but this effect was reversed 1 hour after exposure under similar conditions [125]. This suggests that LPS might reduce the oxygen consumption rate in PHM and J774 cells after a prolonged period of exposure.

To evaluate oxidative stress, the level of malondialdehyde (MDA), a byproduct of lipid peroxidation, was measured in PHM. The outcomes displayed a significant reduction in MDA within PHM treated with A−AOCs compared to the control medium (see figure 25). This suggests that concentrations of A−AOCs up to 10 % might impede MDA release and it might imply that the A−AOCs are influencing macrophages to show a reduced inflammatory response. Diminished MDA concentrations in PHM could signify a decline in oxidative stress, as MDA is released in response to oxidative stress and lipid peroxidation [126]. Furthermore, oxidative stress and lipid peroxidation products like MDA can contribute to inflammation [127]. This finding aligns with the outcomes of ELISA analyses targeting inflammatory markers within PHM, which revealed very low levels of inflammatory makers (TNF-alpha and IL-1beta) in A−AOCs-treated PHM.

7.7. A−AOCs may exhibit potential instability when synthesized in complete cell culture media

To assess the stability of A−AOCs in complete cell culture media, two syntheses were employed: one in J774 culture medium and another in BMDM culture medium. Particle size was measured in dispersions immediately after synthesis (0 h) and after storing them in a 37°C CO_2 incubator for 4 and 24 h. A−AOCs synthesized in J774 culture medium displayed a significant decrease in particle diameter after 4 h of incubation, followed by a tendency towards

an increase after 24 h (see table 19). Similarly, A−AOCs synthesized in BMDM culture medium showed a non-significant decrease in particle diameter after 4 h, followed by a tendency towards an increase after 24 h (see table 20). This initial reduction in particle size within 4 h might be attributed to the evaporation of PFD, causing the A−AOCs to shrink. Jägers' work in 2021 highlighted PFD evaporation as a cause for the reduction in particle size in oxygen carriers, detectable within 5 min [128]. Our findings suggest that the impact of PFD evaporation might extend to at least 4 h. After 24 h of incubation at 37°C, particle size tended to increase, possibly due to coalescence. If albumin molecules are reversibly bound to the surface, they could spontaneously dissolve post-synthesis, supporting immediate coalescence and leading to a broad particle size distribution. Jägers' research also demonstrated a size increase during storage at 4°C, being rapid during the first 5 days and slowing down in the following 18 days [128]. Regarding polydispersity of A−AOCs synthesized in J774 culture medium, a significant decrease was noted after 4 h of incubation, followed by a subsequent significant increase after 24 h, compared to the initial measurement at 0 h (see table 19). In contrast, A−AOCs synthesized in BMDM culture medium exhibited a non-significant decrease in polydispersity after 4 h, followed by a non-significant increase after 24 h, compared to the initial measurement (see table 20). This trend aligns with the particle size measurements. Jägers' work illustrated that extensive reversible binding of albumin molecules can lead to their spontaneous dissolution post-preparation, resulting in immediate coalescence and a broader particle size distribution, indicated by an increasing polydispersion index [128].

The slight distinction between A−AOCs synthesized in J774 culture medium and those in BMDM culture medium likely arises from differences in ion content between the two media. It has been reported that certain nanoparticles are prone to ionization and aggregation in ion-rich biocompatible solutions [8].

At 20°C, under a shear rate of 100 s-1, the viscosity of A−AOCs within the J774 culture medium showed a significant rise after 24 h compared to the initial measurement at 0h. However, there were no significant difference in viscosity when measured at 37°C under the same shear rate across the three time points (see table 19). Similarly, the viscosity of A−AOCs within the BMDM culture medium, measured at both 20°C and 37°C under a shear rate of 100 s-1, did not exhibit significant differences at the time points 4h and 24 h compared to the baseline measurement at 0 h (see table 20). Nonetheless, it was noted that the viscosity at 37°C was markedly lower than that at 20°C, implying a decline in viscosity as the temperature increased.

Furthermore, at the same temperature the viscosity decreased with increasing shear rate. This observation suggests that the viscosity of A−AOCs is influenced by both the shear rate and temperature. In line with these findings, a study by Wrobeln in 2017 also demonstrated a decrease in the viscosity of A−AOCs with higher shear rates [2]. Consequently, it can be stated that the viscosity of A−AOCs within both mediums is reliant on the shear rate, underlining the characterization of A−AOCs as a Newtonian fluid [46,2].

8. Conclusion

In conclusion, this study investigated the effects of A−AOCs on three immune cell models including the human primary macrophages (PHM) derived from THP-1 cells, murine bone marrow-derived macrophages (BMDM), and murine macrophages (J774). These models are widely recognized for their suitability in investigating macrophage responses to nanoparticles. The results demonstrated that only 10 ng/ml PMA could already effectively differentiate THP-1 cells into macrophages without inducing artificial gene upregulation, confirming the suitability of this protocol for subsequent experiments. The investigation into the influence of A−AOCs on cell extravasation and migration elucidated the potential impact of A−AOCs on immune cell behaviour. It was found that A−AOCs might modulate the inflammatory response by reducing ICAM-1 expression which could have implications for immune cell trafficking during inflammation. Moreover, the observed decrease in ICAM-1 expression suggests the potential to alleviate pro-inflammatory cytokines and subsequent cell extravasation. Additionally, the improved oxygen supply through A-AOCs may lead to a lack of motivation for cell migration. These results collectively indicate that A-AOCs may play a crucial role in regulating inflammatory processes and immune cell behaviour. Furthermore, the study extensively evaluated the impact of A−AOCs on cell viability. The findings indicated that A−AOCs were generally well-tolerated by PHM, J774, and BMDM, suggesting their potential safety for these cell types at different concentrations. Interestingly, high concentrations of A−AOCs seemed to influence the cell viability in J774 and BMDM, with lower concentrations (of up to 4 %) showing better tolerance. We also investigated the effects of A−AOCs on protein and gene expression relevant to the immune response. The results demonstrated that A−AOCs did not significantly activate macrophages, as confirmed at both the protein and mRNA levels, highlighting their non-immunogenic nature. The comprehensive investigation involving confocal laser scanning and transmission electron microscopy confirmed the phagocytic behaviour of macrophages towards A−AOCs, indicating their potential uptake by immune cells. The inclusion of functional assays, such as oxygen consumption rate measurements and lipid peroxidation assay in the present study provided insights into potential metabolic and oxidative stress effects induced by A−AOCs exposure. The results suggested that A−AOCs might not significantly impact mitochondrial respiration or induce oxidative stress.

Collectively, this work contributes to our understanding of the interactions between A−AOCs and immune cells, especially macrophages, elucidating their biocompatibility and provide valuable insights for the development of safer and more effective oxygen carriers for clinical applications.

9. Perspectives

The present study offers valuable insights into the potential use of albumin-derived perfluorocarbon-based artificial oxygen carriers (A−AOCs) as substitutes for red blood cells in specific medical contexts. While the current research has predominantly focused on evaluating the effects of A−AOCs on immune cells, specifically macrophages, it set the stage for further investigation into the broader interactions that A−AOCs may have within the body. In particular, the interactions with endothelial cells and red blood cells emerge as crucial areas for future research and exploration. As A−AOCs are administered intravenously and come into direct contact with the bloodstream, their interaction with endothelial cells lining blood vessels is of paramount importance. Endothelial cells play a pivotal role in regulating vascular tone, blood coagulation, inflammation, and immune responses [129]. Investigating how A−AOCs influence endothelial cell behaviour, integrity, and function is imperative to understanding their overall impact on the vascular system. This research could elucidate whether A−AOCs induce any changes in endothelial cell activation, adhesion molecule expression, or release of vasoactive compounds [130]. Furthermore, considering the central role of red blood cells in oxygen transport, it is essential to examine how A−AOCs might interact with these cells. Red blood cells not only carry oxygen but also contribute to blood viscosity and flow dynamics. Investigating the compatibility of A−AOCs with red blood cells is vital to ensuring that their presence does not interfere with blood viscosity, oxygen-carrying capacity, or other essential functions. It would also be pertinent to assess whether A−AOCs have any influence on red blood cell aggregation or potential alterations in their biomechanical properties. To investigate these aspects, advanced techniques such as confocal microscopy, transmission electron microscopy, atomic force microscopy and flow-based assays could be employed to visualize and quantify the interactions between A−AOCs, endothelial cells, and red blood cells. These investigations could provide insights into potential changes in cell morphology, adhesion, aggregation, and activation states. Furthermore, the potential impact of A−AOCs on various blood parameters, such as clotting factors and plasma proteins, should be thoroughly examined to ensure their safety and efficacy in clinical applications. Comprehensive studies that encompass both, *in vitro* experiments and animal models will be essential to gain a global understanding of the interactions between A−AOCs, blood components, and vascular cells. As the development and application of A−AOCs continue to advance, addressing these critical areas of investigation is crucial to refining their design, optimizing their efficacy, and ensuring

their safety for use in clinical scenarios. By expanding the research focus to incorporate interactions with endothelial cells and red blood cells, this study's findings could contribute significantly to advancing the field of A−AOCs and their potential as life-saving interventions in emergency and surgical situations.

10. References

[1] K.B. Ferenz, A.U. Steinbicker, Artificial Oxygen Carriers-Past, Present, and Future-a Review of the Most Innovative and Clinically Relevant Concepts, The Journal of pharmacology and experimental therapeutics 369 (2019) 300–310.

[2] A. Wrobeln, J. Laudien, C. Groß-Heitfeld, J. Linders, C. Mayer, B. Wilde, T. Knoll, D. Naglav, M. Kirsch, K.B. Ferenz, Albumin-derived perfluorocarbon-based artificial oxygen carriers: A physico-chemical characterization and first in vivo evaluation of biocompatibility, European journal of pharmaceutics and biopharmaceutics: official journal of Arbeitsgemeinschaft fur Pharmazeutische Verfahrenstechnik e.V 115 (2017) 52–64.

[3] A. Wrobeln, K.D. Schlüter, J. Linders, M. Zähres, C. Mayer, M. Kirsch, K.B. Ferenz, Functionality of albumin-derived perfluorocarbon-based artificial oxygen carriers in the Langendorff-heart †, Artificial cells, nanomedicine, and biotechnology 45 (2017) 723–730.

[4] A. Wrobeln, J. Jägers, T. Quinting, T. Schreiber, M. Kirsch, J. Fandrey, K.B. Ferenz, Albumin-derived perfluorocarbon-based artificial oxygen carriers can avoid hypoxic tissue damage in massive hemodilution, Scientific reports 10 (2020) 11950.

[5] A. Sheinenzon, M. Shehadeh, R. Michelis, E. Shaoul, O. Ronen, Serum albumin levels and inflammation, International journal of biological macromolecules 184 (2021) 857–862.

[6] R. Raoufinia, A. Mota, N. Keyhanvar, F. Safari, S. Shamekhi, J. Abdolalizadeh, Overview of Albumin and Its Purification Methods, Advanced pharmaceutical bulletin 6 (2016) 495–507.

[7] H.H. Gustafson, D. Holt-Casper, D.W. Grainger, H. Ghandehari, Nanoparticle Uptake: The Phagocyte Problem, Nano today 10 (2015) 487–510.

[8] T. Brzicova, E. Javorkova, K. Vrbova, A. Zajicova, V. Holan, D. Pinkas, V. Philimonenko, J. Sikorova, J. Klema, J. Topinka, P. Rossner, Molecular Responses in THP-1 Macrophage-Like Cells Exposed to Diverse Nanoparticles, Nanomaterials (Basel, Switzerland) 9 (2019).

[9] D. Hirayama, T. Iida, H. Nakase, The Phagocytic Function of Macrophage-Enforcing Innate Immunity and Tissue Homeostasis, International journal of molecular sciences 19 (2017).

[10] G. Arango Duque, A. Descoteaux, Macrophage cytokines: involvement in immunity and infectious diseases, Frontiers in immunology 5 (2014) 491.

[11] S.B. Flohé, H. Agrawal, S. Flohé, M. Rani, J.M. Bangen, F.U. Schade, Diversity of interferon gamma and granulocyte-macrophage colony-stimulating factor in restoring immune dysfunction of dendritic cells and macrophages during polymicrobial sepsis, Molecular medicine (Cambridge, Mass.) 14 (2008) 247–256.

[12] I. Gessner, Optimizing nanoparticle design and surface modification toward clinical translation, MRS bulletin 46 (2021) 643–649.

[13] H.-H. Li, J. Li, K.J. Wasserloos, C. Wallace, M.G. Sullivan, P.M. Bauer, D.B. Stolz, J.S. Lee, S.C. Watkins, C.M. St Croix, B.R. Pitt, L.-M. Zhang, Caveolae-dependent and -independent uptake of albumin in cultured rodent pulmonary endothelial cells, PloS one 8 (2013) e81903.

[14] S. Lemaire, M.-P. Mingeot-Leclercq, P.M. Tulkens, F. van Bambeke, Study of macrophage functions in murine J774 cells and human activated THP-1 cells exposed to oritavancin, a lipoglycopeptide with high cellular accumulation, Antimicrobial agents and chemotherapy 58 (2014) 2059–2066.

[15] Z. Wang, X. He, B. Tang, X. Chen, L. Dong, K. Cheng, W. Weng, Polarization behavior of bone marrow-derived macrophages on charged P(VDF-TrFE) coatings, Biomaterials science 9 (2021) 874–881.

[16] J. Meier, D. Filipescu, S. Kozek-Langenecker, J. Llau Pitarch, S. Mallett, P. Martus, I. Matot, Intraoperative transfusion practices in Europe, British journal of anaesthesia 116 (2016) 255–261.

[17] H.W. Kim, A.G. Greenburg, Artificial oxygen carriers as red blood cell substitutes: a selected review and current status, Artificial organs 28 (2004) 813–828.

[18] J.S. Jahr, N.R. Guinn, D.R. Lowery, L. Shore-Lesserson, A. Shander, Blood Substitutes and Oxygen Therapeutics: A Review, Anesthesia and analgesia 132 (2021) 119–129.

[19] Andreas Greinacher, A population-based longitudinal study on the implication of demographic changes on blood donation and transfusion demand, blood advances 1 (2017) 867-874.

[20] H. Eichler, A.K. Feyer, K. Weitmann, W. Hoffmann, O. Henseler, A. Opitz, A. Patek, D.N. Hans, L. Schönborn, A. Greinacher, Population-Based Analysis of the Impact of Demographics on the Current and Future Blood Supply in the Saarland, Transfusion medicine and hemotherapy : offizielles Organ der Deutschen Gesellschaft fur Transfusionsmedizin und Immunhamatologie 48 (2021) 175–182.

[21] C.I. Castro, J.C. Briceno, Perfluorocarbon-based oxygen carriers: review of products and trials, Artificial organs 34 (2010) 622–634.

[22] N. Mohanto, Y.-J. Park, J.-P. Jee, Current perspectives of artificial oxygen carriers as red blood cell substitutes: a review of old to cutting-edge technologies using in vitro and in vivo assessments, Journal of Pharmaceutical Investigation 53 (2023) 153–190.

[23] M. Njoku, D. St Peter, C.F. Mackenzie, Haemoglobin-based oxygen carriers: indications and future applications, British journal of hospital medicine (London, England : 2005) 76 (2015) 78–83.

[24] D. Mayer, K.B. Ferenz, Perfluorocarbons for the treatment of decompression illness: how to bridge the gap between theory and practice, European journal of applied physiology 119 (2019) 2421–2433.

[25] F.T. Barbosa, M.J. Jucá, A.A. Castro, J.L. Duarte, L.T. Barbosa, Artificial oxygen carriers as a possible alternative to red cells in clinical practice, Sao Paulo medical journal = Revista paulista de medicina 127 (2009) 97–100.

[26] C. Stephan, C. Schlawne, S. Grass, I.N. Waack, K.B. Ferenz, M. Bachmann, S. Barnert, R. Schubert, M. Bastmeyer, H. de Groot, C. Mayer, Artificial oxygen carriers based on perfluorodecalin-filled poly(n-butyl-cyanoacrylate) nanocapsules, Journal of microencapsulation 31 (2014) 284–292.

[27] K. Ferenz, Künstliche Sauerstoffträger Wie lange müssen wir noch warten?, Hämotherapie 25 (2015).

[28] M.P. Krafft, J.G. Riess, Therapeutic oxygen delivery by perfluorocarbon-based colloids, Advances in colloid and interface science 294 (2021) 102407.

[29] Katja Bettina Ferenz, Künstliche Sauerstoffträger. Wie lange müssen wir noch warten?, Hämotherapie (2015).

[30] A. Pape, O. Habler, Alternatives to allogeneic blood transfusions, Best practice & research. Clinical anaesthesiology 21 (2007) 221–239.

[31] J. Jägers, A. Wrobeln, K.B. Ferenz, Perfluorocarbon-based oxygen carriers: from physics to physiology, Pflugers Archiv : European journal of physiology 473 (2021) 139–150.

[32] J.G. Riess, Understanding the fundamentals of perfluorocarbons and perfluorocarbon emulsions relevant to in vivo oxygen delivery, Artificial cells, blood substitutes, and immobilization biotechnology 33 (2005) 47–63.

[33] M.A. Miller, E.M. Sletten, Perfluorocarbons in Chemical Biology, Chembiochem : a European journal of chemical biology 21 (2020) 3451–3462.

[34] M.S. Jayaraman, K. Graham, E.C. Unger, Injectable oxygenation therapeutics: evaluating the oxygen delivery efficacy of artificial oxygen carriers and kosmotropes in vitro, Artificial cells, nanomedicine, and biotechnology 49 (2021) 317–324.

[35] S. Li, K. Pang, S. Zhu, K. Pate, J. Yin, Perfluorodecalin-based oxygenated emulsion as a topical treatment for chemical burn to the eye, Nature communications 13 (2022) 7371.

[36] D. Mayer, K.B. Ferenz, Perfluorocarbons for the treatment of decompression illness: how to bridge the gap between theory and practice, European journal of applied physiology 119 (2019) 2421–2433.

[37] S.C. Gale, G.D. Gorman, J.G. Copeland, P.F. McDonagh, Perflubron emulsion prevents PMN activation and improves myocardial functional recovery after cold ischemia and reperfusion, The Journal of surgical research 138 (2007) 135–140.

[38] R.J. Noveck, E.J. Shannon, P.T. Leese, J.S. Shorr, K.E. Flaim, P.E. Keipert, C.M. Woods, Randomized safety studies of intravenous perflubron emulsion. II. Effects on immune function in healthy volunteers, Anesthesia and analgesia 91 (2000) 812–822.

[39] D.A. Belinskaia, P.A. Voronina, V.I. Shmurak, R.O. Jenkins, N.V. Goncharov, Serum Albumin in Health and Disease: Esterase, Antioxidant, Transporting and Signaling Properties, International journal of molecular sciences 22 (2021).

[40] Hankins J., The role of albumin in fluid and electrolyte balance, J Infus Nurs 29 (2006) 260–265.

[41] A. Spada, J. Emami, J.A. Tuszynski, A. Lavasanifar, The Uniqueness of Albumin as a Carrier in Nanodrug Delivery, Molecular pharmaceutics 18 (2021) 1862–1894.

[42] M. Bern, K.M.K. Sand, J. Nilsen, I. Sandlie, J.T. Andersen, The role of albumin receptors in regulation of albumin homeostasis: Implications for drug delivery, Journal of controlled release : official journal of the Controlled Release Society 211 (2015) 144–162.

[43] V. Mishra, R.J. Heath, Structural and Biochemical Features of Human Serum Albumin Essential for Eukaryotic Cell Culture, International journal of molecular sciences 22 (2021).

[44] C. Tao, Y.J. Chuah, C. Xu, D.-A. Wang, Albumin conjugates and assemblies as versatile bio-functional additives and carriers for biomedical applications, Journal of materials chemistry. B 7 (2019) 357–367.

[45] S.-Q. Zhang, Q. Fu, Y.-J. Zhang, J.-X. Pan, L. Zhang, Z.-R. Zhang, Z.-M. Liu, Surface loading of nanoparticles on engineered or natural erythrocytes for prolonged circulation time: strategies and applications, Acta pharmacologica Sinica 42 (2021) 1040–1054.

[46] R. Haruki, T. Kimura, H. Iwasaki, K. Yamada, I. Kamiyama, M. Kohno, K. Taguchi, S. Nagao, T. Maruyama, M. Otagiri, T. Komatsu, Safety Evaluation of Hemoglobin-Albumin Cluster "HemoAct" as a Red Blood Cell Substitute, Scientific reports 5 (2015) 12778.

[47] J. Jägers, M. Kirsch, M. Cantore, O. Karaman, K.B. Ferenz, Artificial oxygen carriers in organ preservation: Dose dependency in a rat model of ex-vivo normothermic kidney perfusion, Artificial organs 46 (2022) 1783–1793.

[48] S. Varma, S. Dey, D. Palanisamy, Cellular Uptake Pathways of Nanoparticles: Process of Endocytosis and Factors Affecting their Fate, Current pharmaceutical biotechnology 23 (2022) 679–706.

[49] S. Behzadi, V. Serpooshan, W. Tao, M.A. Hamaly, M.Y. Alkawareek, E.C. Dreaden, D. Brown, A.M. Alkilany, O.C. Farokhzad, M. Mahmoudi, Cellular uptake of nanoparticles: journey inside the cell, Chemical Society reviews 46 (2017) 4218–4244.

[50] H.S. Choi, W. Liu, P. Misra, E. Tanaka, J.P. Zimmer, B. Itty Ipe, M.G. Bawendi, J.V. Frangioni, Renal clearance of quantum dots, Nature biotechnology 25 (2007) 1165–1170.

[51] E. Uribe-Querol, C. Rosales, Phagocytosis: Our Current Understanding of a Universal Biological Process, Frontiers in immunology 11 (2020) 1066.

[52] Y.L. Fu, R.E. Harrison, Microbial Phagocytic Receptors and Their Potential Involvement in Cytokine Induction in Macrophages, Frontiers in immunology 12 (2021) 662063.

[53] J.L. Guerriero, Macrophages: Their Untold Story in T Cell Activation and Function, International review of cell and molecular biology 342 (2019) 73–93.

[54] Y. Xing, X. Sun, Y. Dou, M. Wang, Y. Zhao, Q. Yang, Y. Zhao, The Immuno-Modulation Effect of Macrophage-Derived Extracellular Vesicles in Chronic Inflammatory Diseases, Frontiers in immunology 12 (2021) 785728.

[55] D.M. Mosser, K. Hamidzadeh, R. Goncalves, Macrophages and the maintenance of homeostasis, Cellular & molecular immunology 18 (2021) 579–587.

[56] J. Austermann, J. Friesenhagen, S.K. Fassl, B. Petersen, T. Ortkras, J. Burgmann, K. Barczyk-Kahlert, E. Faist, S. Zedler, S. Pirr, C. Rohde, C. Müller-Tidow, M. von Köckritz-Blickwede, C.S. von Kaisenberg, S.B. Flohé, T. Ulas, J.L. Schultze, J. Roth, T. Vogl, D. Viemann, Alarmins MRP8 and MRP14 induce stress tolerance in phagocytes under sterile inflammatory conditions, Cell reports 9 (2014) 2112–2123.

[57] I. Rubio, M.F. Osuchowski, M. Shankar-Hari, T. Skirecki, M.S. Winkler, G. Lachmann, P. La Rosée, G. Monneret, F. Venet, M. Bauer, F.M. Brunkhorst, M. Kox, J.-M. Cavaillon, F. Uhle, M.A. Weigand, S.B. Flohé, W.J. Wiersinga, M. Martin-Fernandez, R. Almansa, I. Martin-Loeches, A. Torres, E.J. Giamarellos-Bourboulis, M. Girardis, A. Cossarizza, M.G. Netea, T. van der Poll, A. Scherag, C. Meisel, J.C. Schefold, J.F. Bermejo-Martín, Current gaps in sepsis immunology: new opportunities for translational research, The Lancet. Infectious diseases 19 (2019) e422-e436.

[58] S. Epelman, K.J. Lavine, G.J. Randolph, Origin and functions of tissue macrophages, Immunity 41 (2014) 21–35.

[59] N.E. Reiner (Ed.), Macrophages and Dendritic Cells. Methods and Protocols, Humana Press, Totowa, NJ, 2009.

[60] A. Shapouri-Moghaddam, S. Mohammadian, H. Vazini, M. Taghadosi, S.-A. Esmaeili, F. Mardani, B. Seifi, A. Mohammadi, J.T. Afshari, A. Sahebkar, Macrophage plasticity, polarization, and function in health and disease, Journal of cellular physiology 233 (2018) 6425–6440.

[61] Z. Duan, Y. Luo, Targeting macrophages in cancer immunotherapy, Signal transduction and targeted therapy 6 (2021) 127.

[62] D. Zhou, C. Huang, Z. Lin, S. Zhan, L. Kong, C. Fang, J. Li, Macrophage polarization and function with emphasis on the evolving roles of coordinated regulation of cellular signaling pathways, Cellular signalling 26 (2014) 192–197.

[63] A. Castoldi, C. Naffah de Souza, N.O.S. Câmara, P.M. Moraes-Vieira, The Macrophage Switch in Obesity Development, Frontiers in immunology 6 (2015) 637.

[64] S.C. Harwani, Macrophages under pressure: the role of macrophage polarization in hypertension, Translational research : the journal of laboratory and clinical medicine 191 (2018) 45–63.

[65] C. Atri, F.Z. Guerfali, D. Laouini, Role of Human Macrophage Polarization in Inflammation during Infectious Diseases, International journal of molecular sciences 19 (2018).

[66] S. Arora, K. Dev, B. Agarwal, P. Das, M.A. Syed, Macrophages: Their role, activation and polarization in pulmonary diseases, Immunobiology 223 (2018) 383–396.

[67] U. Lendeckel, S. Venz, C. Wolke, Macrophages: shapes and functions, Chemtexts 8 (2022) 12.

[68] P.J. Murray, T.A. Wynn, Protective and pathogenic functions of macrophage subsets, Nature reviews. Immunology 11 (2011) 723–737.

[69] Y. Yao, X.-H. Xu, L. Jin, Macrophage Polarization in Physiological and Pathological Pregnancy, Frontiers in immunology 10 (2019) 792.

[70] C.T. Taylor, G. Doherty, P.G. Fallon, E.P. Cummins, Hypoxia-dependent regulation of inflammatory pathways in immune cells, The Journal of clinical investigation 126 (2016) 3716–3724.

[71] T.M. Bui, H.L. Wiesolek, R. Sumagin, ICAM-1: A master regulator of cellular responses in inflammation, injury resolution, and tumorigenesis, Journal of leukocyte biology 108 (2020) 787–799.

[72] H.L. Wiesolek, T.M. Bui, J.J. Lee, P. Dalal, A. Finkielsztein, A. Batra, E.B. Thorp, R. Sumagin, Intercellular Adhesion Molecule 1 Functions as an Efferocytosis Receptor in Inflammatory Macrophages, The American journal of pathology 190 (2020) 874–885.

[73] S.F. Bernatchez, M.R. Atkinson, P.J. Parks, Expression of intercellular adhesion molecule-1 on macrophages in vitro as a marker of activation, Biomaterials 18 (1997) 1371–1378.

[74] H. Zhong, H. Lin, Q. Pang, J. Zhuang, X. Liu, X. Li, J. Liu, J. Tang, Macrophage ICAM-1 functions as a regulator of phagocytosis in LPS induced endotoxemia, Inflammation research : official journal of the European Histamine Research Society … [et al.] 70 (2021) 193–203.

[75] S. Winning, F. Splettstoesser, J. Fandrey, S. Frede, Acute hypoxia induces HIF-independent monocyte adhesion to endothelial cells through increased intercellular adhesion molecule-1 expression: the role of hypoxic inhibition of prolyl hydroxylase activity for the induction of NF-kappa B, Journal of immunology (Baltimore, Md. : 1950) 185 (2010) 1786–1793.

[76] K. Schaffer, C.T. Taylor, The impact of hypoxia on bacterial infection, The FEBS journal 282 (2015) 2260–2266.

[77] C. Wiesner, V. Le-Cabec, K. El Azzouzi, I. Maridonneau-Parini, S. Linder, Podosomes in space: macrophage migration and matrix degradation in 2D and 3D settings, Cell adhesion & migration 8 (2014) 179–191.

[78] K. Cui, C.L. Ardell, N.P. Podolnikova, V.P. Yakubenko, Distinct Migratory Properties of M1, M2, and Resident Macrophages Are Regulated by αDβ2 and αMβ2 Integrin-Mediated Adhesion, Frontiers in immunology 9 (2018) 2650.

[79] G.E. Jones, Cellular signaling in macrophage migration and chemotaxis, Journal of leukocyte biology 68 (2000) 593–602.

[80] L. Chen, H. Deng, H. Cui, J. Fang, Z. Zuo, J. Deng, Y. Li, X. Wang, L. Zhao, Inflammatory responses and inflammation-associated diseases in organs, Oncotarget 9 (2018) 7204–7218.

[81] C.L. Stothers, L. Luan, B.A. Fensterheim, J.K. Bohannon, Hypoxia-inducible factor-1α regulation of myeloid cells, Journal of molecular medicine (Berlin, Germany) 96 (2018) 1293–1306.

[82] A. Palazon, A.W. Goldrath, V. Nizet, R.S. Johnson, HIF transcription factors, inflammation, and immunity, Immunity 41 (2014) 518–528.

[83] K.B. Sandau, J. Zhou, T. Kietzmann, B. Brüne, Regulation of the hypoxia-inducible factor 1alpha by the inflammatory mediators nitric oxide and tumor necrosis factor-alpha in contrast to desferroxamine and phenylarsine oxide, The Journal of biological chemistry 276 (2001) 39805–39811.

[84] A.F. McGettrick, L.A.J. O'Neill, The Role of HIF in Immunity and Inflammation, Cell metabolism 32 (2020) 524–536.

[85] R.B. Johnston, JR, Oxygen metabolism and the microbicidal activity of macrophages, Federation proceedings 37 (1978) 2759–2764.

[86] A. Górski, R. Międzybrodzki, J. Borysowski, K. Dąbrowska, P. Wierzbicki, M. Ohams, G. Korczak-Kowalska, N. Olszowska-Zaremba, M. Łusiak-Szelachowska, M. Kłak, E. Jończyk, E. Kaniuga, A. Gołaś, S. Purchla, B. Weber-Dąbrowska, S. Letkiewicz, W. Fortuna, K. Szufnarowski, Z. Pawełczyk, P. Rogóż, D. Kłosowska, Phage as a modulator of immune responses: practical implications for phage therapy, Advances in virus research 83 (2012) 41–71.

[87] L. Cavinato, E. Genise, F.R. Luly, E.G. Di Domenico, P. Del Porto, F. Ascenzioni, Escaping the Phagocytic Oxidative Burst: The Role of SODB in the Survival of Pseudomonas aeruginosa Within Macrophages, Frontiers in microbiology 11 (2020) 326.

[88] P. Irato, G. Santovito, Enzymatic and Non-Enzymatic Molecules with Antioxidant Function, Antioxidants (Basel, Switzerland) 10 (2021).

[89] S. Reuter, S.C. Gupta, M.M. Chaturvedi, B.B. Aggarwal, Oxidative stress, inflammation, and cancer: how are they linked?, Free radical biology & medicine 49 (2010) 1603–1616.

[90] U. Ziegler, P. Groscurth, Morphological features of cell death, News in physiological sciences : an international journal of physiology produced jointly by the International Union of Physiological Sciences and the American Physiological Society 19 (2004) 124–128.

[91] M.S. D'Arcy, Cell death: a review of the major forms of apoptosis, necrosis and autophagy, Cell biology international 43 (2019) 582–592.

[92] S. van Cruchten, W. van den Broeck, Morphological and biochemical aspects of apoptosis, oncosis and necrosis, Anatomia, histologia, embryologia 31 (2002) 214–223.

[93] N. Vanlangenakker, T. Vanden Berghe, D.V. Krysko, N. Festjens, P. Vandenabeele, Molecular mechanisms and pathophysiology of necrotic cell death, Current molecular medicine 8 (2008) 207–220.

[94] P. Kumar, A. Nagarajan, P.D. Uchil, Analysis of Cell Viability by the Lactate Dehydrogenase Assay, Cold Spring Harbor protocols 2018 (2018).

[95] J. Cuddihy, G. Wu, L. Ho, H. Kudo, A. Dannhorn, S. Mandalia, D. Collins, J. Weir, A. Spencer, M. Vizcaychipi, Z. Takats, I. Nagy, Lactate dehydrogenase activity staining demonstrates time-dependent immune cell infiltration in human ex-vivo burn-injured skin, Scientific reports 11 (2021) 21249.

[96] C. Kioussi, Odontogenesis. Methods and protocols, Humana Press, New York, 2012.

[97] K.J. Livak, T.D. Schmittgen, Analysis of relative gene expression data using real-time quantitative PCR and the 2(-Delta Delta C(T)) Method, Methods (San Diego, Calif.) 25 (2001) 402–408.

[98] E.K. Park, H.S. Jung, H.I. Yang, M.C. Yoo, C. Kim, K.S. Kim, Optimized THP-1 differentiation is required for the detection of responses to weak stimuli, Inflammation research : official journal of the European Histamine Research Society … [et al.] 56 (2007) 45–50.

[99] K.B. Ferenz, Improved Albumin-Derived Per Fluorocarbon- Based Artificial Oxygen Carriers: In-vivo Evaluation of Biocompatibility, AIBM 7 (2017).

[100] D. Mayer, F. Guerrero, C. Goanvec, L. Hetzel, J. Linders, M. Ljubkovic, A. Kreczy, C. Mayer, M. Kirsch, K.B. Ferenz, Prevention of Decompression Sickness by Novel Artificial Oxygen Carriers, Medicine and science in sports and exercise 52 (2020) 2127–2135.

[101] S.M. Pinto, H. Kim, Y. Subbannayya, M. Giambelluca, K. Bösl, R.K. Kandasamy, Dose-dependent phorbol 12-myristate-13-acetate-mediated monocyte-to-macrophage differentiation induces unique proteomic signatures in THP-1 cells, 2020.

[102] S.L. Figenschau, E. Knutsen, I. Urbarova, C. Fenton, B. Elston, M. Perander, E.S. Mortensen, K.A. Fenton, ICAM1 expression is induced by proinflammatory cytokines and associated with TLS formation in aggressive breast cancer subtypes, Scientific reports 8 (2018) 11720.

[103] F. Khorshid, The Effect of the Medium Viscosity on the Cells Morphology in Reaction of Cells to Topography-I (2004) 15–17.

[104] S. Naqvi, M. Samim, M. Abdin, F.J. Ahmed, an Maitra, C. Prashant, A.K. Dinda, Concentration-dependent toxicity of iron oxide nanoparticles mediated by increased oxidative stress, International journal of nanomedicine 5 (2010) 983–989.

[105] L.W. Ott, K.A. Resing, A.W. Sizemore, J.W. Heyen, R.R. Cocklin, N.M. Pedrick, H.C. Woods, J.Y. Chen, M.G. Goebl, F.A. Witzmann, M.A. Harrington, Tumor Necrosis Factor-alpha- and interleukin-1-induced cellular responses: coupling proteomic and genomic information, Journal of proteome research 6 (2007) 2176–2185.

[106] D. Kalb, H.D. Vo, S. Adikari, E. Hong-Geller, B. Munsky, J. Werner, Visualization and modeling of inhibition of IL-1β and TNF-α mRNA transcription at the single-cell level, Scientific reports 11 (2021) 13692.

[107] C. Eder, Mechanisms of interleukin-1β release, Immunobiology 214 (2009) 543–553.

[108] T. Shogi, A. Miyamoto, S. Ishiguro, A. Nishio, Enhanced release of IL-1beta and TNF-alpha following endotoxin challenge from rat alveolar macrophages cultured in low-mg(2+) medium, Magnesium research 16 (2003) 111–119.

[109] S. Chen, A.F.U.H. Saeed, Q. Liu, Q. Jiang, H. Xu, G.G. Xiao, L. Rao, Y. Duo, Macrophages in immunoregulation and therapeutics, Signal transduction and targeted therapy 8 (2023) 207.

[110] S. Hirano, Q. Zhou, A. Furuyama, S. Kanno, Differential Regulation of IL-1β and IL-6 Release in Murine Macrophages, Inflammation 40 (2017) 1933–1943.

[111] N. Kaneko, M. Kurata, T. Yamamoto, S. Morikawa, J. Masumoto, The role of interleukin-1 in general pathology, Inflammation and regeneration 39 (2019) 12.

[112] R. Kaur, V. Singh, P. Kumari, R. Singh, H. Chopra, T.B. Emran, Novel insights on the role of VCAM-1 and ICAM-1: Potential biomarkers for cardiovascular diseases, Annals of medicine and surgery (2012) 84 (2022) 104802.

[113] A.R. Johnson, A.J. Freemerman, E.D. Abel, J. Rathmell, L. Makowski, Glucose metabolism is linked to the inflammatory status of macrophages, BMC Proc 6 (2012).

[114] M. Obaid, S.M.N. Udden, P. Alluri, S.S. Mandal, LncRNA HOTAIR regulates glucose transporter Glut1 expression and glucose uptake in macrophages during inflammation, Scientific reports 11 (2021) 232.

[115] S. Cambier, M. Gouwy, P. Proost, The chemokines CXCL8 and CXCL12: molecular and functional properties, role in disease and efforts towards pharmacological intervention, Cellular & molecular immunology 20 (2023) 217–251.

[116] T. Pentcheva-Hoang, J.G. Egen, K. Wojnoonski, J.P. Allison, B7-1 and B7-2 Selectively Recruit CTLA-4 and CD28 to the Immunological Synapse, Immunity 21 (2004) 401–413.

[117] S.L. Topalian, C.G. Drake, D.M. Pardoll, Immune checkpoint blockade: a common denominator approach to cancer therapy, Cancer cell 27 (2015) 450–461.

[118] Y. Zhou, Y. Yang, G. Warr, R. Bravo, LPS down-regulates the expression of chemokine receptor CCR2 in mice and abolishes macrophage infiltration in acute inflammation, Journal of leukocyte biology 65 (1999) 265–269.

[119] R. Nicolete, D.F. dos Santos, L.H. Faccioli, The uptake of PLGA micro or nanoparticles by macrophages provokes distinct in vitro inflammatory response, International immunopharmacology 11 (2011) 1557–1563.

[120] D. Paul, S. Achouri, Y.-Z. Yoon, J. Herre, C.E. Bryant, P. Cicuta, Phagocytosis dynamics depends on target shape, Biophysical journal 105 (2013) 1143–1150.

[121] N. Tanaka, Electron Nano-Imaging. Basics of Imaging and Diffraction for TEM and STEM, Springer Japan; Imprint: Springer, Tokyo, 2017.

[122] M. Reifarth, D. Pretzel, S. Schubert, C. Weber, R. Heintzmann, S. Hoeppener, U.S. Schubert, Cellular uptake of PLA nanoparticles studied by light and electron microscopy: synthesis, characterization and biocompatibility studies using an iridium(III) complex as correlative label, Chemical communications (Cambridge, England) 52 (2016) 4361–4364.

[123] M. Jung, T.K. Kim, H.-N. Woo, J.Y. Mun, H. Lee, C.-G. Pack, Correlative Light and Electron Microscopy for Nanoparticle-Cell Interaction and Protein Localization, Advances in experimental medicine and biology 1310 (2021) 115–132.

[124] K.S. Lavrich, A.M. Speen, A.J. Ghio, P.A. Bromberg, J.M. Samet, N.E. Alexis, Macrophages from the upper and lower human respiratory tract are metabolically distinct, American journal of physiology. Lung cellular and molecular physiology 315 (2018) L752-L764.

[125] R.P. Pandian, V.K. Kutala, A. Liaugminas, N.L. Parinandi, P. Kuppusamy, Lipopolysaccharide-induced alterations in oxygen consumption and radical generation in endothelial cells, Molecular and cellular biochemistry 278 (2005) 119–127.

[126] D. Tsikas, Assessment of lipid peroxidation by measuring malondialdehyde (MDA) and relatives in biological samples: Analytical and biological challenges, Analytical biochemistry 524 (2017) 13–30.

[127] C.J. Busch, C.J. Binder, Malondialdehyde epitopes as mediators of sterile inflammation, Biochimica et biophysica acta. Molecular and cell biology of lipids 1862 (2017) 398–406.

[128] J. Jägers, Charakterisierung und ex vivo Untersuchung eines künstlichen Sauerstoffträgers für den Einsatz zur Konservierung von Nieren. Universität Duisburg-Essen, Dissertation (2021).

[129] K. Neubauer, B. Zieger, Endothelial cells and coagulation, Cell and tissue research 387 (2022) 391–398.

[130] B.J. Hunt, K.M. Jurd, Endothelial cell activation. A central pathophysiological process, BMJ (Clinical research ed.) 316 (1998) 1328–1329.

11. Appendix

11.1. Table of figures

11.2. Table of tables

11.3. Table of abbreviations

11.4. List of publications and congress contributions

11.4.1. Posters

Linda Marciale Tchuendem, Shah Bahrullah Shah, Katja Bettina Ferenz (2021): Do Albumin-derived perfluorocarbon-based artificial oxygen carriers (A−AOCs) activate immune cells? 100. Jahrestagung der Deutschen Physiologischen Gesellschaft, Frankfurt, 2021.

Linda Marciale Tchuendem, Katja Bettina Ferenz (2022): Do albumin-derived perfluorocarbon-based artificial oxygen carriers (A −AOCs) interact with primary human macrophages (PHM)? 11th Young Physiologists Symposium, Essen 2022.

Linda Marciale Tchuendem, Justin Sonneck, Katja Bettina Ferenz (2022): Contact with albumin-derived perfluorocarbon-based artificial oxygen carriers does not activate primary human macrophages. Europhysiology 2022, Copenhagen, 2023.

Linda Marciale Tchuendem, Nico Uhde, Katja Bettina Ferenz (2023): Do albumin-derived perfluorocarbon-based artificial oxygen carriers (A −AOCs) interact with murine J774 macrophages? 12th Symposium of the Young Physiologists, Kiel, 2023.

L.M. Tchuendem, F. Bos, N. Uhde, H. Jastrow, K.B. Ferenz (2023): How does the immune system react on albumin-derived perfluorocarbon-based artificial oxygen carriers (A −AOCs)? 3rd CENIDE Conference, Bergisch Gladbach, 2023

LM. Tchuendem, Felix Bos, N. Uhde, KB. Ferenz (2023): Do primary murine macrophages (BMDM) and murine J774 macrophages interact differently with albumin-derived perfluorocarbon-based artificial oxygen carriers (A −AOCs)? 10th NRW Nano Conference, Dortmund, 2023.

11.4.2. Talks

Linda Marciale Tchuendem, Katja Bettina Ferenz (2021): Albumin-derived perfluorocarbon-based artificial oxygen carriers (A−AOCs) do not activate primary human macrophages. 20th Day of Science at the Medical Faculty, University of Duisburg-Essen, Essen, 2021.

Linda Marciale Tchuendem, Katja Bettina Ferenz (2021): Molecular responses in macrophages exposed to albumin-derived perfluorocarbon-based artificial oxygen carriers:

Annual Retreat of the Graduate School of Biomedical Science (BIOME), Core: “Ischemia, Reperfusion and Angiogenesis”, Essen 2021.

11.5. Acknowledgments

I would like to extend my gratitude to several individuals who have played significant roles in the completion of my thesis. Firstly, I want to express my deep gratitude to Jun.-Prof. Dr. Katja Ferenz for giving me the opportunity to undertake my thesis under her guidance. Katja, throughout my doctoral studies, you have been an exceptional mentor, offering not just your expertise, but also empowerment and sincere care. Your leadership style has imparted invaluable lessons to me. I am deeply appreciative of your commitment, time, and patience. Your guidance has not only shaped my growth as a researcher but has also positively influenced my personal growth.

Secondly, I extend my thanks to Prof. Dr. med. Joachim Fandrey for his excellent advisement on my PhD project and for facilitating the necessary administrative processes for my position. I am also grateful to Prof. Dr. Stefanie Flohé for agreeing to serve as the second examiner for this work.

I must also acknowledge Dr. Sandra Winning for her constant support. Sandra, your constant availability for my questions and challenges propelled my work significantly, especially regarding flow cytometry experiments.

I extend my sincere appreciation to Claudia Padberg for her friendly and supportive presence, particularly for accompanying me to select experimental animals from the animal facility.

I am thankful to Dr. Miriam Cantore, Eva Hillen, and Susanne Eitner for their technical assistance in the lab.

I am grateful to Nico Uhde, who carried out his bachelor's thesis under my supervision, and to Felix Bos, who completed his specialized internship in the master’s program in chemistry under my guidance. Their valuable contributions significantly enhanced this work.

My appreciation goes to my colleagues Ozan, Shah, Jan-Eric, Fabian, Tobias and Jacqueline for providing a productive working environment and for the inspiring and enjoyable conversations we have shared.

I also extend my thanks to the neighbouring research groups, AG Metzen and AG Fandrey, for their supportive presence in the lab – it has been a pleasure sharing the space with you all.

A special mention of gratitude goes out to Justin Sonneck from Leibniz-Institut für Analytische Wissenschaften - ISAS - e.V. for his significant contributions to the analysis of specific

confocal images. Justin, your engaged collaboration, and valuable insights are deeply appreciated.

My appreciation is extended to Dr. Mike Hasenberg, PD Dr. Holger Jastrow, Bernd Walkenfort, and Sylvia Voortmann for their work in performing electron microscopy and correlative light and electron microscopy.

I reserve deep gratitude for my family and friends for their patience and support, particularly my husband Marvin, who took parental leave to care for our daughter Esther, enabling me to continue with this project. This thesis would not have been possible without your continued support. I am thankful to my mother Sylvienne and to my siblings – Eric-Joel, Guy-Patrice, Michel, and Sidonie – for their enduring encouragement throughout my academic journey.

11.6. Declaration

Hiermit versichere ich, dass ich die vorliegende Arbeit mit dem Titel

„Investigating the Immune Cell Response to Albumin-Derived Perfluorocarbon-Based Artificial Oxygen Carriers (A−AOCs)"

selbstständig verfasst und keine anderen als die angegebenen Quellen und Hilfsmittel benutzt habe. Passagen in dieser Arbeit, sowie gegebenenfalls enthaltene Abbildungen, Zeichnungen oder Grafiken, die wortwörtlich oder inhaltlich aus anderen Werken übernommen wurden, sind entsprechend gekennzeichnet und die Quellen sind angegeben. Die Arbeit ist noch nicht an anderer Stelle als Prüfungsleistung vorgelegt worden.

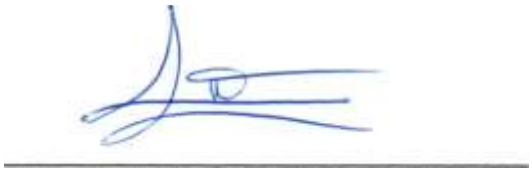

Essen, den 14.11.2023

Linda Marciale Tchuendem